



Politechnika Wroclawska

FIELD OF SCIENCE: Natural sciences

DISCIPLINE OF SCIENCE: Chemical Sciences (Nauki Chemiczne)

DOCTORAL DISSERTATION

Optical properties of chiral heterostructures with gold nanoparticles

Maciej Lipok

Supervisor:

PhD. DSc. Eng. Joanna Olesiak-Bańska

Keywords: optical properties, chiral nanomaterials, gold nanoparticles, gold nanoclusters

WROCLAW 2025

Acknowledgements

First of all, I extend my deepest thanks to my supervisor, Professor **Joanna Olesiak-Bańska**, for her guidance, constant support, unwavering patience, and boundless encouragement that have been the bedrock upon which this work stands. Thank you, for all the great discussions concerning our mutual goal to understand the nanoworld and, most of all, the knowledge and skills I gained during my scientific journey.

To my colleagues, **Patryk Obstarczyk, Anna Pniakowska, Agata Hajda, and Manuela Grelich-Mucha**, the brilliant minds who have walked beside me on this winding path of discovery, your camaraderie has been both a beacon of light in moments of doubt and a spark of inspiration in times of triumph. This dissertation is not merely a solitary effort but a reflection of the generosity, brilliance, and kindness that you all have so freely shared. Thank you all for the great time spent together!

I would also like to thank Professor **Julie Biteen** for the support and guidance during my internship at the University of Michigan as well as **Saaj Chattopadhyay** and **Zechariah Pffafenberger**, for their extraordinary skills and passion for single-molecule microscopy, which resulted in joint research on the interactions of single nanoparticles with amyloid fibrils.

Next, I would like to extend my deepest gratitude to Professor **Wiktor Lewandowski** for his ideas and great knowledge about the liquid-crystalline materials that led to joint work on the interaction between gold nanoclusters and liquid-crystalline helices. No lesser thanks to **Sylwia Parzyszek**, for her help with TEM imaging of chiral heterostructures with gold nanoclusters, and **Maciej Bagiński**, for the synthesis of liquid-crystalline materials used in my research.

I also thank Professor **Thomas Buergi** and **Yanan Wang** for their help in understanding the intriguing world of atomically-precise gold nanoclusters and their structures.

I would also like to thank **Andrzej Żak** for his invaluable help with TEM imaging of chiral heterostructures created during my research. The images you take and the skills you have are of the highest world standard!

I am also tremendously grateful to the entire administration of the **Doctoral School of Wrocław University of Science and Technology** for their immense help with a plethora of various smaller and bigger matters that occurred during my studies and readiness to solve every problem I encountered during this journey.

Last, but definitely not least, I would like to thank the people who were with me before I started my scientific adventure and supported me throughout the entire process until the very end – **my family, friends, and loved ones**. Without you all, this would never have been possible.

Abstract

Despite the enormous progress of science and medicine over the last century, there is still a lack of efficient tools for detecting and imaging biomolecules important to human health. Since many of them are chiral, this issue could be resolved by exploring their selective interaction with sensor materials like gold nanoparticles. These selective interactions can often be observed as changes in the chiral optical properties of nanoparticle-biomolecule assemblies. Thus, studying these properties can lead to the invention of new methods for the selective detection of chiral molecules, such as proteins or their aggregates, and the creation of new advanced materials exhibiting unique chiral optical properties.

The aim of this doctoral thesis is to explore how assembling plasmonic gold nanoparticles or gold nanoclusters with various chiral molecules influences their optical properties and discover new chiroptical properties emerging upon the assembly. The thesis starts with the literature review introducing the topic of chiral heterostructures with plasmonic gold nanoparticles and gold nanoclusters, which shows that there are still many open questions concerning the heterostructure assembly and their chiroptical properties. Some of these questions are addressed within the framework of this thesis using various spectroscopy and microscopy methods. The first part of the presented research focuses on the chiroptical properties of chiral biomolecule-coated gold nanoclusters. I explored the circular dichroism and circularly polarized luminescence spectra of ATT (6-aza-2-thiothymine) stabilized chiral gold nanocluster and its two enantiomers, functionalized with L- and D-arginine. Although the enantiomers were characterized by mirror-like circular dichroism (CD) spectra, their circularly polarized luminescence (CPL) was of one handedness. Further studies have shown that one of the possible explanations is the kernel-structure relaxation since arginine-free ATT nanoclusters exhibited CPL of the same sign and order of magnitude. Moreover, I analyzed their two-photon excited CPL using the home-built system I developed during my doctoral research. The obtained signal was two orders of magnitude stronger than one-photon excited CPL, which was explained by the different radiative relaxation pathways of one-photon and two-photon luminescence of studied nanoclusters. The results presented in this topic not only proved the broken symmetry between chiral light absorption (CD) and chiral photoluminescence (CPL) of ATT-stabilized gold nanoclusters but also showed that their nonlinear chiroptical effects can be stronger than their linear counterparts.

The second issue addressed in this work concerned the still poorly understood template-assisted assembly of gold nanoclusters. I checked if the helical assembly method using a liquid-crystal template creating helical nanofilaments would be applicable to atomically precise achiral gold nanoclusters $\text{Au}_{25}(\text{PET})_{18}$. As confirmed by the resulting microscopy image, surface functionalization of $\text{Au}_{25}(\text{PET})_{18}$ with two ligands, dodecanethiol and liquid-crystalline ligand derived from the template, allowed efficient mixing with the template material and lead to the helical assembly of nanoclusters. Moreover, the helical assembly influenced the optical properties of gold nanoclusters: red-shifted the luminescence of studied nanoclusters, but also generated new chiroptical properties. Using the CPL microscope I constructed, I discovered that helically-assembled gold nanoclusters generate strong circularly polarized luminescence of the handedness depending on the helical twist of the nanofilaments hosting them. This

confirmed that achiral gold nanoclusters could obtain chiral optical properties upon binding to helical nanofilaments.

The last part of this dissertation focused on finding the origin and application of chiral optical properties emerging upon assembling the plasmonic gold nanoparticles with chiral biomolecules. For this purpose, I studied the optical properties of chiral heterostructures assembled using the achiral anisotropic gold nanoparticles, like nanobipyramids and nanorods, and chiral bovine insulin protein aggregates. Not only did I discover that such assembly is possible by controlling the parameters such as solution pH or NaCl concentration but also that a new chiroptical property – induced circular dichroism, emerges upon the assembly. The observed signal did not result from the helical arrangement of gold nanoparticles but, as confirmed by the heterostructures morphology and optical properties, coulombic interactions between the gold nanoparticles and chiral protein molecules. Thus, I explored if the induced optical chirality could be used for selective biosensing of insulin protein aggregates. By studying the optical properties of chiral heterostructures with insulin protein aggregates characterized by different structures I observed that the location and strength of induced circular dichroism is connected with the aggregate internal structure and the exposure of the chiral tyrosine residues. Finally, I studied the chiral heterostructures made from gold nanorods and insulin amyloid fibrils. The experiments showed that it is possible to induce circular dichroism under such conditions. Although, as confirmed by polarization-resolved single-molecule microscopy, at the single-particle level, single gold nanorods bound to insulin fibrils did not show any induced chirality.

The results presented in this doctoral thesis proved that the optical properties of chiral heterostructures with gold nanoparticles can be used to understand the interactions of chiral organic molecules with their inorganic environment and to selectively detect some of them, which in the future can be used to develop new methods for selective detecting and imaging of chiral molecules like proteins or DNA.

Abstract in Polish (Streszczenie po polsku)

Pomimo ogromnego postępu nauki i medycyny w ciągu ostatniego stulecia, nadal brak skutecznych narzędzi do detekcji i obrazowania licznych biocząsteczek ważnych dla zdrowia człowieka. Ponieważ wiele z nich jest chiralnych, problem ten można rozwiązać, badając ich selektywne interakcje z materiałami łatwymi do detekcji, takimi jak nanocząstki złota. Te selektywne interakcje można często zaobserwować poprzez zmiany chiralnych właściwości optycznych takich struktur. Badanie tych właściwości może doprowadzić do wynalezienia nowych metod selektywnej detekcji chiralnych cząsteczek, takich jak białka lub ich agregaty, oraz do stworzenia nowych materiałów zaawansowanych wykazujących unikalne chiralne właściwości optyczne.

Celem tej rozprawy doktorskiej jest zbadanie, w jaki sposób oddziaływanie plazmonicznych nanocząstek złota lub nanoklastrów złota z różnymi chiralnymi cząsteczkami wpływa na ich właściwości optyczne i odkrycie nowych chiralnych właściwości optycznych pojawiających się w heterostrukturach. Praca rozpoczyna się od przeglądu literatury wprowadzającego temat chiralnych heterostruktur z plazmonicznymi nanocząstkami złota i nanoklastami złota, który pokazuje, że nadal istnieje wiele otwartych pytań dotyczących tworzenia takich heterostruktur i ich właściwości optycznych. Odpowiedzi na postawione w pracy pytania szukałem wykorzystując w badaniach liczne metody spektroskopowe i mikroskopowe. Pierwsza część przedstawionych badań koncentruje się na chiralnych właściwościach optycznych nanoklastrów złota opłaszczonych chiralnymi biocząsteczkami. W ramach tych badań, zbadalem widma dichroizmu kołowego i kołowo spolaryzowanej luminescencji chiralnych nanoklastrów złota stabilizowanych 6-aza-2-tiotyminą (ATT) i ich dwóch enancjomerów sfunkcjonalizowanych L- i D-argininą. Mimo, że enancjomery charakteryzowały się lustrzanym odbiciem widm dichroizmu kołowego (CD), ich kołowo spolaryzowana luminescencja (CPL) była tego samego znaku. Dalsze badania wykazały, że jednym z możliwych wyjaśnień tego efektu jest relaksacja promienista z rdzenia nanoklastra, ponieważ nanoklastry nie sfunkcjonalizowane chiralnymi ligandami argininy wykazywały CPL tego samego znaku i rzędu wielkości co chiralne enancjomery. Ponadto przeanalizowałem dwufotonowo wzbudzoną CPL (2P CPL) tych nanostruktur przy użyciu systemu pomiarowego opracowanego samodzielnie podczas moich badań i również opisanego w pracy. Uzyskany sygnał 2P CPL był o dwa rzędy wielkości silniejszy niż jednofotonowo wzbudzone CPL, co zostało wyjaśnione różnymi ścieżkami relaksacji promienistej wzbudzonej jednofotonowo i dwufotonowo badanych nanoklastrów. Przedstawione wyniki nie tylko udowodniły złamanie symetrii pomiędzy chiralną absorpcją (CD) i chiralną emisją (CPL) nanoklastrów złota stabilizowanych ATT, ale także pokazały, że nieliniowe efekty chiralne mogą być silniejsze niż ich liniowe odpowiedniki.

Drugim zagadnieniem poruszonym w ramach tej pracy było zbadanie wciąż słabo poznanej metody helikalnego układania nanoklastrów złota wspomaganego matrycą. W ramach tych badań, sprawdziłem czy matryca ciekłokrystaliczna, tworząca w odpowiednich warunkach helikalne nanofilamenty, może zostać zastosowana do helikalnego ułożenia atomowo precyzyjnych achiralnych nanoklastrów złota $\text{Au}_{25}(\text{PET})_{18}$. Uzyskane obrazy mikroskopowe pokazały, że funkcjonalizacja powierzchni $\text{Au}_{25}(\text{PET})_{18}$ dwoma ligandami, dodekanotiolem i

ciekłokrystalicznym ligandem będącym pochodną matrycy, umożliwiła zmieszanie nanoklastrów z materiałem matrycy i w rezultacie helikalne ułożenie nanoklastrów. Co więcej, ułożenie to wpłynęło na ich właściwości optyczne. Nie tylko przesunęło długość fali luminescencji badanych nanoklastrów ku czerwieni, ale także wygenerowało nowe właściwości chiroptyczne. Używając skonstruowanego przeze mnie i opisanego w pracy mikroskopu CPL odkryłem, że nanoklastry złota, ułożone helikalnie dzięki matrycy, generują silną kołowo spolaryzowaną luminescencję o znaku zależnym od skrętu helikalnych nanofilamentów, na których się znajdują. Potwierdziło to, że achiralne nanoklastry złota mogą uzyskać chiralne właściwości optyczne po opłaszczeniu ciekłokrystalicznych helikalnych nanofilamentów.

Ostatnia część rozprawy doktorskiej skupiała się na znalezieniu źródła i zastosowania chiralnych właściwości optycznych pojawiających się po zmieszaniu plazmonicznych nanocząstek złota z chiralnymi biocząsteczkami. W tym celu zbadałem właściwości optyczne chiralnych heterostruktur stworzonych z achiralnych anizotropowych nanocząstek złota, takich jak nanobipiramidy i nanopręty, oraz chiralnych agregatów białkowych insuliny bydłcej. W ramach tych badań odkryłem, że aby stworzyć taki rodzaj heterostruktur kluczowa jest kontrola parametrów, takich jak pH roztworu lub stężenie NaCl, oraz że po ich stworzeniu ukazuje się nowa właściwość chiroptyczna – indukowany dichroizm kołowy. Zaobserwowany sygnał nie wynikał z helikalnego ułożenia nanocząstek złota ale, jak potwierdziła morfologia heterostruktur i ich właściwości optyczne, oddziaływania kulombowskiego między nanocząstkami złota a chiralnymi cząsteczkami białek. Zbadałem zatem, czy indukowany dichroizm kołowy może zostać wykorzystana do selektywnej detekcji agregatów insuliny. Badając właściwości optyczne różnych chiralnych heterostruktur utworzonych z agregatami białka insuliny charakteryzującymi się różnymi strukturami, zaobserwowałem, że lokalizacja i siła indukowanego dichroizmu kołowego jest związana z wewnętrzną strukturą białkowych agregatów i ekspozycją chiralnych reszt tyrozyny. Na koniec zbadałem chiralne heterostrukтуры wykonane z nanoprętów złota i fibryli amyloidowych insuliny. Eksperymenty wykazały, że w odpowiednich warunkach, możliwe jest indukowanie dichroizmu kołowego również w takich układach. Jednak, jak potwierdzono za pomocą mikroskopii polaryzacyjnej pojedynczych cząsteczek, na poziomie pojedynczych cząsteczek, pojedyncze nanopręty złota związane z fibrylami insuliny nie wykazywały żadnej indukowanej chiralności.

Wyniki przedstawione w tej rozprawie doktorskiej udowodniły, że właściwości optyczne chiralnych heterostruktur z nanocząsteczkami złota mogą być wykorzystane do zrozumienia oddziaływań chiralnych cząsteczek organicznych z ich nieorganicznym otoczeniem oraz do selektywnego wykrywania niektórych z nich. Wyniki tych badań i odkryte zależności, mogą być w przyszłości wykorzystane do opracowania nowych metod selektywnego wykrywania i obrazowania chiralnych cząsteczek, takich jak białka lub DNA.

Table of contents

ACKNOWLEDGEMENTS	2
ABSTRACT	3
ABSTRACT IN POLISH (STRESZCZENIE PO POLSKU)	5
DISSERTATION OBJECTIVES AND MOTIVATION	9
ABBREVIATIONS	11
LITERATURE REVIEW	12
I. STUDIES ON CHIRALITY AND ITS IMPACT ON SOCIETY	12
II. CHIRAL HETEROSTRUCTURES – THE VERSATILE CHIRAL NANOMATERIALS	13
II.1 <i>Chiral nanomaterials</i>	13
II.2 <i>Chiral heterostructures – highly adaptable nanomaterials</i>	15
II.3 <i>Fabrication techniques for chiral heterostructures</i>	16
II.4 <i>Chiral templates used in chiral heterostructure</i>	17
II.5 <i>Chiroptical properties of chiral heterostructures</i>	19
II.6 <i>Applications</i>	22
III. PLASMONIC GOLD NANOPARTICLES	25
III.1 <i>Synthesis of plasmonic gold nanoparticles</i>	25
III.2 <i>Optical properties of plasmonic gold nanoparticles</i>	26
III.3 <i>Chirality in plasmonic gold nanoparticles</i>	28
III.4 <i>Applications of plasmonic gold nanoparticles</i>	30
IV. GOLD NANOCLUSTERS	31
IV.1 <i>Synthesis of gold nanoclusters</i>	31
IV.2 <i>Optical properties of gold nanoclusters</i>	32
IV.3 <i>Chirality of gold nanoclusters</i>	35
IV.4 <i>Applications of gold nanoclusters</i>	36
V. CHIRAL HETEROSTRUCTURES WITH GOLD NANOPARTICLES	38
V.1 <i>Template-directed chiral heterostructures with plasmonic gold nanoparticles</i>	39
V.2 <i>Template-directed chiral heterostructures with gold nanoclusters</i>	43
V.3 <i>Chiral biomolecule-protected gold nanoclusters</i>	44
V.4 <i>Selected questions regarding the chiral heterostructures with gold nanoparticles</i>	46
EXPERIMENTAL METHODS	48
VI.1 ONE AND TWO-PHOTON EXCITED CIRCULARLY POLARIZED LUMINESCENCE	48
VI.2 TWO-PHOTON EXCITED FLUORESCENCE LIFETIMES	52
RESULTS	56
VII. CHIROPTICAL PROPERTIES OF CHIRAL GOLD NANOCLUSTERS	56
VII.1 <i>Materials & methods</i>	57
VII.2 <i>Synthesis, purification and functionalization of ATT-AuNCs</i>	58
VII.3 <i>Optical characterization of ATT-AuNCs before and after the functionalization with arginine</i>	58
VII.4 <i>Linear chiroptical properties</i>	60
VII.5 <i>Non-linear chiroptical properties</i>	62
VII.6 <i>Conclusions</i>	65
VIII. OPTICAL PROPERTIES OF CHIRAL HETEROSTRUCTURES WITH GOLD NANOCLUSTERS	67

VIII. 1	<i>Materials & methods</i>	68
VIII. 2	<i>Synthesis and characterization of achiral gold nanoclusters Au₂₅(PET)₁₈</i>	69
VIII. 3	<i>Liquid crystalline matrix characterization</i>	72
VIII. 4	<i>Nanocluster functionalization and chiral heterostructure preparation</i>	74
VIII. 5	<i>Results & discussion</i>	79
VIII. 6	<i>Conclusions</i>	83
IX.	OPTICAL PROPERTIES OF CHIRAL HETEROSTRUCTURES WITH ANISOTROPIC PLASMONIC GOLD NANOPARTICLES	84
IX. 1	<i>Materials & methods</i>	85
IX. 2	<i>Optical properties of gold nanobipyramids</i>	86
IX. 3	<i>Chiral protein aggregates of bovine insulin</i>	87
IX. 4	<i>Chiral heterostructure sample preparation</i>	91
IX. 5	<i>Exploring the chirality transfer between chiral insulin matrix and gold nanobipyramids</i>	94
IX. 6	<i>Chirality transfer between the plasmonic nanoparticles and amyloid fibrils at single-particle level</i> 99	
IX. 7	<i>Conclusions</i>	103
CONCLUSIONS & PERSPECTIVES		105
BIBLIOGRAPHY		108
APPENDIX		121

Dissertation objectives and motivation

The main goal of this dissertation is to explore how assembling plasmonic gold nanoparticles or gold nanoclusters into chiral heterostructures influences their optical properties and to discover new chiroptical properties emerging upon the assembly.

We currently live in a time when ground-breaking scientific discoveries made in the 19th and 20th centuries have led to a point where medicine can significantly extend the length of human life and effectively treat most of the diseases that afflict it. Unfortunately, many health problems, including neurodegenerative diseases or metabolic disorders, are still unsolved because of the inability to selectively target specific forms of biomolecules or their aggregates. However, most biomolecules, like proteins or DNA, present chirality, which can be used to detect them selectively. One of the ways to do that is by studying the chiral optical properties emerging upon assembling these chiral organic molecules and inorganic matter, like gold nanoparticles. By analyzing these optical properties one could understand the nature of the mutual interactions between the gold nanoparticle and surrounding chiral molecules and, as a result - develop new methods for detecting and imaging these chiral structures.

Gold nanoparticles, like plasmonic gold nanoparticles or gold nanoclusters, offer not only a variety of sizes and shapes but also high tunability of optical properties and relatively easy surface functionalization - beneficial properties in studying the interaction with chiral organic molecules and their assemblies. Their simple synthesis and high biocompatibility make them ideal candidates for studying interactions with various biomolecules. Moreover, upon mixing with chiral organic molecules, gold nanoparticles could create chiral heterostructures - a type of chiral nanomaterials characterized by new properties emerging from the mutual interactions between two or more different materials that build them. Among these emerging properties are chiral optical properties like circular dichroism or circularly polarized luminescence. Analysis of these properties allows not only to obtain information on the chirality of the tested organic molecules but also, in some cases, their structure, which enables their more selective detection. However, due to the novelty of this research area, there are still several important issues that need to be addressed:

- There are some reports on the assembly of chiral heterostructures created with plasmonic nanoparticles. However, it is still not clear what is the origin of those new properties and if they could be used for biosensing without the need for complicated helical or twisted nanoparticle assembly.
- Although there are several reported protocols of gold nanocluster chiral self-assembly, there are only a few reports on template-driven assembly of gold nanoclusters which could lead to the creation of chiral heterostructures. Thus, little is known about the interaction of nanoclusters with various template molecules, how it affects their optical properties, or what new chiral optical properties can emerge upon such assembly.
- Biomolecule-coated chiral gold nanoclusters are reported to exhibit strong chiroptical properties, but it is still not well understood if and how it affects their non-linear optical properties, which can be used for *in vivo* imaging.

Thus, my research aimed to address some of the listed issues by studying the optical properties of chiral heterostructures that combine various chiral organic molecules, like liquid crystals or proteins, and two types of gold nanoparticles – plasmonic gold nanoparticles and gold nanoclusters. For this purpose, I used numerous spectroscopic methods, such as spectrofluorometry and circular dichroism spectroscopy, and microscopic methods, such as two-photon microscopy or circularly polarized luminescence microscopy. The main hypotheses verified within this work are:

- 1. Chiral template assembled achiral plasmonic nanoparticles can exhibit strong circular dichroism without any helical arrangement of nanoparticles*
- 2. Chiral protein aggregates can be detected using their interaction with single achiral plasmonic nanoparticles, which can be probed using their circular dichroism*
- 3. The same type of surface-functionalization and gold-template interactions can be used to helically assemble plasmonic nanoparticles and ultra-small gold nanoclusters*
- 4. Helical assemblies of gold nanoclusters created using liquid-crystal templates can exhibit circularly polarized luminescence*
- 5. Arginine-coated gold nanoclusters can emit two-photon excited circularly polarized luminescence*

Abbreviations

1PL – one-photon excited luminescence

2PL – two-photon excited luminescence

2PM – two-photon excited fluorescence microscopy

TPA – two-photon absorption

ABS - absorbance

AuNCs – gold nanoclusters

AuNPs – gold nanoparticles

AuNRs – gold nanorods

AuBPs – gold bipyramids

ATT - 6-Aza-2-thiothymine

Arg – arginine

BSA – bovine serum albumin

CD – circular dichroism

CPL – circularly polarized luminescence

Cys - cysteine

GSH - glutathione

OIM - 1,3-phenylenebis[4-(4-oleyloxyphenyliminonetyl)benzoate], oleylo-imino matrix

HNF – helical nanofilaments

PL – photoluminescence

QDs – quantum dots

Literature review

I. Studies on chirality and its impact on society

The asymmetry of various molecules and structures in Nature is one of the most important topics related to the origin of life in our universe. From the chirality of amino acids and sugars to the helical structures of DNA, chirality plays a crucial role in the molecular architecture of life. In order to understand it, it is important to investigate the significance of chirality at the nanoscale – the scale at which basic elements of living organisms, such as proteins or DNA helices, interact with each other and other structures. Understanding how chirality emerges and is sustained at the nanoscale could provide essential insights into the mechanisms that govern prebiotic chemistry and the origins of life on Earth. Moreover, it might also open new avenues for solving scientific problems in fields such as drug design, catalysis or advanced materials. Many chiral molecules interact with polarized light in a selective manner, depending on their chiral configuration, resulting in chiroptical properties such as circular dichroism or circularly polarized luminescence. By exploring these properties we can understand how such interaction influences their structure and interactions with the surrounding environment. What is important, the study of chirality at the nanoscale has already had a profound impact on various aspects of modern science and everyday life, revolutionizing a few well-known fields like pharmacy, display technology, the food industry and agriculture.

II. Chiral heterostructures – the versatile chiral nanomaterials

II.1 Chiral nanomaterials

Nanomaterial could be defined as a material with sizes up to 100 nm in at least one dimension. They constitute a bridge between bulk (>100 nm) and molecular materials. Due to the nanometric size constriction, they possess unique physical and chemical properties, which can be further tuned by modifying their shape, size or environment, opening a myriad of possible applications. One of the most interesting types of such materials are chiral nanomaterials, which selectively interact with an electromagnetic wave depending on the direction of its circular polarization.

Chiral nanomaterials offer several advantages, making them valuable for a range of applications (Figure 1). Molecular optical properties are related to electronic transitions between two molecular states, most commonly highest occupied molecular orbital (HOMO) and lowest unoccupied molecular orbital (LUMO). The energy of these transitions usually corresponds to the ultraviolet (UV) range of wavelengths. In the case of nanomaterials, electronic transitions could be easily tuned in a much broader wavelength range, spanning from UV, through the visible (VIS) range and up to the near-infrared (NIR). Such tunability also applies to the magnetic and electronic behavior of nanomaterials, which is useful in designing advanced materials for spintronics or data storage devices.^{1, 2} Moreover, chiral nanomaterials exhibit stronger interaction with circularly-polarized light than most of bulk and molecular materials.³ Their high surface-to-volume ratio gives chiral nanomaterials a significant advantage in catalysis, allowing for highly selective and efficient reactions, especially in enantioselective processes.⁴ Due to their unique interactions with polarized light and chiral molecules, they enhance the sensitivity and selectivity of sensors for detecting biomolecules or drugs.^{5, 6} In addition, many chiral nanomaterials can be engineered for compatibility with biological systems, supporting applications in drug delivery, bioimaging, and disease diagnosis.⁷ In the end, chiral nanomaterials could self-assemble into complex structures, offering diverse options for materials design and the potential to build hierarchical structures, applicable in materials science.^{8, 9} These advantages position chiral nanomaterials as a transformative class of materials in cutting-edge research and technology across numerous industries.

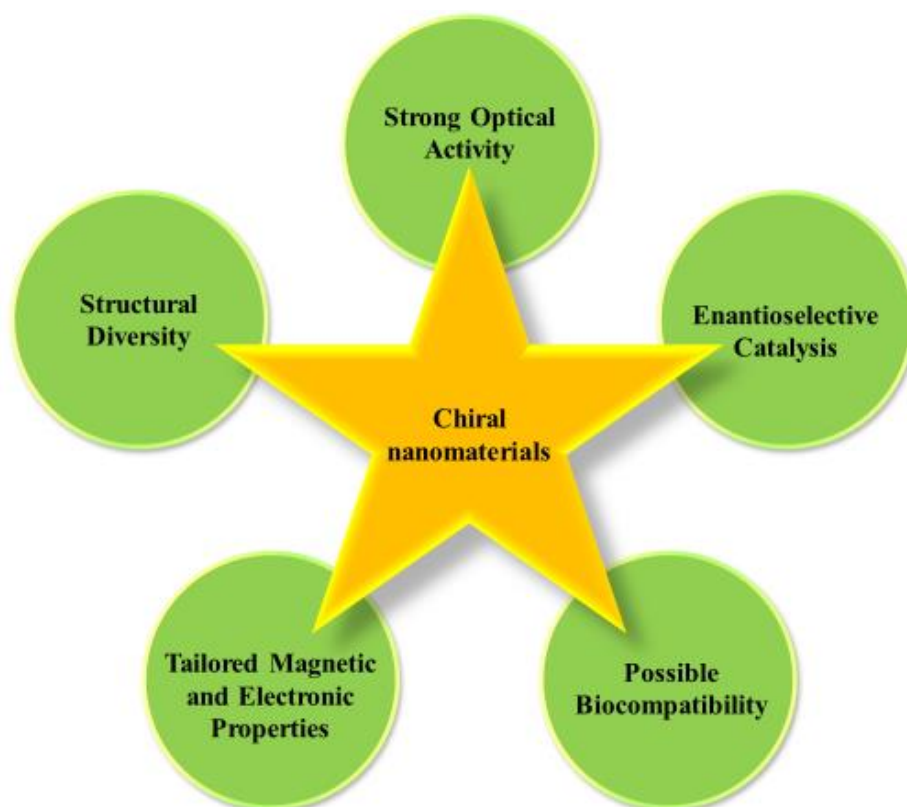


Figure 1. Main advantages of chiral nanomaterials.

Chiral nanomaterials can be categorized based on their composition and structure. They could be divided into:

- Chiral plasmonic nanostructures (examples: helical assemblies of gold nanorods)⁶
- Chiral semiconductor nanoparticles (examples: CdTe quantum dots with chiral ligands)¹⁰
- Chiral Metal–Organic Frameworks (MOFs) (examples: Zn-based or Cu-based MOFs with amino acid ligands)¹¹
- Chiral Polymer-Based Nanostructures (examples: chiral block copolymers, Polylactic acid (PLA) nanoparticles)¹²
- Chiral Carbon Nanostructures (examples: chiral carbon dots)¹³
- Chiral Supramolecular Assemblies (examples: helices, micelles, and vesicles formed by chiral peptides or amphiphiles)¹⁴
- Chiral Dielectric Nanostructures (examples: silicon-based chiral metasurfaces)¹⁵
- Chiral Hybrid (Organic-Inorganic) Nanostructures (examples: chiral cellulose films conjugated with gold nanoparticles)¹⁶

Each of these types of chiral nanomaterials leverages unique structural and compositional properties to interact with light, molecules, or magnetic fields in distinct ways, enabling a wide range of applications in optics, catalysis, sensing, and beyond.

One of the most explored topics concerning chiral nanomaterials is understanding the processes underlying their chiral properties. Three major mechanisms used to induce the chirality in

nanomaterials are intrinsic chiral geometry, chiral ligands, and assembly. The intrinsic chiral geometry could be observed from nanostructures with helical or twisted shapes, which exhibit chirality due to their asymmetric 3D configurations. The examples are chiral protein aggregates (amyloids)¹⁷ or gold helicoids¹⁸. On the other hand, functionalizing the geometrically achiral nanostructures with chiral ligands, due to its universality and a large pool of chiral ligands, is frequently used for various types of nanoparticles with different morphologies. It leads to a chiral arrangement of atoms and, as a result, creates a chiral surface. The examples are chiral thiol-capped quantum dots¹⁹ or arginine-capped gold nanoclusters²⁰. The last widely used mechanism is inducing the chiral effects in nanomaterials via their assembly. The assembly could be self-directed or template-directed. The self-directed assembly could be mediated by small ligands attached to the nanoparticle surfaces, which interact with each other, creating complex helical hierarchical structures.²¹ Moreover, Kotov *et al* have proved that the self-assembly could also be directed by circularly polarized light.²² The template-assisted assembly requires the usage of chiral templates like proteins,²³ DNA²⁴ or liquid crystals²⁵. The application of templates provides spatial control over the arrangement of nanoparticles, allowing the formation of highly ordered chiral structures with precise configurations. Moreover, it enables precise tuning of the optical properties, making it beneficial for applications in plasmonic and photonic devices.²⁶

II. 2 Chiral heterostructures – highly adaptable nanomaterials

Chiral heterostructures are a unique subset of chiral nanomaterials that combine distinct nanoscale layers or components into a single cohesive material. Unlike single-component chiral nanostructures, chiral heterostructures integrate different types of materials (such as metals, semiconductors, or organic compounds) with varying electronic, optical, or catalytic properties. A heterostructure could be defined as any structure composed of two or more materials that are physically or chemically bonded.²⁷ At the nanoscale, heterostructures could be made from two different nanomaterials belonging to the same class (examples: metal-metal²⁸, semiconductor-semiconductor²⁹) or two different classes (examples: metal-semiconductor³⁰, metal-organics³¹). Materials that build heterostructures can mutually influence each other, strongly modifying their physicochemical properties. With a thorough understanding of the mutual interactions, such modification could be controllable.³²⁻³⁴ Furthermore, the creation of heterostructure could result in the emergence of new properties. Good examples are chiral heterostructures, starting to exhibit chiral optical properties only after the heterostructure assembly.^{25, 35} Although, the most important feature of chiral heterostructures is the adaptability they could gain via the modification. By modifying the sequence, thickness, or material composition, researchers can tailor the optical, magnetic, and electronic properties of the heterostructure. This flexibility makes chiral heterostructures particularly suitable for applications that require specific chiroptical characteristics, such as circularly polarized light emission or enantioselective catalysis. The tunable nature of these heterostructures enables customization for specific functionalities, which is difficult to achieve with single-component chiral nanomaterials. For example, combining metallic or semiconductor nanoparticles with various biomolecules could strongly enhance their biocompatibility, increasing their application potential in fields like biosensing, bioimaging or photodynamic therapy.³⁶ Mixing the semiconductor nanoparticles with metallic ones increases their electronic performance, which could be used in fields like

solar cells or photocatalysis.³⁰ Chiral heterostructures also demonstrate unique optical phenomena such as enhanced circular dichroism and circularly polarized luminescence, which are critical for advanced photonic and sensing applications. These optical properties are often stronger than those observed in single-component chiral materials making chiral heterostructures invaluable in developing highly sensitive optical sensors and devices for detecting molecular chirality, with potential applications in pharmaceuticals and environmental monitoring.

In summary, chiral heterostructures represent an advanced approach to chiral nanomaterials, combining the advantages of multiple components to achieve tunable, multifunctional, and robust materials. Their unique layered design allows for enhanced performance in applications requiring specific chiroptical properties and stability, positioning them as promising candidates for next-generation technologies in sensing or catalysis.

II. 3 Fabrication techniques for chiral heterostructures

Fabrication techniques for chiral heterostructures are diverse and evolving, combining precise nanoscale assembly methods with materials engineering to create structures with unique chiroptical properties. One primary approach is **template-assisted assembly**, which uses templates such as DNA,³⁷ cellulose nanocrystals,³⁸ or other organic molecules²⁶ to guide the organization of nanoparticles into chiral configurations. Another prominent technique is **bottom-up self-assembly**, which allows the spontaneous organization of chiral molecules or nanoparticles into larger, ordered chiral heterostructures.^{39, 40} This approach leverages molecular interactions, such as van der Waals forces, hydrogen bonding, or electrostatic forces, to promote chiral assembly. This has been used in materials like cellulose nanocrystals to assemble metallic nanoparticles into chiral arrangements for sensing applications.⁴¹ In addition, there are **top-down nanofabrication techniques**, including electron-beam lithography.⁴² These approaches involve physically patterning materials on a substrate to produce nanoscale chiral patterns. For example, electron-beam lithography can carve chiral patterns into a substrate, onto which other materials can be deposited to create heterostructures with tailored chiral optical responses. This method has been used to create chiral meta-surfaces that enhance circularly polarized light interactions and are highly applicable in advanced photonics. In the end, **layer-by-layer assembly** methods allow researchers to precisely control the sequence of materials in chiral heterostructures, leading to highly customizable properties. For instance, alternating layers of chiral polymers and metal nanostructures can be assembled to amplify the chiral optical response and achieve greater control over the resulting heterostructure's properties.^{43, 44} Each of these fabrication techniques offers unique advantages for controlling the chiral and optical properties of heterostructures, making them applicable across various fields. This versatility, combined with the precision achievable through these methods, positions chiral heterostructures as a promising platform for next-generation materials in advanced technologies.

II. 4 Chiral templates used in chiral heterostructure

One of the most interesting types of chiral heterostructures is the one created by connecting chiral templates and achiral nanoparticles. As mentioned previously, chiral templates could be used as an assembly directing factor guiding the organization of nanoparticles into chiral configurations and enabling the production of nanostructures with distinct optical and electronic properties. In this chapter, some of the types of templates and their properties will be discussed.

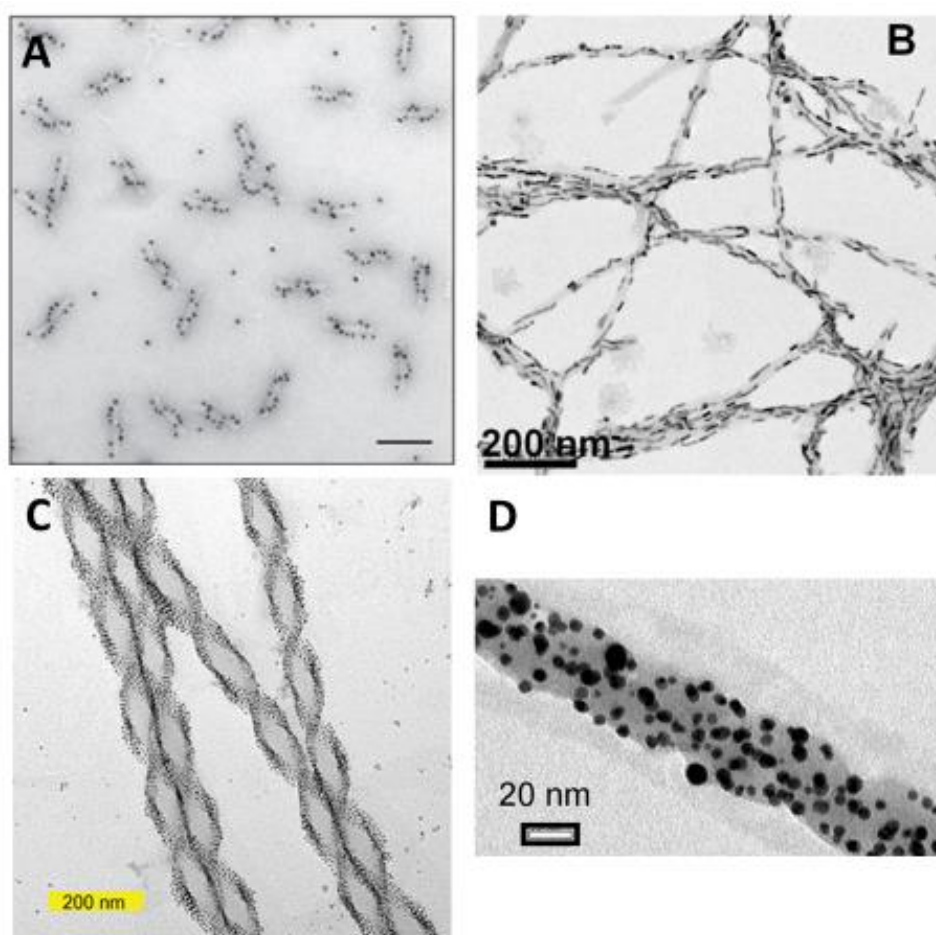


Figure 2. Types of chiral templates used in template-assisted assembly of chiral heterostructures. (a) DNA (scale bar, 100 nm), reprinted from reference no.⁴⁵ (<https://doi.org/10.1038/nature10889>) with permission from Springer Nature. (b) Alpha-synuclein amyloids, reprinted from reference no.⁴⁶ (<https://doi.org/10.1073/pnas.1721690115>). Copyright © 2018 National Academy of Sciences. (c) Liquid crystalline helical nanofilaments, reprinted from reference no.³⁵ (<https://doi.org/10.1002/adma.201904581>) under Attribution-ShareAlike 4.0 International license (CC BY-SA 4.0). (d) Silica nanohelices, reprinted with permission from reference no.⁴⁷ (<https://doi.org/10.1021/jp307784m>). Copyright © 2012 American Chemical Society.

1. Deoxyribonucleic acid (DNA)

DNA is a molecule that carries the genetic instructions used in the growth, development, functioning, and reproduction of all living organisms. It is made up of two long amino acid strands, held together by hydrogen bonds between the appropriate nitrogenous bases, that form a characteristic double helix structure. In the context of chiral nanomaterials, DNA is a well-

studied template material as evidenced by a few extensive review articles published in the last 10 years.⁴⁸⁻⁵⁰ It was used to helically assemble the nanomaterials like noble metal nanoparticles (Figure 2a),⁴⁵ semiconductor nanoparticles⁹ or silver nanoclusters⁵¹. Moreover, DNA enables highly precise control over the chiral optical properties of molecules and materials across multiple length scales, from nanometers to micrometers due to DNA programmable structure, with customizable base sequences and tailorable length.⁵⁰

2. Proteins and their aggregates

Another often applied templates in chiral heterostructures are various proteins. Their chiral nature, originating from the arrangement of amino acids in specific secondary and tertiary structures (e.g., helices, sheets), allows them to guide the assembly of nanomaterials with well-defined handedness (chirality). Proteins can be applied as chiral templates for materials such as metallic nanoparticles⁵² or semiconductor quantum dots⁵³. One of the most important features of protein templates is an interaction between the protein and nanomaterials, which can induce chirality in the structure, even without their chiral arrangement. Govorov *et al.* reported that chiral proteins can induce circular dichroism in neighbouring metallic nanoparticles via dipole-dipole interaction between the chiral protein and chiral nanoparticle (dipole-coupling).^{54, 55} Moreover, proteins offer specific binding sites that can recognize and interact with certain chemical groups promoting the selective interactions and alignment of nanoparticles.⁵⁶ In addition, nanoparticles could interact with ordered protein aggregates. An example of such structures are amyloids, associated with diseases such as Alzheimer's or Parkinson's with characteristic fibrillar morphology composed of tightly packed, beta-sheet structures, making amyloids highly stable and resistant to degradation.⁵⁷ Kumar *et al* reported the chiral heterostructures made of gold nanoparticles helically assembled using the alpha-synuclein amyloids (Figure 2b).⁴⁶

3. Chiral liquid crystals

Liquid crystals (LCs) are a unique state of matter that exhibit properties intermediate between those of conventional liquids and solid crystals. These materials consist of anisotropic molecules that, while behaving like liquids, can exhibit long-range orientational or positional order similar to crystalline materials. Moreover, liquid crystals can undergo transitions between different phases characterized by different physical properties depending on external conditions like temperature (thermotropic liquid crystals) or solvent concentration (lyotropic liquid crystals). What is most important from the perspective of chiral nanomaterials, studies have demonstrated that both thermotropic and lyotropic liquid crystals can exhibit chiral mesophases.^{58, 59} Kumacheva *et al.* reported that such chiral cholesteric films formed by cellulose nanocrystals could be used to assemble plasmonic nanoparticles, inducing strong circular dichroism.⁶⁰ Furthermore, some of the thermotropic liquid crystals could transition into helical nanofilament (HNF) phase, allowing creation of nanoparticle-coated helical nanofilaments upon the co-assembly with metallic nanoparticles, as reported by Lewandowski *et al* (Figure 2c).³⁵

4. Silica nanohelices

A silica nanohelix is a helical nanostructure made of silica (SiO₂) that exhibits chiral properties due to its geometry. These structures are typically on the nanoscale, with dimensions and helical pitches (distance between two points on a helix separated by a one complete helix turn) that can be carefully controlled during the fabrication. Chiral silica templates or silica nanohelices provide impressive durability and customizable surface properties, making them excellent for creating hybrid materials. For example, Oda *et al.*, demonstrated using transmission electron microscope (TEM) imaging that chiral silica nanohelices can strongly interact with gold nanoparticles of various sizes and assemble them upon functionalization of both silica and nanoparticles surface with the same ligands - 3-aminopropyl)triethoxysilane (APTES) or (3-mercaptopropyl)triethoxysilane (MPTES) (Figure 2d).⁴⁷ It was also reported that silica could induce chiroptical properties in non-metallic nanomaterials: Liu *et al.*⁶¹ showed that silica nanoribbons could induce circular dichroism in CdSe nanocrystals upon their template-assisted chiral assembly and Oda *et al.*⁶² reported that silica nanohelices could induce CD signal in perovskite CsPbBr₃ nanocrystals.

In the end, it is also worth noting, that template-assisted methods for fabricating chiral nanostructures offer several advantages over other methods. Templates like liquid crystals could ensure precise control over the properties of assembled heterostructures. For example, liquid crystalline helical nanofilaments could create chiral domains of different handedness which, upon co-assembly with gold nanoparticles, results in their switchable chiroptical properties.³⁵ The other benefit of using templates is their versatility. Cheng *et al.* showed that one template (silica nanohelices) could be used to helically assemble gold nanoparticles ranging in size from 4 nm to 10 nm.⁶³

II. 5 Chiroptical properties of chiral heterostructures

As mentioned in the previous chapters, assembling of chiral heterostructures often leads to new emerging chiroptical properties. The most common ones are circular dichroism or circularly polarized luminescence.

Circular dichroism (CD) results from the difference (ΔA) between the material absorbance of left-handed circularly polarized (LCP) and right-handed circularly polarized (RCP) light.

$$\Delta A = A_{LCP} - A_{RCP} \quad \text{Eq. 1}$$

It could also be expressed as the difference between the material extinction coefficients for LCP and RCP light:

$$\Delta A = A_{LCP} - A_{RCP} = (\varepsilon_{LCP} - \varepsilon_{RCP}) \cdot c \cdot l \quad \text{Eq. 2}$$

Where ε is the molar extinction coefficient, c is the molar concentration of the sample and l is the length of the measurement cell path. However, most measurements are reported as molar ellipticity, calculated using the equation:

$$[\theta] = 3298.2 \cdot (\varepsilon_{LCP} - \varepsilon_{RCP}) \quad \text{Eq. 3}$$

CD amplitude depends on external factors such as sample molar concentration and the cell path length, thus it is often problematic to compare the strength of this optical property between different materials, differing significantly in concentration. To address that issue, one could calculate the dimensionless dissymmetry factor g_{abs} (eq. 4) by normalizing the CD amplitude by the average absorbance.

$$g_{abs} = \frac{\Delta A}{A} = 2 \cdot \frac{A_{LCP} - A_{RCP}}{A_{LCP} + A_{RCP}} \quad \text{Eq. 4}$$

From the theoretical point of view, CD could be described as polarization-dependent electronic transitions from the ground states to excited states. Moreover, it could be expressed as the enantioselective absorption resulting from the interference of the electric ($\vec{\mu}$) and magnetic (\vec{m}) dipole transition moments:

$$CD \propto \text{Im}[\vec{\mu} \cdot \vec{m}] \quad \text{Eq. 5}$$

Since the CD response results from light absorption, the CD amplitude and spectral position could be used to analyze the polarization sensitivity of electronic transitions from the ground to excited states. CD bands of organic molecules, like proteins and other biomolecules, are often located in the ultraviolet region.⁶⁸ Meanwhile, bands of inorganic nanoparticles tend to span from UV to the lower energetic end of the visible range.⁷ In the case of metallic nanoparticles, this range could be extended to infrared.⁶⁹ For other inorganic nanomaterials, infrared is often accessible only via their chiral self-assembly.⁷⁰ The main advantages of this technique are non-destructive and simple sample preparation, fast measurement speed, and relatively low cost of CD instruments, making it accessible for a wider range of laboratories. Moreover, CD spectra can provide quantitative data regarding the amount of secondary structural elements in a sample, such as the fraction of beta-sheets building the analyzed proteins. CD is also one of the most common chiroptical properties exhibited by the chiral heterostructures made from templates discussed in the previous chapter. Kuzyk *et al* reported CD spectra of two types of gold nanoparticle helices made using DNA origami.⁴⁵ They discovered that helices assembled using 16 nm (diameter) nanoparticles exhibited two orders of magnitude stronger signal than smaller, 10 nm nanoparticles, due to plasmonic enhancement. Mandal *et al* generated a strong CD response from the amyloid-templated chiral plasmonic nanostructures.⁶⁴ They showed that by modifying the concentration of gold nanorods conjugated to BSA amyloid fibrils, they can manipulate the strength of the induced plasmonic CD response up to hundreds of mdeg. Grzelak *et al* presented that liquid crystalline nanohelices coated with gold nanoparticles exhibit tunable plasmonic circular dichroism: the strength of CD signal increased while increasing the content of gold nanoparticles.²⁵ Moreover, the handedness of the signal was switchable by exchanging one chiral dopant substance (dopS) to another (dopR). Cheng *et al* reported CD response from the “Goldhelices” created from silica nanohelices and plasmonic gold nanoparticles.⁶³ They showed that CD signal strength increases with increasing size of nanoparticles (from 5.7 nm to 9.8 nm diameter) and that nanoparticles coating the nanohelices of opposite handedness exhibit reversed CD spectra. By summing up the cited studies, one can conclude that the strength of the CD response depends on the nanoparticle size or concentration and the sign of signal often follows the template handedness.

Circularly polarised luminescence (CPL) is an optical phenomenon where chiral materials emit luminescence that has a preferred circular polarization, either left- or right-handed. The CPL signal is also often expressed as the difference between the intensity of left-handed (I_{LCP}) and right-handed (I_{RCP}) circularly polarized luminescence emitted by the material:

$$\Delta I = I_{LCP} - I_{RCP} \quad \text{Eq. 6}$$

To compare the strength of the CPL signal among various nanomaterials, one could use the dimensionless luminescence dissymmetry factor g_{lum} (eq. 7), calculated similarly to g_{abs} , by normalizing the CPL amplitude by the average circularly polarized luminescence intensity.

$$g_{lum} = \frac{\Delta I}{I} = 2 \cdot \frac{I_{LCP} - I_{RCP}}{I_{LCP} + I_{RCP}} \quad \text{Eq. 7}$$

Theoretically, the luminescence dissymmetry factor is proportional to the θ angle between the magnetic and electric transition moments and could be defined as:

$$g_{lum} = 4 \cos \theta \frac{|\vec{m}| \cdot |\vec{\mu}|}{|\vec{m}|^2 + |\vec{\mu}|^2} \quad \text{Eq. 8}$$

CPL is a less frequent property of chiral heterostructures than CD, as many of the studied nanomaterials are not luminescent. The most common type of CPL active materials are made according to the rule - chiral host–achiral luminescent guest.⁶⁵ Naito *et al* reported that semiconductor CdS quantum dots embedded inside a chiral protein cage made of ferritin emitted strong left-handed CPL with g_{lum} values of magnitude 10^{-3} .⁵³ They also showed that the maximum of CPL spectra could be shifted by changing the nanoparticle size due to photoetching, resulting in tunability of the discovered chiroptical property. Additionally, Parzyszek *et al* reported that CPL spectra from other semiconductor quantum dots (InP/ZnS) co-assembled with liquid crystal nanohelices could also be tuned by changing the ratio between the content of nanoparticles and liquid crystal matrix.⁶⁶ Increasing the number of QDs shifted the luminescence maxima toward longer wavelengths (from 590 nm to 620 nm), but lowered the luminescence dissymmetry factor g_{lum} from 0.005 to 0.002. Liu *et al* showed that CPL with a $g_{lum} \sim 10^{-3}$ could also be emitted by luminescent perovskite CsPbBr₃ nanocrystals helically arranged on silica nanohelices.⁶² Moreover, the sign of the CPL signal depended on the handedness of silica nanohelices, leading to the emission of left-handed CPL from assemblies with R-silica helices and red-handed CPL from assemblies with L-silica helices. Ultimately, CPL-active chiral heterostructures could also be created using gold nanoclusters. Zhang *et al* reported that, under suitable conditions, gold nanoclusters co-assembled with cellulose nanocrystals emit strong left-handed CPL with a maximum of around ~700 nm with g_{lum} up to 0.287.⁶⁷ Taking all of that into account, it could be concluded that CPL of the chiral heterostructures depends on the factors like nanoparticle size, achiral guest/chiral host ratio and handedness of the chiral host matrix. In addition, the biggest advantage of CPL spectroscopy is its versatility - CPL measurements can be taken in solution, in the solid state, or within biological samples, providing flexibility across various sample types.

II. 6 Applications

Chiral nanomaterials, with their unique asymmetrical structures and optical properties, have emerged as a cornerstone in various advanced technologies, offering solutions to challenges in fields ranging from healthcare to catalysis.

The most explored field of applications is biomedicine.^{7, 72} Chiral nanomaterials, due to their structure and properties, could interact with various biomolecules in an enantioselective manner, which can be used in therapy. For example, chiral glutathione-capped gold nanoparticles could be used to prevent the aggregation of amyloid beta proteins, directly connected with Alzheimer's disease (Figure 3a, third and fourth row of images from the confocal microscope shows lower amyloid concentration in samples with nanoparticles).⁷³ Furthermore, D-glutathione (GSH) capped nanoparticles demonstrated a stronger binding affinity to amyloid beta monomers, contributing to more effective inhibition of fibril formation, highlighting the impact of chirality on nanoparticle functionality. Chiral organic-inorganic nanomaterials could also be applied in therapy thanks to the combination of biomolecule affinity and nanoparticle optical properties. Sun *et al* reported that chiral semiconductor nanoparticles (cysteine-modified CdTe) can specifically cleave 90 base pairs from the DNA strand because of the affinity between cysteine and specific DNA sequence and using the photoinduced reactive oxygen from the nanoparticles.⁷⁴ Also chiral heterostructures, such as DNA-driven chiral silver-gold nanostructures, showed a possible application in photodynamic therapy as they were reported to generate reactive oxygen species under circularly polarized light illumination.⁷⁵

Chiral template-directed heterostructures also enable sensitive detection of various chiral biocomponents. Wang *et al* presented that L- and D-penicillamine coated gold nanoparticles adsorbed chiral bovine serum albumin molecules in different orientations, confirmed by more negative charges exposed after binding to D-penicillamine AuNPs. Kumar *et al* reported that gold nanorods could be used to detect amyloid fibrils connected to Parkinson's disease since their mutual interaction leads to amyloid-driven helical assembly of nanoparticles resulting in circular dichroism (Figure 2b).⁴⁶ Using DNA as a chiral host material for gold nanorods assembly, Mu *et al* demonstrated that DNA concentration of the host material correlates with the strength of circular dichroism exhibited by the assembled nanostructures and the system could detect even the concentrations as low as 3.7 attomoles (Figure 3b).⁷⁶ Xu *et al* showed that gold nanoparticles functionalized with chiral L- and D- cysteine molecules led to the creation of nanoparticle dimers with CD signal dependent on the cysteine concentration and detection sensitivity of 20 pM.⁷⁷ Ngamdee *et al* developed a biosensor of glucose based on chiral CdS nanoparticles.⁷⁸ The sensing mechanism was also based on CD signal dependence on the concentration of glucose and was highly selective, showing much lesser affinity to other studied saccharides (Figure 3c). Other promising materials are DNA-templated chiral nanomaterials which detected intracellular microRNA in real time using plasmonic CD, inside the living cells⁷⁹

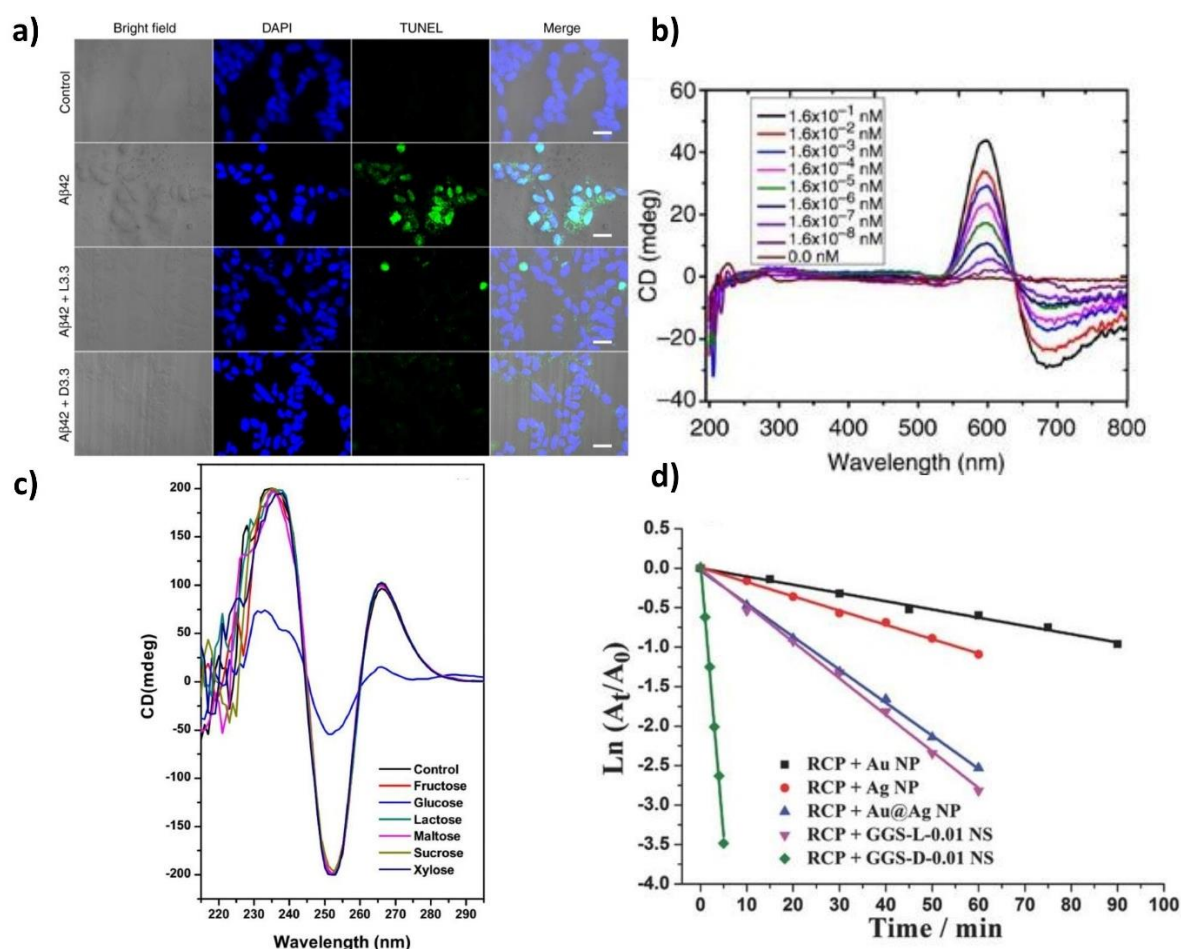


Figure 3. Exemplary applications of chiral nanomaterials. (a) Images from bright-field and confocal microscopes presenting the SH-SY5Y cells treated with A β 42 amyloids in the absence and presence of L-glutathione (L3.3) and D-glutathione (D3.3) stabilized gold nanoparticles. Scale bars, 50 μ m. Reprinted from reference no.⁷³ (b) CD spectra of gold nanorod assemblies obtained with different DNA concentrations, reprinted from reference no.⁷⁶ (c) CD spectra of D-penicillamine/Cysteine coated CdS quantum dots in the absence and presence of different types of sugar, reprinted from reference no.⁷⁸ (<https://doi.org/10.1016/j.snb.2018.08.005>), copyright © 2018, with permission from Elsevier. (d) Photocatalytic activity evaluation of gold-gap-silver nanostructures by monitoring the changes in absorption intensities (A_t/A_0) of 4-nitrophenol during the reduction by sodium borohydride. Au NPs, Ag NPs, Au@Ag NPs denote gold nanoparticles, silver nanoparticles and gold-silver nanoparticles without the gaps, respectively. Reprinted from reference no.⁸⁰ (<https://doi.org/10.1002/adfm.201502429>), copyright © 2015, with permission from Wiley.

Another application of chiral nanomaterials is chiral catalysis. One of the examples is chiral gold-gap-silver nanostructures, reported to exhibit photocatalytic activity under left-circularly polarized light irradiation, 71 times stronger than for gold nanoparticles studied in the research (Figure 3d).⁸⁰ The photocatalytic activity was monitored using the reduction of 4-nitrophenol to 4-aminophenol. Photocatalytic properties were also reported for quantum dots made of copper sulfide and functionalized with chiral L-/D-penicillamine ligands.⁸¹ Under irradiation with circularly polarized light, they produced hydroxyl radicals, used to cleavage proteins such as bovine serum albumin or human serum albumin. Not only colloidal materials, but also chiral films presented photocatalytic properties. Xu et al presented that chiral films

made of gold nanoparticles functionalized with L- and D-phenylalanine could be used for selective photooxidation of L- and D-glucose.⁸²

Overall, the diverse applications of chiral nanomaterials underscore their transformative impact across scientific disciplines, driven by their unique physical, chemical, and biological properties. Their continued development promises groundbreaking advancements in technology, healthcare, and sustainability.

III. Plasmonic gold nanoparticles

The term "gold nanoparticles" could be used to describe all colloidal materials built of gold atoms with a size between 1 and 100 nanometers in at least two dimensions. At this size, they exhibit unique physical and chemical properties that distinguish them from bulk gold, which arise due to quantum nanometer size effects. Gold nanoparticles consist of a core of gold atoms surrounded by a stabilizing layer of organic molecules or surfactants, which prevent aggregation and enhance stability in various media. Their synthesis can be achieved through chemical, physical, or biological methods, with chemical reduction being the most common. Gold nanoparticles can take different shapes – eg. spherical, rod-like, cubic, and star-shaped. Gold is inherently inert and resistant to oxidation, ensuring the stability of nanoparticles under various conditions. Moreover, the surface of AuNPs can be easily modified with various ligands, providing a platform for targeted interactions. Functionalized AuNPs can also exhibit excellent biocompatibility, allowing their safe use in biological and medical applications. Additionally, from the economic perspective, the small amounts required for AuNP-based technologies make them economically viable and their potential for green synthesis and use in sustainable energy solutions aligns with global environmental goals. However, the most important features of gold nanoparticles, from this work's perspective, are their unique optical properties connected to the electronic configurations and tailorable by modifying their size, shape, and environment. They could be divided into two categories characterized by distinct properties – plasmonic gold nanoparticles and gold nanoclusters.

III. 1 Synthesis of plasmonic gold nanoparticles

Although plasmonic gold nanoparticles could be synthesized using various methods such as photolithography or laser ablation, the most regarded one, is chemical synthesis.⁸³ The standard chemical synthesis of isotropic gold nanoparticles begins with the reduction of gold ions Au^{3+} present in the precursor (gold salt solution) to Au^0 using the reducing agent (borohydrides or citrate). Then, the solution of stabilizing/capping agents is injected into the solution to prevent gold particles from excessive aggregation leading to precipitation. By modifying the ratio between the concentration of precursor and stabilizing agents, the size of nanoparticles could be controlled. However, the synthesis of gold nanoparticles with different shapes, like anisotropic gold nanoparticles, requires a more complex synthesis procedure, like seed-mediated synthesis.

Seed-mediated synthesis consists of two main steps: preparing a gold seed solution and nanoparticle growth under appropriate conditions by mixing the seed solution with the growth solution. The typical seed solution is prepared by the swift reduction of HAuCl_4 using sodium borohydride in the presence of CTAC (cetyltrimethylammonium chloride).⁸⁴ Then the seed solution is mixed with the growth solution, which should at least contain a gold salt (HAuCl_4), a surfactant (CTAB (cetyltrimethylammonium bromide) or CTAC) and ascorbic acid. The ascorbic acid reduces Au^{3+} to Au^+ , and after the addition of seed solution, catalyzes the reduction from Au^+ to Au^0 allowing to obtain larger nanoparticles. The final nanoparticle size can be modified by changing the amount of seeds in the reaction – lower seed concentration results in bigger nanoparticles.

On the other hand, the seedless growth method could be used to prepare smaller plasmonic nanoparticles. As reported in 2012 by Ali *et al.*, the application of seedless one-pot

synthesis results in monodisperse mini nanorods with average sizes below 20 nm.⁸⁵ In the seedless method, both nucleation and growth of nanoparticles occur in the same solution. It allows to omit the two-step reduction of Au³⁺ to Au⁰ by using a stronger reduction agent like NaBH₄. The reduction rate could be controlled using pH and the nanoparticle size strongly depends on the NaBH₄ and CTAB concentration.

III. 2 Optical properties of plasmonic gold nanoparticles

The basic feature of all plasmonic gold nanoparticles (AuNPs) is their localized surface plasmon resonance (LSPR). LSPR could be explained as coherent collective oscillations of the conduction electrons confined to a particle of a size comparable to the wavelength of incident light.⁸⁶ The resulting strong light-matter interaction leads to remarkable optical, electronic, and thermal properties of AuNPs. The plasmonic properties of gold nanoparticles are connected to their frequency (ω) dependant complex dielectric function $\varepsilon(\omega)$ defined as:

$$\varepsilon(\omega) = Re[\varepsilon(\omega)] + i \cdot Im[\varepsilon(\omega)] \quad \text{Eq. 9}$$

Where the real (eq. 10) and imaginary (eq. 11) parts of dielectric function could be defined using plasma frequency ω_p and relaxation frequency γ :

$$Re[\varepsilon(\omega)] = 1 - \frac{\omega_p^2}{\omega^2 + \gamma^2} \quad \text{Eq. 10}$$

$$Im[\varepsilon(\omega)] = 1 - \frac{\gamma \omega_p^2}{\omega(\omega^2 + \gamma^2)} \quad \text{Eq. 11}$$

The plasma frequency ω_p of gold nanoparticles depends on the density of mobile charge carriers n , their charge e , mass m and the relative permittivity ε_0 of free space. It can be calculated using the formula:

$$\omega_p = \sqrt{\frac{ne^2}{\varepsilon_0 m}} \quad \text{Eq. 12}$$

Meanwhile the relaxation frequency γ can be determined by measuring the electric conductivity of the material, which for gold is equal to $\gamma = \frac{1}{25 fs}$.⁸⁷ Using the presented equations, as well as the dielectric constant of nanoparticle surrounding medium $\varepsilon_m(\lambda)$ and the nanoparticle volume V_{AuNP} , one could determine the AuNPs extinction cross-section for spherical gold nanoparticle using the formula:⁸⁸

$$\sigma_{Ext}(\lambda) = \frac{18\pi[\varepsilon_m(\lambda)]^{\frac{3}{2}}}{\lambda} \cdot V_{AuNP} \cdot \frac{Im[\varepsilon_m(\lambda)]}{[Re[\varepsilon(\omega)] + 2 \cdot \varepsilon_m(\lambda)]^2 + Im[\varepsilon_m(\lambda)]^2} \quad \text{Eq. 13}$$

Analyzing the equation, one could notice that the optical extinction of plasmonic gold nanoparticles is related to its plasmonic properties, volume and surrounding medium and, thus, could be tuned by changing these properties. As a result, for every nanoparticle, LSPR is possible only at a specific frequency (excitation wavelength).⁸⁸ Optical extinction of AuNPs could be divided into two types of light-matter interactions: light scattering and light absorption. During the light scattering, the incident light is re-radiated in all directions at the same

frequency, meanwhile during light absorption, the incident light is absorbed and converted into energy, mostly in the form of heat, phonons or crystal lattice vibrations. The absorption and scattering of AuNPs depend on the particle size. When the nanoparticle size is smaller than the wavelength of incident light, the absorption is dominant.⁸⁹ However, when the nanoparticle size is comparable and bigger to the light wavelength, the scattering dominates over the absorption, inducing the red-shift of the LSPR band.⁹⁰ Moreover, the optical properties of plasmonic gold nanoparticles could be further tuned by their assembly. Plasmons on neighbouring nanoparticles could interact with each other, leading to the generation of 'hybrid' plasmon modes. As an example, Cheng *et al* reported that dimers made of gold nanospheres induce new LSPR bands, increasing their number from one band to two bands.⁹¹ The LSPR position could be tuned even further with anisotropic gold nanoparticles. Link *et al* discovered, while studying dimers of gold nanorods, that their LSPR position depends on factors such as dimer gap distance, mutual orientation angle or size mismatch between nanoparticles.⁹² Furthermore, as reported by Ma⁸ or Shinomeri,⁶⁹ assembly of plasmonic gold nanoparticles in a chiral manner could induce strong chiroptical properties.

Gold nanoparticles, due to differences in morphology, could be categorized into two groups – isotropic gold nanoparticles and anisotropic gold nanoparticles. Isotropic nanoparticles are characterized by a single extinction band and uniform properties in all directions (Figure 4, nanospheres, nanoplates, nanocages).⁸⁷ Isotropic gold nanoparticles include gold nanospheres and hollow gold nanoparticles. The LSPR of gold nanospheres is located in the visible part of the light spectrum, and could be tuned from 520 nm to 650 nm, meanwhile, the LSPR of hollow nanoparticles could be tuned from 400 nm to even 1200 nm.⁹³ Anisotropic gold nanoparticles are often characterized by two extinction bands as well as direction-dependent properties (Figure 4, nanorods, nanotriangles, nanostars). This group includes shapes like nanorods, nanobipyramids, nanostars, nanotriangles or nanoprisms. The most studied type of anisotropic gold nanoparticles are gold nanorods, due to the tunability of their optical properties from the visible range (600 nm) to near-infrared (1800 nm).⁹³

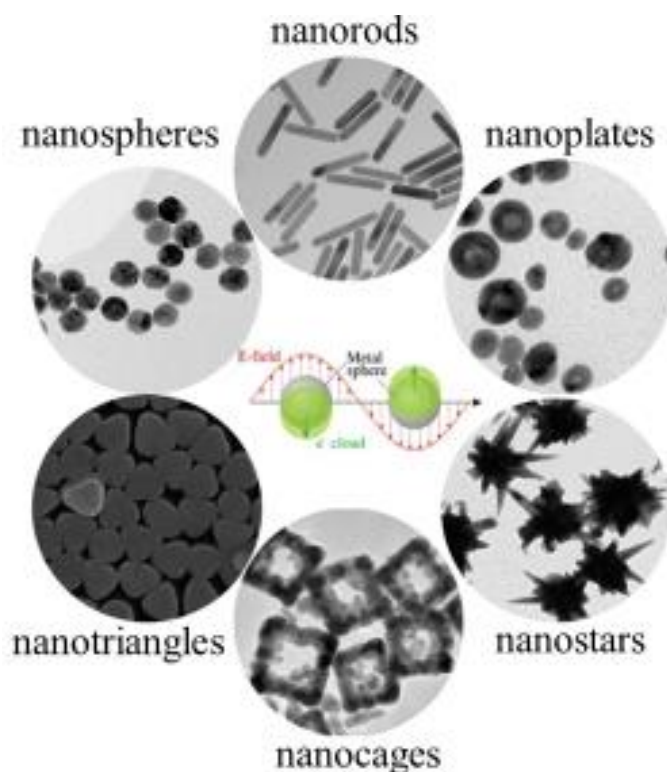


Figure 4. Various types of plasmonic gold nanoparticles and their extinction spectra. Reprinted from reference no.⁹³ (<https://doi.org/10.1016/j.jconrel.2019.08.032>), copyright © 2019, with permission from Elsevier.

III. 3 Chirality in plasmonic gold nanoparticles

Chiral plasmonic gold nanoparticles are part of the recently rapidly growing field of studies called chiral plasmonics, focusing on the idea of enhanced and tailored chiral optical responses in chiral plasmonic systems.⁹⁴

The first method inducing the chirality in plasmonic gold nanoparticles is via their chiral geometry. Chiral gold nanoparticles could have various shapes resulting in chiral properties such as helicoids⁹⁵, chiral nanorods⁹⁶, wrinkled nanorods⁹⁷, gold nanospirals⁹⁸ or nanooctopods⁹⁹. The chiral shape of a nanoparticle is often imparted using chiral molecules and biomolecules during the synthesis. For instance, chiral plasmonic helicoids reported by Lee *et al.* were synthesized with the addition of L- and D-cysteine to the synthesis reaction mixture, which allowed the creation of two types of chiral nanoparticles with enantiomeric chiroptical properties (Figure 5a).⁹⁵ The origin of chiroptical properties of single chiral AuNPs is also well understood. In 2012, Govorov *et al.* explained that the theoretical origin of single chiral gold nanocrystals with twisted and helical shapes could be attributed to the mixing of plasmonic harmonics induced by a chiral AuNP shape.¹⁰⁰

The second method of AuNP chirality induction is coupling the plasmonic nanoparticles with chiral molecules. Govorov *et al.* discovered that the strength and sign of these interactions depend on the orientation of chiral molecule electric $\vec{\mu}$ and magnetic \vec{m} dipoles in relation to the nanoparticle taking part in the dipole coupling (Figure 5b).¹⁰¹ It was confirmed by Slocik *et al.* who presented experimentally that such interactions also depend on molecule-nanoparticle distance.¹⁰² Additionally, Nesterov *et al.* proved theoretically that the chiral fields from chiral molecules are strongly enhanced while in the gap between achiral gold nanoparticles due to near-field interactions and antenna-like behavior of AuNPs.¹⁰³ It helped understand the

behavior observed during experiments with such systems, for example, two orders of magnitude enhancement of CD response from chiral cysteine molecules located in the hot spots between gold nanospheres.¹⁰⁴

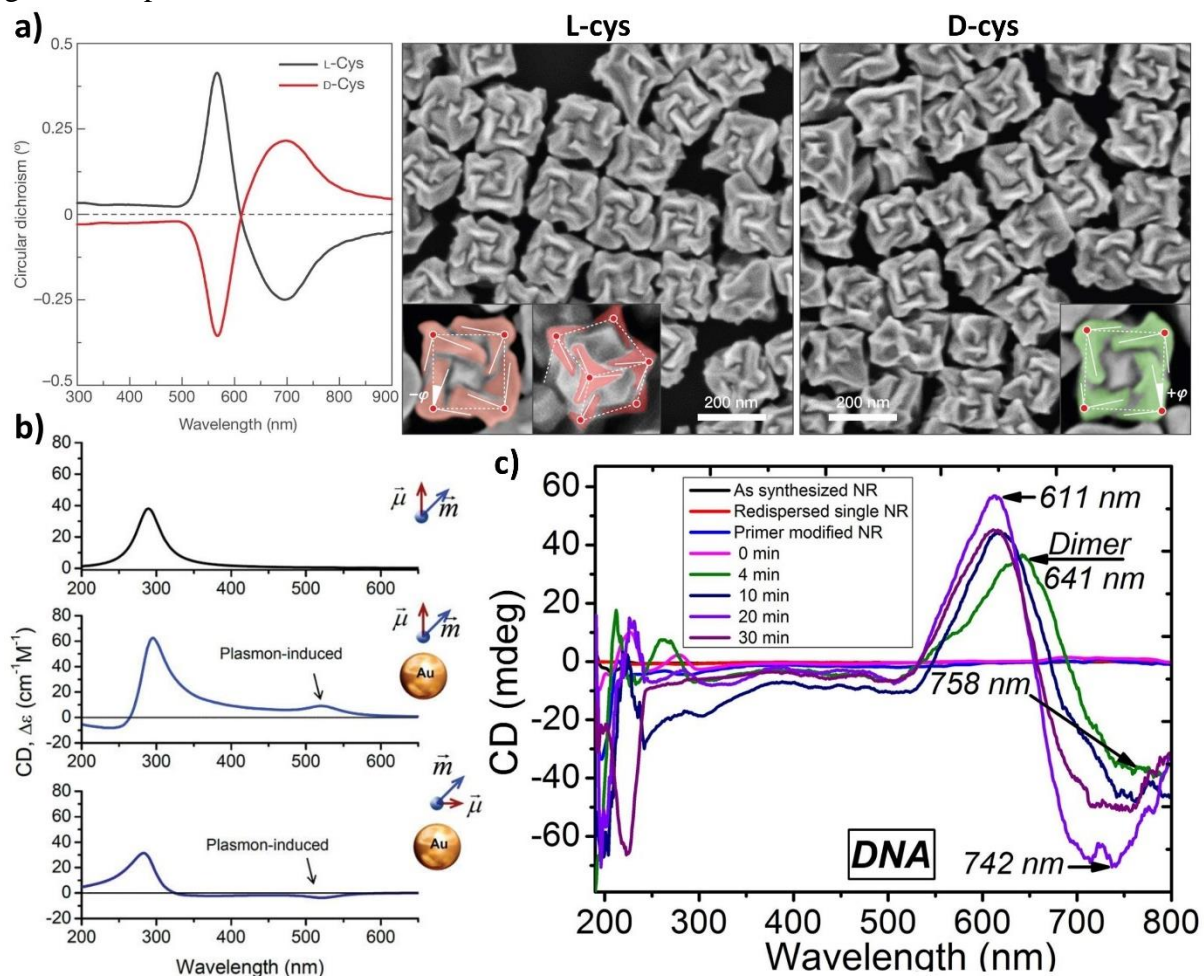


Figure 5. Various types of plasmonic gold nanoparticles and their extinction spectra. (a) Circular dichroism spectra and scanning electron microscope (SEM) images of chiral helicoids synthesized using L-cysteine and D-cysteine. Reproduced from reference no.⁹⁵ with permission from Springer Nature. (b) Circular dichroism spectra calculated for a chiral molecule and chiral molecule in the vicinity of the spherical gold nanoparticle with two different orientations of electric $\vec{\mu}$ and magnetic \vec{m} dipoles. Reprinted from reference no.¹⁰¹ (<https://doi.org/10.1021/nl100010v>). Copyright © 2010 American Chemical Society. (c) Circular dichroism spectra and TEM image of gold nanorod dimers assembled using DNA. Reprinted from reference no.⁸ under Creative Commons 4.0 Attribution-NonCommercial-NoDerivatives 4.0 International (CC-BY-NC-ND) license.

The last group of methods used to induce chirality in AuNPs is focused on their assembly. As shown by Ma *et al.*, even an AuNPs dimer with a propeller-like configuration of nanoparticles could result in their chiroptical activity (Figure 5c).⁸ Assembling methods of AuNPs are divided into self-assembly⁴⁰ and template-driven assembly²⁶. The most common self-assembly method is tip-to-tip nanoparticle linking with biological surfactants¹⁰⁵, DNA⁷⁶ or cysteine¹⁰⁶. The tip-to-tip configuration amplifies the chiroptical activity of gold nanoparticles due to the strong plasmonic coupling at the sharp tips. Moreover, it could facilitate the formation of hierarchical or superchiral structures by controlling interparticle interactions - self-assembly could be controlled using factors such as temperature¹⁰⁷ or pH¹⁰⁸. In the case of the

template-driven assembly of AuNPs, the main force that comes into play is the interactions between the nanoparticles and template molecules, enforcing their chiral arrangement. Because of that, AuNPs are often required to have the appropriate surface functionalization. Moreover, template-driven methods offer a plethora of advantages. Chen *et al.* discovered that peptide-driven assembly of gold nanoparticles is highly programmable, allowing modification of the metrics and structures of these assemblies.¹⁰⁹ In addition, using soft templates such as amyloids or liquid crystals leads to the tunable periodicity of the assembled particles due to weak and reversible interactions between template molecules and nanoparticle ligands.³⁵

III. 4 Applications of plasmonic gold nanoparticles

Plasmonic gold nanoparticles have gained significant attention for their diverse applications across science and technology due to their unique plasmonic properties. These optical characteristics enable strong near-field enhancement, biocompatibility, and tunable optical responses, making AuNPs indispensable in areas like biomedical imaging, photodynamic therapy, catalysis, and renewable energy.

For example, high scattering cross sections of bigger plasmonic nanoparticles resulted in their application in dark-field microscopy of biological tissues. Using this technique, El-Sayed *et al.* reported that plasmonic AuNPs conjugated to epidermal growth factor receptors have a higher tendency to target cancer cells compared with other cells.¹¹⁰ Moreover, because gold nanoparticles, under suitable conditions, could convert almost 100% of the absorbed energy into heat, they found an application in photodynamic therapy that could be used to destroy the targeted tumors.¹¹¹ Vankayala *et al.* presented that gold nanorods upon NIR light excitation could produce singlet oxygen which leads to the complete destruction of tumors in mice.¹¹² In addition, their high sensitivity to refractive index changes allows plasmonic AuNPs to function as sensors for detecting small environmental or biological changes. Plasmonic AuNPs have already been used as biosensors for bacteria,¹¹³ cellulose,¹¹⁴ or proteins.¹¹⁵

Gold nanoparticles can serve as effective catalysts in chemical reactions, benefiting from their high surface-area-to-volume ratio and tunable surface chemistry. Due to their plasmonic properties, AuNPs are particularly effective in light-driven catalysis. Mukherjee *et al.* showed that AuNPs templated in TiO₂ matrix could be used for dissociation of H₂ molecules on Au nanoparticles surface under illumination with visible light.¹¹⁶ AuNPs could also be used as a platform for surface-enhanced Raman scattering (SERS) to monitor the undergoing photocatalytic reactions.¹¹⁷ Gold nanoparticles, due to their ability to generate strong localized surface plasmon resonances, significantly enhance the Raman signal intensities.

Apart from medicine and catalysis, research is also being carried out on the application of plasmonic gold nanoparticles in photoelectronic devices¹¹⁸, high-frequency nanoantennas¹¹⁹ or nanolasers¹²⁰. In conclusion, these multifunctional capabilities of plasmonic gold nanoparticles position them as transformative tools across multiple disciplines. Continued advancements in their synthesis, functionalization, and understanding can unlock further applications, addressing various global challenges in healthcare, the chemical industry or electronics.

IV. Gold nanoclusters

Gold nanoclusters (AuNCs) are a group of ultra-small gold nanoparticles (often below 2 nm in diameter) made of a maximum of several hundred gold atoms. Due to their size constraint, quantum size effects come into play and the collective electron oscillations, responsible for plasmonic effects in bigger gold nanoparticles, are no longer possible.¹²¹ Instead, gold nanoclusters possess more molecule-like properties, like discrete energy levels or HOMO-LUMO electronic transitions.¹²² They could also emit strong photoluminescence in the range from ultraviolet to infrared.¹²³ Moreover, their photostability higher than in the case of many standard optical markers, makes them useful in bioimaging or biomolecule detection.¹²⁴ AuNCs could be dissolved in both organic and inorganic solvents, with water-soluble nanoclusters offering the highest biocompatibility among all types. Another great feature of gold nanoclusters is their relatively simple surface functionalization, which could highly impact and enhance their physical and chemical properties. Gold nanoclusters, due to the high surface-to-volume ratio and molecular structure, are highly sensitive to structure or composition modification.¹²⁵ Even the addition of a single atom or ligand could influence their properties. Thus, observations of transitions in the UV-Vis spectrum may reveal details about the nanocluster's composition and stability, making them a perfect platform for sensing applications. Moreover, in recent years, a lot of attention has been paid to the synthesis and properties of atomically precise gold nanoclusters, a group of nanoclusters with precisely controlled atomic structure where the number of gold atoms and ligands is strictly defined.¹²⁶ This discovery allowed scientists to understand the interactions between the nanoclusters and other molecules on the atomic level using both experimental and theoretical methods. It also allowed to better understand their interaction with light. The most studied group of gold nanoclusters are thiolate-protected nanoclusters.^{121, 127} Their structure is made of three layers: kernel gold atoms assembling the nanocluster “core”, staple-like motif of gold and sulfur atoms (-Au-S-Au-) surrounding it and stabilizing ligands. They are defined with a general formula $Au_a(SR)_b$, where a is the number of gold atoms and b is the number of surrounding ligands. Among the gold nanoclusters, thiolate-protected nanoclusters have extraordinary chemical stability and well-defined optical properties, leading to various applications.

IV. 1 Synthesis of gold nanoclusters

There are two major methodologies allowing to obtain gold nanoclusters with precisely controlled structures: the size-focusing method and the ligand exchange-induced structure transformation. Size-focusing method follows the principle of survival of the robustness – it is based upon the different stability of different sizes of nanoclusters.¹²⁸ The first step is preparing the precursor solution by dissolving the gold precursor (e.g. $HAuCl_4$) in an appropriate solvent (organic or inorganic) together with chosen ligands. Then, a reducing agent is added to the precursor-ligand solution, reducing Au^{3+} ions to metallic Au^0 atoms. The reduced gold atoms nucleate, forming polydisperse nanoclusters with a wide size distribution, and ligands prevent extensive growth and aggregation. The last step is thermodynamic control over the synthesis solution by ensuring a stable solution temperature over a prolonged time, depending on the nanocluster size. The ligand exchange-induced structure transformation enhances the size-focusing method, allowing to obtain the nanocluster sizes unobtainable by that method.¹²⁹ Step one is to obtain monodispersed atomically precise gold nanoclusters. Then, the AuNCs solution

is mixed with the appropriate ligand, having a higher binding affinity to gold atoms than initial ligands coating their surface. With time, the ligand exchange reaction follows, which could be monitored by changes in the optical properties or structural composition of AuNCs. To promote efficient ligand exchange, parameters like temperature, ligand concentration, solvent polarity, and reaction time should be carefully adjusted. The structural distortion accompanying ligand exchange allows to release or uptake of additional gold atoms and ligands. After all the initial nanoclusters are transformed, a new thermodynamically stable state is achieved in the reaction solution. It is also worth noting, that after any synthesis the nanoclusters have to be separated from unreacted ligands or by-products through techniques such as precipitation, centrifugation, or filtration. Moreover, achieving 100% homogeneity from any AuNCs synthesis method is impossible, thus, after the synthesis and purification of nanoclusters, different nanocluster species are isolated from each other using chromatography or dialysis.

IV. 2 Optical properties of gold nanoclusters

The origin of the optical properties of gold nanoclusters was a highly discussable matter until the synthesis and crystallographic analysis of the atomically precise gold nanoclusters - $[\text{Au}_{102}(\text{p-MBA})_{44}]^{130}$, where *p*-MBA is *p*-mercaptobenzoic acid, and $[\text{Au}_{25}(\text{SCH}_2\text{CH}_2\text{Ph})_{18}]^{131}$. Correlating them with DFT (density functional theory) calculations led to an understanding of their electronic and optical properties. For example, it was understood that the HOMO band, and the lowest three LUMO bands, in the electronic structure of Au_{25} nanoclusters, are mainly composed of 6s (or 6sp) atomic orbitals and that both types of orbitals have a slightly S(3p) character, indicating ligand influence.¹²² Furthermore, understanding the electronic structure of this nanocluster allowed scientists to determine which electronic transitions are associated with each of the bands observed in its absorption spectra. While the crystallization of gold nanoclusters across a wide range of sizes remains challenging, some studies have established correlations between their optical properties and factors such as their size¹³² or surface functionalization¹³³. Jin *et al* compared the optical properties of thiolate-protected gold nanoclusters with sizes from Au_{15} to Au_{144} and have reported that increasing the number of gold atoms building the nanocluster (and, as a result, their size) results in a shrinking electronic band gap. Moreover, he discovered that the geometry of the nanocluster kernel also plays a vital role – structures with FCC geometry have much higher band gap energies than the icosahedral ones of comparable sizes. The recent work by Zhou *et al* allowed to further characterize the correlation between the nanoclusters structure, size and their optical properties.¹³⁴ They found out, that based on the optical properties, such as the radiative and nonradiative recombination rates, gold nanoclusters could be divided into three distinct groups (Figure 6). AuNCs smaller than 50 gold atoms present optical properties are more dependent on their structure than size. AuNCs with sizes between 50 and 100 gold atoms with both size- and structure-dependent optical properties and large-sized gold NCs (>100 Au atoms) with optical properties depending only on size.

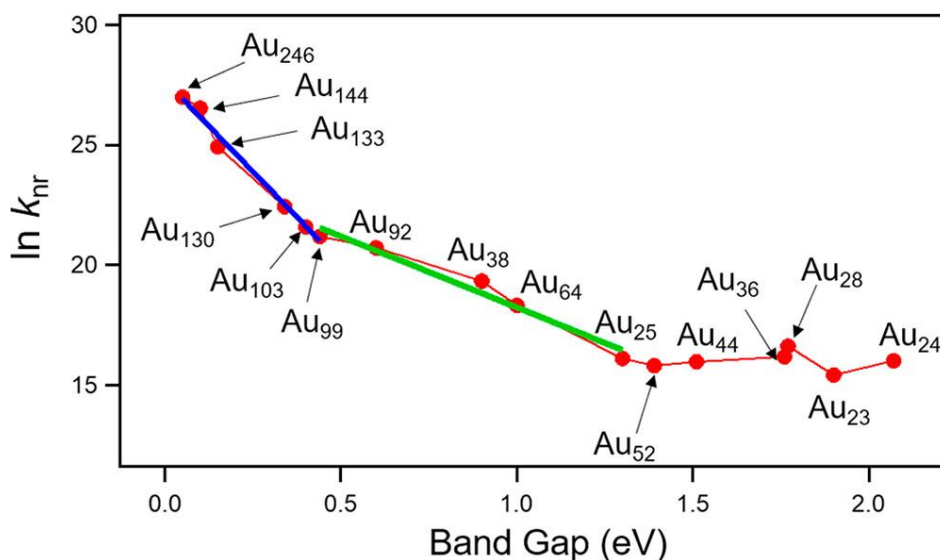


Figure 6. Plot of nonradiative recombination rate k_{nr} of versus the band gap energy for gold nanoclusters of different sizes. Reprinted from reference no. ¹³⁴ (<https://doi.org/10.1021/jacs.9b09066>), copyright © 2019 American Chemical Society.

Another of the molecule-like properties of gold nanoclusters, besides the discrete absorption spectra, is their ability to emit photoluminescence.¹³⁵ The photoluminescence of the first synthesized gold nanoclusters was often located in the red or infrared range of the light spectrum and characterized by relatively low (<20%) quantum yields.¹³⁶ However, over the last decade, a lot of research has focused on enhancing this property because of the other beneficial features of nanoclusters that distinguish them from other luminescent materials like organic dyes or semiconductor quantum dots - AuNCs exhibit superior biocompatibility, photostability and reduced toxicity.^{137, 138} Based on research on that topic, it can be concluded that the luminescent properties of gold nanoclusters could be tailored by ligand engineering (Figure 7a), kernel modification (Figure 7b), aggregation (Figure 7c) or assembly (Figure 7d).¹³⁵ Photoluminescence of many AuNCs is based on ligand-to-metal charge transfer and, thus, controlling the electron-donating capability by ligand modifications is an easy way to tune it. A good example of this mechanism was reported by Wu *et al* – they discovered that the intensity of photoluminescence emitted by Au₂₅(SR)₁₈ could be increased by increasing the charge-donating capability of ligands, from the lowest PL intensity reported for Au₂₅(SC₆H₁₃)₁₈ and the highest for Au₂₅(SC₂H₄Ph)₁₈.¹³⁹ Moreover, changing the ligand could also lead to transformation of the nanocluster kernel, changing the luminescence wavelength range. Pradeep *et al* reported that an additional shell of thiolate on the Au₂₅(SBB)₁₈ nanocluster surface not only changed the nanocluster core (to Au₂₉(SBB)₂₄S) but also shifted its luminescence maximum from 1030 nm to 737 nm and increased PL quantum yield from 0.04% to 1.8%.¹⁴⁰ Another way to enhance the photoluminescence of AuNCs is aggregation-induced emission (AIE) - a phenomenon where specific molecules emit weakly, or not at all, in a dispersed state but exhibit strong luminescence upon aggregation.¹⁴¹ For example, Luo *et al* discovered that non-luminescent gold nanoclusters made from Au(I)-thiolate complexes could emit strong luminescence after either a solvent-induced or cation-induced aggregation.¹⁴² Moreover, the intensity and emission maximum were tunable by changing the degree of aggregation. In the end, also the self-assembly of gold nanoclusters into hierarchical structures could enhance their

optical properties. Wu *et al* used the aurophilic ($Au^1 \cdots Au^1$) interaction to organize $Au_{25}(SR)_{18}$ nanoclusters into nanoribbons and discovered that it induced two independent emission bands.¹⁴³ The optical properties of gold nanoclusters could also be modified using template-driven assembly. Huang *et al* showed that aminosilane-grafted AuNCs prepared on a silica template exhibited red-shifted PL emission and 66% quantum yields.¹⁴⁴ Interestingly, high fluorescence quantum yield resulted from the order of magnitude increase in radiative decay rate k_r due to electronic coupling between the closely-assembled gold nanoclusters.

Moreover, gold nanoclusters, as one of the few types of nanomaterials, exhibit fascinating nonlinear optical (NLO) properties.¹⁴⁵ Nonlinear optics refers to the study of light-matter interactions where the response of a material depends nonlinearly on the electric field of light. Unlike linear optics, where properties like refractive index remain constant, NLO phenomena involve effects like light intensity-dependent refractive index and change of wavelength of light travelling in NLO material. These effects result from the material's polarization response, which, at a sufficiently high electric field, depends on the higher-order material's susceptibilities. However, since the probability of such effects is extremely low, they require high photon flux, typically achievable with femtosecond lasers. Gold nanoclusters were reported to exhibit both second-order non-linear optical effects, like second-harmonic generation (SHG), and third-order non-linear optical effects, like two-photon absorption (TPA) or third-harmonic generation (THG). Knoppe *et al* showed that both $Au_{25}(\text{capt})_{18}^-$ (where capt is captopril) and $Au_{38}(\text{SCH}_2\text{CH}_2\text{Ph})_{24}$ nanoclusters can exhibit SHG upon excitation at 800 nm, and proved that it is connected to their non-centrosymmetric geometry.¹⁴⁶ Moreover, at 1200 nm excitation wavelength, $Au_{38}(\text{SCH}_2\text{CH}_2\text{Ph})_{24}$ also exhibited THG. Concerning the exquisite two-photon absorption of AuNCs - in 2008, Ramakrishna *et al.* reported a record-high TPA cross-section values for hexane thiolate capped Au_{25} gold nanoclusters, reaching 427 000 GM (Goeppert Mayer, $1 \text{ GM} = 10^{-50} \text{ cm}^4 \text{ s photon}^{-1}$) at 800 nm, which was two orders of magnitude higher than standard organic dyes, showing their great potential for application in multiphoton imaging.¹⁴⁷ Additionally, Obstarczyk *et al.* showed that the non-linear properties of $Au_{25}(\text{PET})_{18}$ gold nanoclusters could be further enhanced by linking them into dimers or trimers using (1*R*,1'*R*)-6,6'-(1,4-phenylene)di-1,1'-binaphthyl-2,2'-dithiol.¹⁴⁸ The starting TPA cross-section 9 000 GM for monomers rised to 50 000 GM and 66 000 GM for dimers and trimers, respectively. In the end, gold nanocluster could also efficiently emit two-photon excited fluorescence. Oh *et al.* excited the water-soluble bidentate-poly(ethylene glycol) capped gold nanoclusters and observed that upon two-photon excitation at wavelengths ranging from 860 nm to 1400 nm, nanoclusters show a broad fluorescence band, with maximum located in the same range as during one-photon excitation at 450 nm.¹⁴⁹

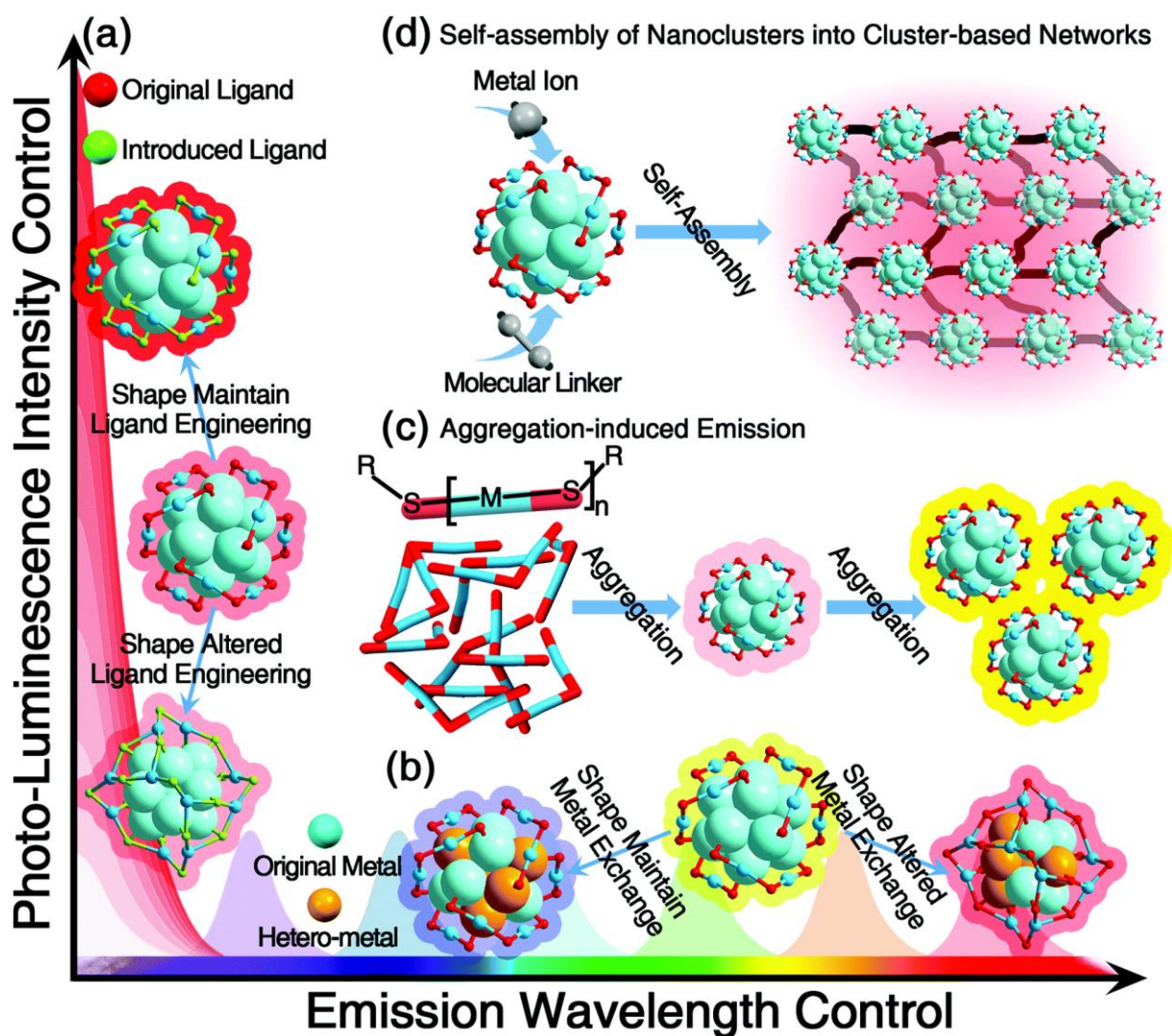


Figure 7. Scheme presenting the PL-tailoring strategies for gold nanoclusters. (a) ligand engineering, (b) kernel modification, (c) aggregation-induced emission, (d) AuNCs self-assembly. Used with permission of Royal Society of Chemistry from reference no.¹³⁵ (<http://dx.doi.org/10.1039/C8CS00800K>) © 2025; permission conveyed through Copyright Clearance Center, Inc.

IV. 3 Chirality of gold nanoclusters

In addition to the AuNCs features described earlier, gold nanoclusters can also gain a plethora of new physical and chemical properties through chirality, including new chiroptical properties like circular dichroism or circularly polarized luminescence. The chirality of gold nanoclusters can emerge from three sources. The first one is intrinsic chirality, which could arise from the chiral geometry of the nanocluster kernel,¹⁵⁰ chiral arrangement of surrounding staple motives,¹⁵¹ or chiral arrangements of carbon tails within the ligand structure.¹⁵² The second, and the most common, source of chirality points to chiral ligands stabilizing the surfaces of gold nanoclusters. Numerous studies have shown that intrinsically achiral gold nanoclusters can gain chirality due to functionalization with chiral ligands such as glutathione,¹⁵³ captopril,¹⁵⁴ or BINAP (2,2'-bis(diphenylphosphino)-1,1'-binaphthyl)¹⁵⁵. Finally, the last source of AuNCs chirality is hierarchical assembly. It could be realized via self-assembling methods¹⁵⁶ or template-driven assembly¹⁵⁷. These types of methods allow to

achieve strong chiroptical properties, often stronger than other chirality-induction methods, and offer versatility, inducing the chiral properties upon assembly of both previously chiral and achiral AuNCs. Moreover, assembly with the support of soft templates, such as biomolecules or liquid crystalline materials, provides advantages like adjustable periodicity of assembled particles, enabled by the weak and reversible interactions between template molecules and nanocluster ligands.¹⁵⁸ Broader incorporation of this type of AuNCs assembly could be used to solve one of the major problems with intrinsically chiral gold nanoclusters - their synthesis often produces a racemic solution.¹⁵⁹

The fundamental property of most chiral gold nanoclusters, which is also, under any circumstances, used to confirm their chiral character, is circular dichroism.¹⁶⁰ Due to their molecule-like properties, CD spectra usually consist of many bands of varying intensity extending over the entire absorption range. Their analysis allows deciphering information such as the contribution of individual ligands.¹⁶¹ Moreover, some of the luminescent gold nanoclusters emit strong circularly polarized luminescence. The luminescence dissymmetry factors of single gold nanoclusters or their aggregates are of the order of magnitude 10^{-3} .^{162, 163} Interestingly, the strongest CPL activity was reported for cellulose template-assembled gold nanoclusters films by Zhang *et al.* with g_{lum} of the magnitude 10^{-2} .⁶⁷ During the recent years, researchers' attention was also drawn to non-linear chiroptical properties of gold nanoclusters. Olesiak-Bańska *et al.* proved that chiral $Au_{25}[(capt)_{18}]^{-}$ gold nanoclusters exhibit two-photon circular dichroism.¹⁶⁴ Pniakowska *et al.* reported that gold nanoclusters stabilized with 6-aza-2-thiothymine and coated with chiral L- and D-arginine ligands could also exhibit two-photon excited fluorescence detected circular dichroism.¹⁶⁵ Moreover, two-photon circular dichroism was two orders of magnitude stronger than standard one-photon excited CD. In addition, Obstarczyk *et al.* showed that enantiomers of $Au_{38}(PET)_{24}$ nanoclusters could exhibit both two- and three-photon circular dichroism, which was 178 and 217 times stronger than the one-photon CD of studied nanoclusters.¹⁶⁶

In conclusion, gold nanoclusters are promising chiral nanomaterials with a plethora of ways to induce chiral optical properties. Their broad CD range and strong circularly polarized luminescence make them a perfect candidate for a next-generation optical marker, which, due to their biocompatibility, could be more useful than standard organic dyes currently used.

IV. 4 Applications of gold nanoclusters

Gold nanoclusters with their ultrasmall size, unique quantum-confined properties, and high biocompatibility find applications across various domains.

Gold nanoclusters exhibit bright fluorescence with a tunable emission spectrum, making them excellent candidates for multimodal bioimaging. Casteleiro *et al.* showed that AuNCs stabilized with PNAM (poly(*N*-acryloyl morpholine)) could be used for bioimaging of HeLa cells under both one- and two-photon excitation.¹⁶⁷ Moreover, Jiang *et al.* discovered that gold nanoclusters capped with a zwitterionic ligand and 11-mercaptopundecanoic acid and functionalized with biomarkers like biotin and streptavidin could be used in multimodal imaging of breast cancer cells.¹⁶⁸ On the other hand, Obstarczyk *et al.* used another feature of nanoclusters in tissue imaging. They reported that crown-ether capped gold nanoclusters could

be applied in TEM imaging of biological structures like amyloid fibrils due to their high electron density and high affinity to biomolecules.¹⁶⁹

AuNCs properties could also be used to cure, for example by photodynamic therapy. It was reported that AuNCs nanocomposites made from glutathione-capped AuNCs, hyaluronic acid and protamine proteins can generate highly reactive singlet oxygen species.¹⁷⁰ Moreover, described nanocomposites targeted MDA-MB-231 cancer cells and, after irradiation with white light, caused the death of 83% of targeted cells. Zhu *et al* used multifunctional composites made of antimicrobial peptide (AMP)-protected AuNCs conjugated with appropriate polymers could kill not only cancer cells but also *E. coli* bacteria.¹⁷¹

Apart from biomedical applications, gold nanoclusters could also be used in fields like energy harvesting or catalysis. Zhang *et al* reported that incorporating water-soluble gold nanoclusters inside non-photosynthetic *M. thermoacetica* bacteria allowed efficient photosynthesis of acetic acid from CO₂.¹⁷² Gold nanoclusters exhibit remarkable catalytic properties for reactions such as oxidation and reduction, largely due to their quantum-sized effects and active surface atoms. Because of that, they were used to construct continuous-flow microreactors for catalysis.¹⁷³ Combining gold nanoclusters with graphene layers allowed the continuous flow-reduction of 4-nitrophenol into 4-aminophenol and AuNCs served as catalytically active sites.

As can be seen, gold nanoclusters exhibit extraordinary versatility across applications such as catalysis, bioimaging, biosensing, and energy conversion. Their continued development and functionalization hold significant promise for advancing fields ranging from renewable energy to personalized medicine, as evidenced by their success in numerous cutting-edge scientific studies.

V. Chiral heterostructures with gold nanoparticles

The analysis of the previous chapters devoted to the broad field of chiral nanomaterials and, specifically, gold nanoparticles leads to the conclusion that these are extremely multifunctional materials with unique optical properties and numerous applications in fields from medicine to photocatalysis. Chiral heterostructures with AuNPs are designed by integrating gold nanoparticles with chiral organic molecules, biomolecules, or chiral templates. This integration often enhances intrinsic properties of gold nanoparticles and nanoclusters, as well as, enables the generation of pronounced chiroptical effects, such as circular dichroism and circularly polarized luminescence, which are crucial for advanced sensing and imaging technologies. Furthermore, the structural tunability of AuNP- or AuNC-based heterostructures allows for precise control over their optical and electronic properties, making them versatile platforms for studying light-matter interactions at the nanoscale. Despite these promising applications, challenges remain in achieving scalable and reproducible synthesis, understanding the mechanisms behind their chiroptical responses, and optimizing their performance for practical use. Research into chiral heterostructures with AuNPs is therefore at the intersection of materials science, chemistry, and nanophotonics, offering transformative potential across scientific and industrial domains.

This chapter will be a review of the most important and recent information on chiral heterostructures with gold plasmonic nanoparticles and gold nanoclusters. It will focus on three types of chiral heterostructures that were explored experimentally during the dissertation: template-directed chiral heterostructures with plasmonic gold nanoparticles, template-directed chiral heterostructures with gold nanoclusters and chiral biomolecule-protected gold nanoclusters. It will discuss their fabrication methods and the unique optical properties obtained in this way. It also aims to identify some of the issues of chiral heterostructures and questions that still need to be answered.

V. 1 Template-directed chiral heterostructures with plasmonic gold nanoparticles

One of the most studied types of chiral heterostructures are those created from plasmonic gold nanoparticles bound to various biomolecules. As mentioned in the previous chapters, such conjunction strongly increases their biocompatibility with biological tissues and cells, allowing their application in medical fields. Moreover, the chiral template-driven assembly of AuNPs can induce chiroptical activity in achiral AuNPs, which can be used to detect the chosen biomolecules.

A great example showing how significant research on chiral heterostructures can be for the development of medicine is the report on heterostructures with amyloids and other protein aggregates associated with neurodegenerative diseases. In 2018, Kumar *et al.* reported that α -synuclein amyloid fibrils could helically arrange gold nanorods, inducing circular dichroism response in their plasmonic (~ 800 nm) wavelength range (Figure 8a).⁴⁶ Moreover, they discovered that this method could also be extended to detect fibrils incubated from prion proteins (PrP), responsible for Creutzfeldt–Jakob disease. However, what is most important from the application perspective, this technique was not only successfully applied to detect the pathological changes *in vitro*, but also the ones grown *in vivo*, as confirmed by enhanced CD signal observed from human brain homogenates of patients affected by Parkinson’s disease. The origin of observed chiroptical activity was explained as the result of dipole-coupling between the neighboring helically arranged gold nanoparticles. This was backed up by the theoretical calculations of optical properties of double helical-arranged gold nanoparticles. In addition, scientists determined a few factors controlling the chiroptical response. First of all, the induced CD response increased with the amyloid incubation time, stabilizing only after the mature amyloid fibrils were formed. Secondly, the CD intensity was highly dependent on the AuNRs concentration, increasing after the addition of more nanoparticles. Thirdly, the helical end-to-end arrangement of AuNRs led to strong (>50 nm) red-shift of both extinction and CD bands. Thus, the induced plasmonic chiroptical activity not only allows the detection of the amyloid fibrils, but also monitors their formation over time. Another advantage of the discussed chiral heterostructures was the simplicity of their preparation. They were created by mixing gold nanorods, synthesized using the seedless growth method,⁸⁵ with already fibrillated proteins. The gold nanorods were dispersed in a buffer solution made of 1 mL water, 150 mM NaCl and 25 mM Tris-HCl pH 8 buffer, and then, various concentrations up to 80 nM of α -synuclein amyloid fibrils were added and monitored using CD spectroscopy. The importance of Kumar’s discovery encouraged other scientists to turn their attention to chiral amyloid-AuNPs heterostructures. Longhena *et al.* expanded the applicability of the mechanism suggested by Kumar even further, presenting a chiral plasmonic response from the interaction of AuNRs with two different forms of α Syn fibrils incubated both *in vitro* and *in vivo*, using the mouse brain tissues.¹⁷⁴ Lu *et al.* discovered that chiral heterostructures assembled from AuNRs coated with hIAPP (human islet amyloid polypeptides) and hIAPP fibrils result in record-breaking g -factors, higher than reported for α -synuclein.⁷¹ The intensity of the CD peaks increased from 0.90 mdeg (assembly without hIAPP coating) to 2000 mdeg, enabling highly precise sensing to track the kinetics of amyloid peptide association, even at relatively low peptide concentrations. To sum up, the research on amyloid-AuNRs chiral heterostructure not only results in a set of new tools to detect and monitor the behavior of various proteins and their

aggregates incubated both *in vitro* and *in vivo* but also leads to the creation of chiral nanomaterials with record-breaking chiroptical properties.

In addition to proteins, a large part of research on this topic is also devoted to chiral heterostructures combining plasmonic gold nanoparticles with DNA. They can be divided into three categories: pyramidal DNA-linked nanoparticles, DNA-directed helices and DNA-linked dimers.⁵⁰ The development of pyramidal heterostructures became possible after Goodman *et al.* reported a paper about the self-assembly of DNA tetrahedrons.¹⁷⁵ The first reports focused on constructing the asymmetric plasmonic configurations by binding plasmonic AuNPs to tetrahedron tips.¹⁷⁶ However, no chiroptical properties were observed. The next step was a study by Yan *et al.* describing asymmetric pyramidal nanostructures made with different materials and their chiroptical properties.⁹ They discovered that pyramidal heterostructures with three different types of NPs (Au, Ag and CdSe/ZnS quantum dots) exhibit chiroptical activity (circular dichroism in the visible range) with anisotropy g -factors $\sim 1.9 \times 10^{-2}$. However, bi-pyramidal DNA heterostructures created with only gold plasmonic nanoparticles exhibited a much weaker CD response.¹⁷⁷ The second and most studied type of DNA-AuNP heterostructures are DNA-directed helices. In 2012, Kuzyk *et al.* reported using DNA origami templates to arrange spherical AuNPs into nanohelices (Figure 8b).⁴⁵ What is more important, the reported helices possessed tailorable chiroptical properties with switchable handedness, as well as the tunable intensity and wavelength range of chiroptical response. The creation of this kind of heterostructure was possible due to the functionalization of both the surface of nanoparticles and the appropriate DNA template fragments binding them. AuNPs were functionalized with thiol-modified DNA strands which were complementary to the template attachment sites, consisting of three 15-nucleotide-long single-stranded oligonucleotides. Concerning their tunable chiroptical properties, the handedness of the CD signal was connected to the handedness of DNA-AuNP helices, switchable after the modification of the attachment site's location. Changing the diameter of nanoparticles from 10 nm to 16 nm, enhanced the CD signal intensity 400 times. In the end, changing the nanoparticles metal composition by spraying silver on their surface, blue-shifted the bands visible in CD spectra compared to pure Au composition. The last but not least type of DNA-AuNP heterostructures are chiral dimers created using DNA as linkers. As previously written, anisotropic gold nanoparticles could gain chirality due to the chiral mutual arrangement of nanoparticles, even in assemblies as small as dimers or trimers. For example, Ma *et al.* reported the creation of tilted nanorod dimers connected with DNA, showing a CD activity in the plasmonic range.⁸ The nanorods' sides were modified with two complementary nucleic acids, enabling them to form a tilted chiral dimeric structure through dimerization during a polymerase chain reaction (PCR) process.

Chiral template-assisted assembly of plasmonic gold nanoparticles may also use silica nanohelices. Gao *et al.* reported the creation of “*Goldhelices*” exhibiting chiroptical properties and created from silica nanohelices and plasmonic gold nanoparticles.⁴⁴ In order to create them, the AuNPs ligands with carboxylic groups were linked via the covalent bond with the amine-modified silica surfaces. The resulting dispersions of gold helices exhibited a strong CD signal in the visible range, with signs depending on the controllable twist of silica helices (Figure 8c). Moreover, the researchers proved that observed chiroptical properties could be further tuned by

the hierarchical organization of *Goldhelices* into multi-layered structures - changing the layer-to-layer spacer thickness allowed to switch off the chiroptical properties while keeping the linear dichroism at the same order of magnitude.

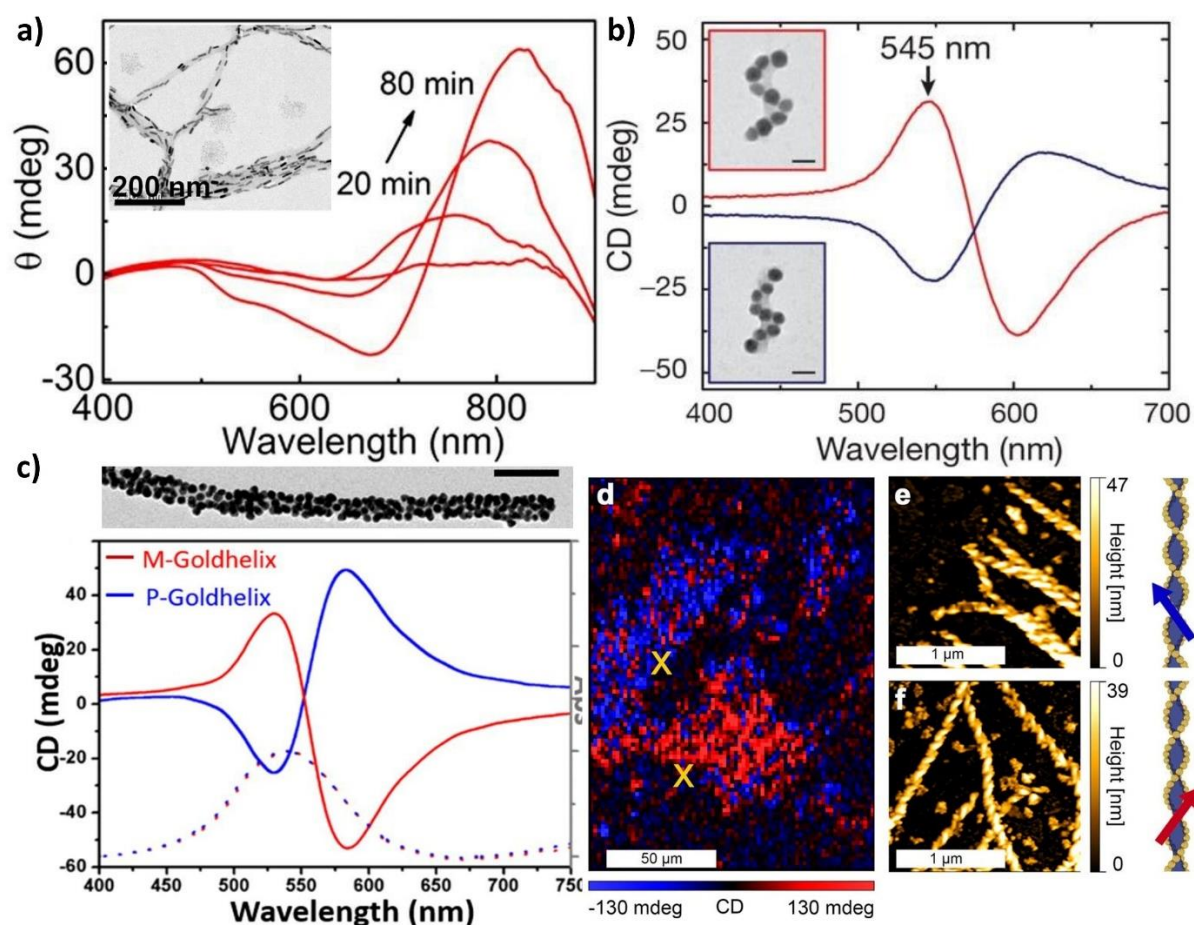


Figure 8. Optical properties of template-directed chiral heterostructures with plasmonic gold nanoparticles. (a) Circular dichroism spectrum and TEM images of helical assemblies of gold nanorods coating alfa-synuclein amyloid fibrils. Reprinted from reference no.⁴⁶ Copyright © 2018 National Academy of Sciences. (b) CD spectrum and TEM images of DNA origami templated gold nanospheres assembled into helices. Reproduced from reference no.⁴⁵ (<https://doi.org/10.1038/nature10889>) with permission from Springer Nature. (c) TEM image and CD spectrum of one of the *Goldhelices* assembled using silica nanohelices and AuNPs. Reprinted with permission from reference no.⁴⁴ (<https://doi.org/10.1021/acs.nano.9b08823>) Copyright © 2020 American Chemical Society. (d) CD map of chiral domains of helical nanofilaments coated by gold nanospheres. AFM images of left-handed (e) and right-handed (f) helical nanofilaments building the chiral domains. Images (d – f) are reprinted from reference no.¹⁷⁸ under Creative Commons Attribution 4.0 (CC BY 4.0) license.

Last but not least are chiral heterostructures assembled with organic soft materials, such as liquid crystals. As mentioned in chapter II. 4, liquid-crystalline helical nanofilament (HNF) phases can be used to assemble nanoparticle-coated helices.³⁵ To create them, the surface of the 3.9 nm spherical AuNP was functionalized with a mixed dodecanethiol/L ligand coating (where L is a promesogenic compound derived from the studied liquid crystalline template), ensuring the optimal interactions between the nanoparticles and the helical template. Then, the nanoparticles were mixed with the template solution and subjected to the heating/cooling cycle, required to form the nanofilament phase. The helical edges of the resulting heterostructures

were coated with AuNPs, as confirmed by TEM imaging. What is more important, the same study has shown that this template-driven assembly method could be applied not only to spherical gold nanoparticles of other diameters (1.9 nm) but also to gold nanorods, showing its universality and broad applicability. Advancing further studies on such types of chiral heterostructures, Szustakiewicz *et al.* reported the chiroptical properties of HNF-AuNP assemblies.¹⁷⁸ Using the micro-CD technique, they discovered that such assemblies create homochiral domains with mirror-like plasmonic CD signals bearing both handedness (Figure 8d-f).

The examples discussed above highlight the potential of chiral heterostructures of plasmonic gold nanoparticles as versatile chiral nanomaterials with unique optical properties. Research on amyloid-AuNP heterostructures presented a new platform for biosensing pathologic changes in the human body. Peptide fibril templated heterostructures exhibited record-breaking chiroptical properties. Moreover, combining the AuNPs with DNA offered high tunability of both optical properties and morphology of assembled heterostructures. Research on silica-templated heterostructures showed that the hierarchical organization of such structures can also tune their chiroptical activity. In the end, liquid crystalline helical nanofilaments turned out to be a universal matrix that allows for the arrangement of plasmonic nanoparticles of various shapes and sizes. Overall, current advancements in understanding the collective chiroptical activity of colloidal plasmonic systems provide a rich resource of templates and methodologies. Continued efforts aim to enhance structure–optical activity relationships, maximizing their chiroptical performance. Thus, chiral heterostructures with plasmonic gold nanoparticles are addressing the demands of advanced chiral photonic system applications.

V. 2 Template-directed chiral heterostructures with gold nanoclusters

In the case of gold nanoclusters, in contrast to the multiple reported ways of inducing chirality via chiral ligands or self-assembly, the topic of optical properties exhibited by chiral heterostructures constructed via templates remains largely unexplored. There are only few papers about the optical properties of chiral template-directed assemblies of gold nanoclusters.^{67, 157}

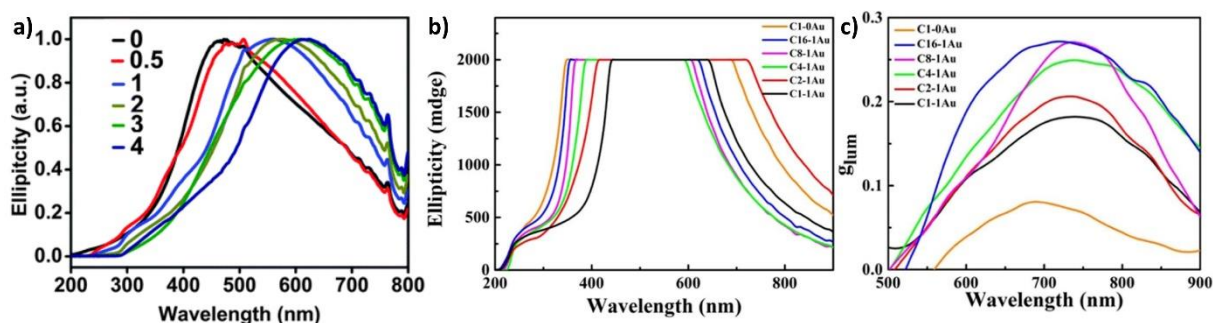


Figure 9. Optical properties of template-directed chiral heterostructures with gold nanoclusters. (a) Circular dichroism spectra of BSA-AuNC-CNC films tuned by BSA-AuNC load modification. Numbers from 0 to 4 describe the mL volume of AuNC in the mixture. Used with permission of Royal Society of Chemistry from reference no.¹⁵⁷ (<http://dx.doi.org/10.1039/C5TC04163E>); permission conveyed through Copyright Clearance Center, Inc. CD (b) and CPL (c) spectra of composite film with different ratios of CNCs (from 1 to 16) and BSA-AuNCs (0 or 1). Images (b – c) are reprinted with permission from reference no.⁶⁷ (<https://doi.org/10.1021/acs.langmuir.2c00376>). Copyright © 2022 American Chemical Society.

In 2016, Qu *et al.* published a paper about the chiral AuNC films assembled using photonic cellulose nanocrystals (CNC).¹⁵⁷ The study used the Au₂₅ gold nanoclusters stabilized with bovine serum albumin (BSA), because of their negatively charged surface at neutral pH. It was important since AuNC and CNC could self-organize, forming host-guest films *via* repulsive interactions. After the synthesis, the appropriate amount of AuNCs was mixed with a water solution of cellulose nanocrystals until homogeneity, and then, the suspension underwent evaporation-induced self-assembly for 2 days at room temperature to obtain chiral nematic AuNC-CNC films. The resulting films possessed tunable optical and chiroptical properties. It was shown that by tuning the AuNC load in the AuNC-CNC mixture, one could tune both the location of optical absorption and CD band maximum (Figure 9a). It was explained by the changing helical pitch of periodically arranged AuNCs inside the CNC template. Moreover, the fluorescence intensity and maximum wavelength were also tunable – an increased load of AuNCs led to increased fluorescence intensity and maximum redshift. In the end, they discovered that one of the composite films, AuNC₁-CNC, exhibits chiroptical-dependent fluorescence emission. A few years later, Zhang *et al.* further explored the optical properties of CNC-based AuNC assemblies and reported that apart from CD, they could exhibit strong circularly polarized luminescence.⁶⁷ The composite films were prepared in a similar manner to the previously discussed case, mixing various amounts of BSA-AuNC with CNC aqueous solution, followed by evaporation-induced self-assembly. However, both the reported CD spectra of CNC and AuNCs-CNC films exhibited strong positive CD signals, red-shifting with increasing AuNC concentration and with an intensity exceeding 2000 mdeg (Figure 9b).

The composite films were also studied using a CPL spectrometer. All studied films, also without gold nanoclusters, exhibited strong left-handed CPL and increasing the concentration of AuNC increased the CPL wavelength from 675 nm to 706 nm. What is more, modification of the AuNC concentration also led to changes in the g_{lum} values – from 0.07 for CNC films without AuNC to 0.27 for AuNC-CNC composite with CNC/AuNC ratio 16:1 (Figure 9c). This study has proved, that CNCs-assisted gold nanoclusters assemblies lead to strong chiroptical properties and creation of a new type of CPL active materials.

V. 3 Chiral biomolecule-protected gold nanoclusters

Many studies on gold nanoclusters, because of their optical properties and strong luminescence tunable from VIS to NIR range, focus on their application in biomedical fields. One of the most common ways to enhance their biocompatibility is functionalization with intrinsically chiral biomolecules like amino acids, peptides, and proteins. Such assembly results in another type of chiral heterostructures, often exhibiting chiroptical properties.

In the case of gold nanoclusters coated with amino acids, chiral optical properties were reported for heterostructures with histidine (His),¹⁷⁹ cysteine (Cys),¹⁸⁰ and arginine (Arg)¹⁶⁵. The synthesis of optically active His-AuNCs was reported by Guo *et al.*¹⁷⁹ Interestingly, the presented synthesis was a one-step, one-pot process, starting with mixing the aqueous solutions of HAuCl₄ and His (both racemic and enantiomeric forms) followed by two-hour incubation in room temperature. The resulting gold nanoclusters were characterized by absorption maximum located at 260 nm and a green fluorescence (QY≈8.96%) with an emission maximum located at 498 nm. CD spectroscopy has revealed that His-enantiomer-coated AuNCs (L-His and D-His) exhibited mirror-like CD spectra, with new peaks located at 298 nm, since free His have CD peaks at 214 nm. Moreover, they explored how changing the mutual molar ratio between His and HAuCl₄ during the synthesis influences the chiroptical properties of resulting AuNCs and found that increasing the concentration of amino acids, from molar ratio 10 to 45, increases the ellipticity of CD maximum band from <1 mdeg to >10 mdeg. This CD response was further modified by the addition of another layer of chiral ligand - penicillamine, to pre-existing His-AuNCs. Each enantiomer was functionalized with the penicillamine ligands of the opposite handedness (L-His-AuNCs with D-Pen and D-His-AuNCs with L-Pen). Such a procedure not only enhanced the CD intensity of both enantiomers to above 90 mdeg but also reversed its handedness. It was concluded, that observed chiroptical properties could originate from both the intrinsically chiral metal core of AuNCs and the dissymmetrical field model, responsible for effects observed in Pen-His-coated AuNCs. Another example of chiral amino-acid coated AuNCs are Cys-AuNCs.¹⁸⁰ Hao *et al.* reported that this type of gold nanocluster not only possesses a high binding affinity to plasma coagulation factor, but also exhibits chiroptical activity. Cys-AuNCs synthesis was based on the modified Brust method.¹⁸¹ First the aqueous cysteine solution was mixed with HAuCl₄, and pH was adjusted with NaOH. Then addition of NaBH₄ resulted in reduction reaction and the solution was stirred for 36 hours, before followed by purification with methanol. Two resulting enantiomers of L-Cys and D-Cys coated gold nanoclusters were characterized by mirror-like broad CD spectra with multiple peaks ranging from 200 nm to 650 nm. In 2023, Pniakowska *et al.* reported that amino acid-protected gold nanoclusters could also possess strong non-linear chiroptical activity.¹⁶⁵ The chiral gold

nanoclusters were functionalized with two types of ligands – stabilizing ligand 6-aza-2-thiopyrimidine (ATT) and chiral ligands L- and D-arginine. Chiral nanoclusters were synthesized in two steps. First, the one-pot synthesis of ATT-AuNCs, where an aqueous solution of ATT (pH 10) was mixed with HAuCl₄, stirred for 1 hour at room temperature and purified by ultrafiltration using Millipore filters. Then, an appropriate amount of L-Arg and D-Arg solutions (pH 10) were added to ATT-AuNCs and incubated for 24 hours at 37° in order to create both enantiomers. The absorption spectra of Arg/ATT-AuNCs were characterized with three bands, located at 405 nm, 466 nm and 505 nm. Both enantiomers emitted strong green fluorescence with a maximum located at 528 nm and high quantum yields equal to 63.2% and 58.4% for L-Arg/ATT-AuNCs and D-Arg/ATT-AuNCs, respectively. CD spectrometry revealed that both enantiomers are characterized by mirror-like CD spectra, consisting of three bands located at 350 nm, 415 nm and 470 nm. Additionally, scientists measured the two-photon circular dichroism (TPCD) of both enantiomers using the fluorescence-detected circular dichroism method. In both cases, the shape and sign of TPCD spectra agreed well with their one-photon counterparts (Figure 10a). However, comparing the one-photon and two-photon anisotropy factors g_{abs} showed that the two-photon signal, at its maximum located at 825 nm, was ~245 times stronger than one-photon signal. Most importantly, these studies have shown that biomolecule-protected gold nanoclusters are characterized by strong nonlinear chiroptical properties, worth investigating further.

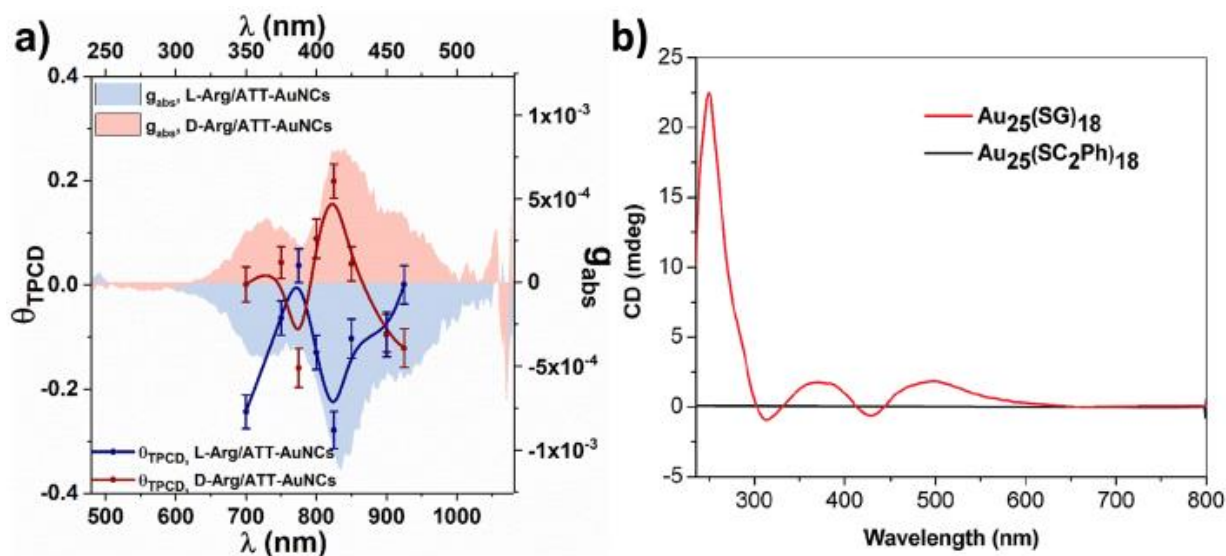


Figure 10. Optical properties of chiral biomolecule-protected gold nanoclusters. (a) One-photon dissymmetry factor (red/blue areas) and two-photon circular dichroism spectra (red/blue markers) of L-Arg and D-Arg functionalized ATT-AuNCs. Reprinted from reference no.¹⁶⁵ under a Creative Commons Attribution-NonCommercial 3.0 Unported (CC BY-NC) Licence. CD spectra of Au₂₅ gold nanoclusters coated with glutathione (SG) and phenylethylthiolate (SC₂Ph). Reprinted with permission from reference no.¹⁸² (<https://doi.org/10.1021/ja900386s>). Copyright © 2009 American Chemical Society.

Apart from amino-acids, chiral heterostructures with gold nanoclusters could also be functionalized with peptides¹⁸³ and proteins¹⁸⁴. The best known of all peptide-capped gold nanoclusters are those functionalized with glutathione (GS). The first reports come from 2000, when¹⁸⁵ Schaaf *et al.* reported that GSH-AuNCs are characterized with strong optical activity with multiple new CD bands, not reported for free GSH, in range from 5.5 eV to 1.5 eV (~225 nm to 825 nm). A few years later, Wu *et al.* synthesized and explored the structure of atomically precise Au₂₅(GS)₁₈ as well as their chiroptical properties.¹⁸² The CD spectrum of Au₂₅(GS)₁₈ was also characterized with multiple, relatively weak (~2 mdeg), bands in range from 300 nm to 600 nm. Moreover, they confirmed that in this case, chiroptical properties do not come from the chiral core, since Au₂₅(SCH₂CH₂Ph)₁₈ showed no optical activity, but are induced by GS ligands (Figure 10b). Additionally, Monti *et al.* explored theoretically what factors influence the chiroptical properties of glutathione-capped [Au₂₅(GS)₁₈]⁻¹ gold nanoclusters.¹⁸³ They discovered, that the UV range of studied CD spectrum strongly depends on the solvent, affecting both the geometry and the electronic structure of the nanocluster. In the case of protein-coated gold nanoclusters, the ligand-induced changes are usually only visible in the UV range of CD spectra. As showed for BSA-coated gold nanoclusters, mixing BSA with gold nanoclusters highly influences the protein secondary structure, which could be deduced from the changes in 200-250 nm range of CD spectra, but does not induce any new bands.¹⁸⁴

To sum up, various chiral biomolecules could be used to tailor the optical properties of gold nanoclusters, leading to chiral heterostructures with unique chiroptical properties. However, so far, only amino acids allow controllable tunability of their optical activity and strong chiral nonlinear effects.

V. 4 Selected questions regarding the chiral heterostructures with gold nanoparticles

As was presented in this chapter, chiral heterostructures with gold nanoparticles offer a new, and still not well understood, way to induce unique chiral optical properties at the nanoscale. In the case of both plasmonic nanoparticles and gold nanoclusters, applying chiral templates eliminates the requirement of chiral nanoparticle geometry or chiral ligands. Moreover, it often allows tunability of the induced chiral properties. On the other hand, coating the gold nanoclusters with biomolecules not only increases their biocompatibility but also induces strong linear and non-linear chiroptical properties. However, since this is a relatively new research direction, many questions still remain unanswered.

1. Chiral heterostructures with plasmonic gold nanoparticles:

- ❖ Kumar *et al.* showed that amyloid fibrils could be used to helically assemble gold nanorods, inducing strong CD response at the plasmonic range. It was proposed that the reported effect could be used to detect amyloid structures.⁴⁶ However, **do achiral plasmonic nanoparticles need to be helically assembled to exhibit induced chiroptical properties?** If the effect is observed also without their helical assembly but, for example, based on the coulombic interactions with chiral proteins or their aggregates, the nanoparticle-based amyloid-sensing method will be much more versatile.

- ❖ Govorov *et al.* presented that an achiral gold nanoparticle can start exhibiting chiroptical properties upon the dipole-coupling with the neighboring chiral molecule.⁵⁵ **Can the single nanoparticle also sense the aggregate of chiral molecules, such as protein fibrils?** Observing and understanding such an effect would allow for a breakthrough in biosensing and bioimaging of amyloids.

2. Chiral heterostructures with gold nanoclusters:

- ❖ Bagiński *et al.* discovered that co-assembly of plasmonic gold nanoparticles and helical nanofilaments could be used to helically arrange AuNPs in domains with both handedness.³⁵ One of the requirements was double-functionalization of AuNP surface with two ligands, ensuring the correct interaction with the template material. **Could the same type of surface-functionalization and gold-template interactions be used to helically assemble ultra-small gold nanoclusters?** Confirming that would create a new way to assemble various types and sizes of organic-soluble gold nanoclusters and, potentially, generate heterostructures with chiral optical properties.
- ❖ Zhang *et al.* reported the strong chiroptical properties, both CD and CPL, of CNC-based BSA-AuNC assemblies.⁶⁷ The left-handed CPL signal was observed from both CNC and CNC-AuNCs assemblies, and its intensity and wavelength changed with AuNCs concentration, indicating that interactions with nanoclusters enhance the chiral properties of the reported heterostructure. **Can template-directed assembly of AuNCs lead to CPL originating solely from the gold nanoclusters?**

3. Biomolecule-coated gold nanoclusters:

- ❖ Pniakowska *et al.* confirmed that Arginine-coated ATT gold nanoclusters possess both strong linear and nonlinear chiroptical properties.¹⁶⁵ Moreover, they presented that a two-photon CD response is two orders of magnitude stronger than a one-photon CD response, indicating that non-linear chiroptical properties are much stronger. **Could Arginine-coated ATT-AuNCs emit two-photon excited circularly polarized luminescence which is stronger than one-photon excited CPL?** Such discovery would be a motivation to intensify research on chiral nonlinear optical properties of gold nanoclusters and another proof, that gold nanoclusters are an excellent candidate for biological markers used in multiphoton imaging.

Experimental methods

VI. 1 One and Two-photon excited circularly polarized luminescence

As mentioned in the introductory part of this dissertation, many chiral nanomaterials exhibit chiral optical properties. During the research connected to this dissertation, I focused on two chiroptical properties of chiral heterostructures – circular dichroism and circularly polarized luminescence. The circular dichroism was measured using the commercially available equipment, Jasco J-1500 spectropolarimeter. However, part of the conducted research required determining the complementary information about the chiral properties of both the ground and excited state of the chiral heterostructure. Thus, to check if the observed chirality is also conserved in their luminescence properties I designed and built hand-made setups measuring both one-photon and two-photon excited circularly polarized luminescence.

The constructed setups were based on CPL type 0 measurement systems, where the left-handed and right-handed circularly polarized luminescence are obtained by properly rotating the quarter-wave plate to the main axis of the polarizer placed in front of the detector. Systems of this type are characterized by simplicity, relatively low price, and the ability to quickly verify whether a given material emits circularly polarized luminescence with a specific handedness. However, their main disadvantage is low sensitivity as compared to more complex and expensive setups. During my research, I developed two systems measuring circularly polarized luminescence resulting from both one-photon (Figure 11a) and two-photon (Figure 11b) excitation.

In the case of one-photon excited circularly polarized luminescence (Figure 11a, 1P-CPL) measuring system, samples were excited with a beam from 532 nm laser diode passing through a grey filter to control its power, measured, when needed, with a Thorlabs laser power meter. Then, the excitation beam went through a half-wave plate, used to control its polarization, and entered the microscope body. The CPL signal was collected in the form of two-dimensional XY scans using dry objective (Nikon LU Plan Fluo 100xA/0.90, epi-fluorescent mode) with 100x magnification and piezoelectric scanning stage (Piezojena TRITOR 102). Moreover, to minimize the possible artefacts from the laser, emission was collected after passing a 567 nm dichroic mirror (Thorlabs), reflecting the wavelengths below 567 nm and transmitting the wavelengths above 567 nm. The signal was then redirected with a silver mirror to a darkened box in which a quarter-wave plate (Thorlabs) and a polarizer (Thorlabs) were mounted in front of the detector - an avalanche photodiode (IDQ id100).

In the case of two-photon excited circularly polarized luminescence (Figure 11b, 2P-CPL), samples were excited with a laser beam from a Chameleon Ti:Sapphire laser (Coherent Inc.) with ~100 fs pulses and 80 MHz repetition rate. Then, the beam went through a grey filter to control its power (also measured using the Thorlabs power meter) and achromatic half-wave plate (Thorlabs), adjusted to the correct wavelength range. Samples were illuminated through a microscope objective (Nikon Plan Fluor, 40x, NA 0.75) working in the epi-fluorescence mode. Then, the collected signal was redirected to the 2P-CPL collection pathway, also built of a quarter-wave plate (Thorlabs) and a Glan-Thompson polarizer (Thorlabs). The 2P-CPL spectra were collected using the Shamrock 303i spectrometer (Andor) with an iDus camera (Andor).

The emission was also filtered with an 800 nm dichroic mirror (Thorlabs) to discard the scattered signal from the excitation beam.

Both systems are using the same mechanism for CPL collection. First, the circularly polarized signal is changed to linearly polarized one by the quarter-wave plate. Left-handed circularly polarized light results in a linearly polarized signal with an orientation -45° with respect to the QWP fast axis and right-handed circularly polarized light results in a linearly polarized signal with an orientation $+45^\circ$ with respect to the QWP fast axis. Then, the signal is filtered with a polarizer oriented -45° or $+45^\circ$ with respect to the QWP fast axis to collect left-handed (Figure 11c) or right-handed (Figure 11d) CPL. After collecting left-handed CPL and right-handed CPL, the one-photon (g_{1P-lum}) and two-photon (g_{2P-lum}) luminescence dissymmetry factors were calculated using the appropriate equations for 1P-CPL (eq. 14) and 2P-CPL (eq. 15):

$$g_{1P-lum} = 2 \cdot \frac{I_{LCPL} - I_{RCPL}}{I_{LCPL} + I_{RCPL}} \quad \text{Eq. 14}$$

$$g_{2P-lum} = 2 \cdot \frac{I_{2P LCPL} - I_{2P RCPL}}{I_{2P LCPL} + I_{2P RCPL}} \quad \text{Eq. 15}$$

The signal intensities collected by measuring left-handed and right-handed circularly polarized luminescence using one-photon CPL measuring system are labelled as I_{LCPL} and I_{RCPL} , respectively. The signal intensities collected by measuring left-handed and right-handed circularly polarized luminescence using two-photon CPL measuring system are labelled as $I_{2P LCPL}$ and $I_{2P RCPL}$, respectively. The luminescence dissymmetry factors are commonly used to compare the strength of the circularly polarized luminescence. If g_{lum} value is close to 2, it means that the majority of the signal emitted by the sample is circularly polarized luminescence of one-handedness. On the other hand, values close to 0 are connected with materials characterized by weak or no chiroptical properties, resulting in almost identical LCPL and RCPL signal intensity.

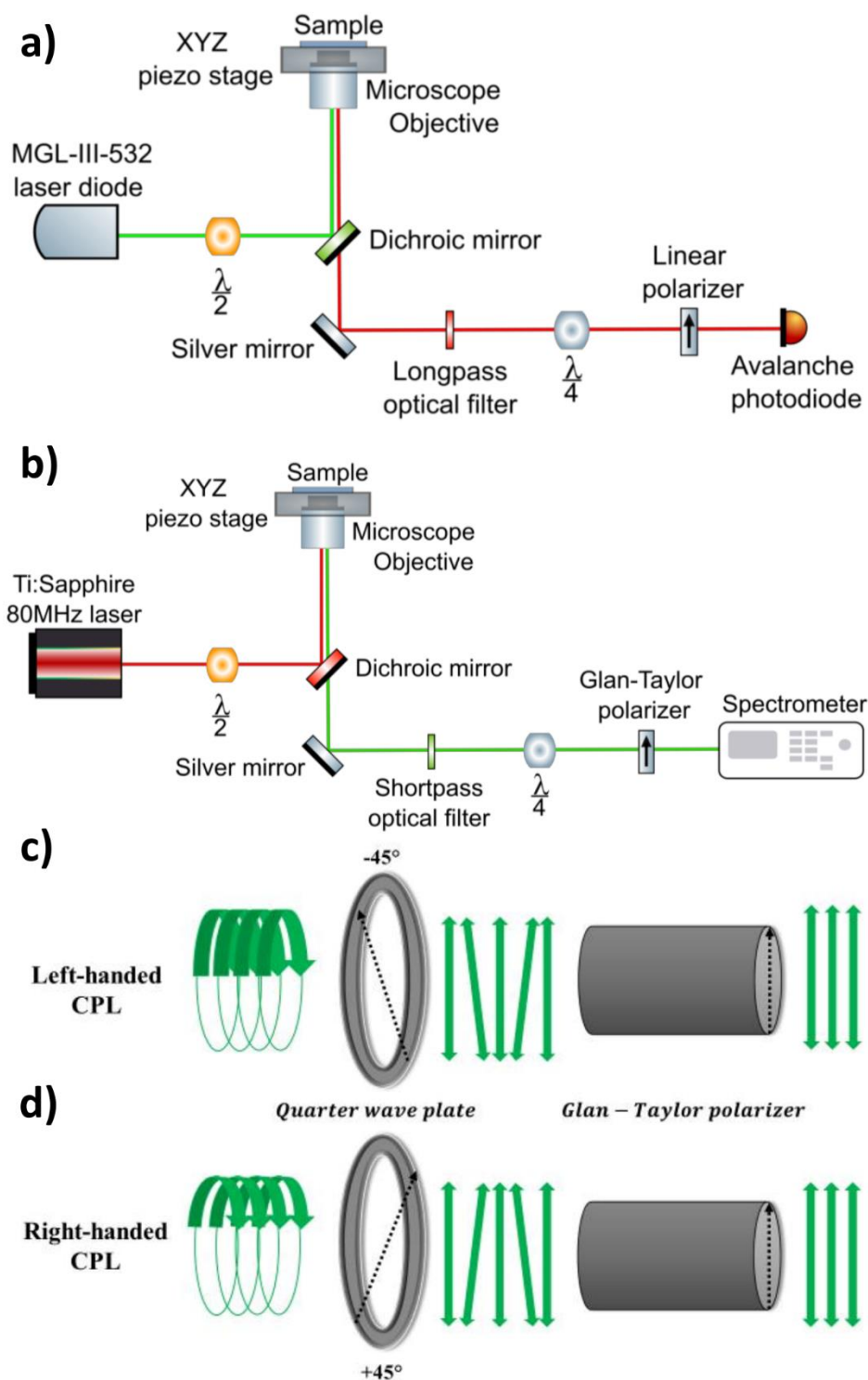


Figure 11. One- and Two-photon excited circularly polarized luminescence detection system and its principle of work. Scheme of one-photon (a) and two-photon (b) excited circularly polarized luminescence measuring system. System adjustment used during the measurement of left-handed (c) and right-handed (d) circularly polarized luminescence.

After assembling both setups, each of them was calibrated. The 1P-CPL setup sensitivity was checked using the solution of achiral $\text{Au}_{25}(\text{PET})_{18}$ nanoclusters,¹⁸⁶ by finding the appropriate arrangement of optical elements and polarization of the excitation light (controlled by a half-wave plate) resulting in a luminescence dissymmetry coefficient closest to 0. Since

the lowest luminescence dissymmetry factors calculated from scans of this sample (described in detail in chapter VI.1) was of the order of magnitude 10^{-3} , that was the detection limit of the 1PCPL system.

The 2P-CPL setup, due to the innovative nature of this system as well as the wide tunability of the excitation source (680 nm – 1080 nm), was calibrated using both achiral and chiral reference (Figure 12). First, the system was checked with an aqueous solution of achiral dye, fluorescein, characterized by strong fluorescence with a maximum located at 514 nm. The solution was excited at 900 nm and monitored from 460 nm to 600 nm. Two-photon excited L-CPL (Figure 12a, blue) and R-CPL (Figure 12a, red) spectra had similar shapes and relatively similar intensity. However, even after carefully adjusting the mutual QWP and polarizer orientation to collect both CPL handedness as well as the plane of excitation polarization, the difference between L-CPL and R-CPL signal was still non-zero (Figure 12b, bright green area). The calculated luminescence dissymmetry factor (Figure 12b, dark green line) at 514 nm was equal to -2×10^{-3} and, as a result, this value was determined to be the sensitivity limit of the constructed system. In addition, a chiral reference (europium tris[3-(trifluoromethylhydroxymethylene)-(+)-camphorate], $\text{Eu}[\text{facam}]_3$) was measured in order to confirm that the setup correctly detects the strength and handedness of measured chiral effects. The sample was excited at 750 nm, an excitation spectrum maximum of the studied material, and the emission was monitored in the range from 580 nm to 620 nm. As presented in Figure 12c, the emission spectrum was characterized by three bands, located at 585 nm, 595 nm and 612 nm. Comparing both CPL handedness revealed that L-CPL (Figure 12c, blue line) was stronger at 612 nm meanwhile R-CPL (Figure 12c, red line) was stronger at 585 nm and 595 nm, which is visible after analyzing the signal difference (Figure 12d, yellow area). The calculated dissymmetry factors (Figure 12d, orange line) were equal to -0.68 at 595 nm and $+0.09$ at 612 nm. Those $g_{2P\text{-lum}}$ values were close to the ones reported from 1P-CPL experiments (~ -0.78 at 612 nm and $+0.07$ at 595 nm)^{187, 188} and thus confirmed that equipment was sensing the CPL correctly. The differences between the recorded and reported values could be caused by the use of two-photon excitation. In other report, comparing 1P-CPL and 2P-CPL of Λ -Eu:L1 complexes, the dissymmetry factors also differed - $g_{1P\text{-lum}} = +0.30$ and $g_{2P\text{-lum}} = +0.25$.¹⁸⁹

Both discussed systems played an important role in my research. The 1P-CPL system was used to check the chiroptical properties of achiral $\text{Au}_{25}(\text{PET})_{18}$ induced due to their chiral assembly using the liquid crystalline template, discussed in detail further in the chapter “Optical properties of chiral heterostructures with gold nanoclusters”. Thanks to it, it was proven that such helical assembly of gold nanoclusters results in their circularly polarized luminescence, with signs depending on the local handedness of the matrix. The 2P-CPL system, described in detail in the chapter VI.1, was used to explore the chiroptical properties of chiral gold nanoclusters. It allowed me to discover that in the case of gold nanoclusters stabilized with 6-aza-2-thiothymine and functionalized with chiral L- and D-arginine ligands, the symmetry between absorption and emission is broken - enantiomers characterized by mirror reflection in the absorption spectrum emit luminescence with single handedness. What is more, the 2P-CPL setup created for my research purposes, along with the acquired results, is one of the first

presentations of this technique and its application, increasing the novelty of research conducted as part of my dissertation.

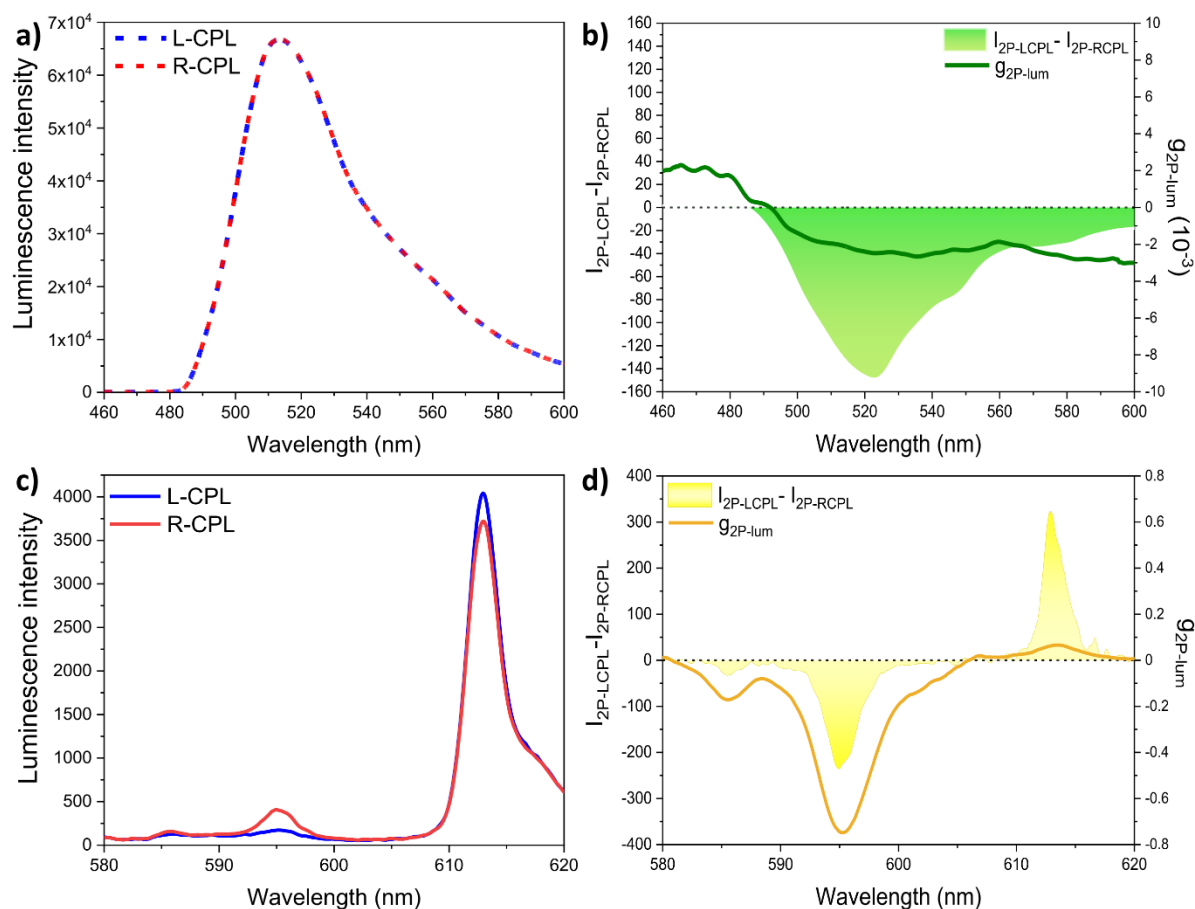


Figure 12. Two-photon excited circularly polarized luminescence and luminescence dissymmetry factors of reference materials. Left- and right-handed two-photon excited circularly polarized luminescence of fluorescein (a) and Eu[facam]₃ (c). 2P-CPL intensity difference and calculated luminescence dissymmetry factors of fluorescein (b) and Eu[facam]₃ (d).

VI. 2 Two-photon excited fluorescence lifetimes

Another technique developed during the work on my dissertation was a system to measure two-photon excited fluorescence lifetimes. It allowed me to investigate whether different nanomaterials have the same radiative relaxation paths following one-photon and two-photon absorption. In the case of my research, it was used to explore the differences between one-photon and two-photon excited fluorescence of chiral L-Arg/ATT-AuNCs and D-Arg/ATT-AuNCs, described in detail in the chapters VII.1 and VII.2.

The system was based on one of the most commonly used fluorescence lifetime measuring techniques - time-correlated single photon counting (TCSPC). TCSPC correlates the arrival time of a single photon at the detector with the time of the laser excitation pulse to provide the fluorescence decay curve. The fluorescence excitation source is a pulsed laser diode, with a controlled pulse frequency that allows monitoring of the decay curves within various time windows, from tens to thousands of nanoseconds. In the case of a two-photon excited system (Figure 13), the excitation source was a Chameleon Ti:Sapphire femtosecond laser with 80

MHz pulse frequency corresponding to 12.5 nanoseconds window between laser pulses. Because of such a short time window, preventing the measurement of most fluorescent samples, an APE pulseSelect pulse picker was installed to control the laser pulse repetition rate in the range from 80 MHz to 4 MHz, prolonging the available measuring time window to 250 ns. In order to operate correctly, the pulse picker received the information about the reference beam from the laser (reference INPUT in Figure 13) and transmitted the information about the modified beam with a changed repetition rate generated by the pulse picker to the TCSPC detector (reference OUTPUT in Figure 13). The fluorescence was collected using the Acton SpectraPro SP-2300 monochromator, coupled to an HPM-100-50 TCSPC detector, and operated via the included PC software. The sample mounted in a sample holder was excited with the modified laser beam, focused with a 20x Mitutoyo apochromatic objective, allowing to achieve high photon density required to efficiently induce two-photon absorption. Two-photon excited fluorescence was collected via the short-pass optical filter (filtered wavelength range changed depending on the sample) mounted next to the monochromator entrance slit.

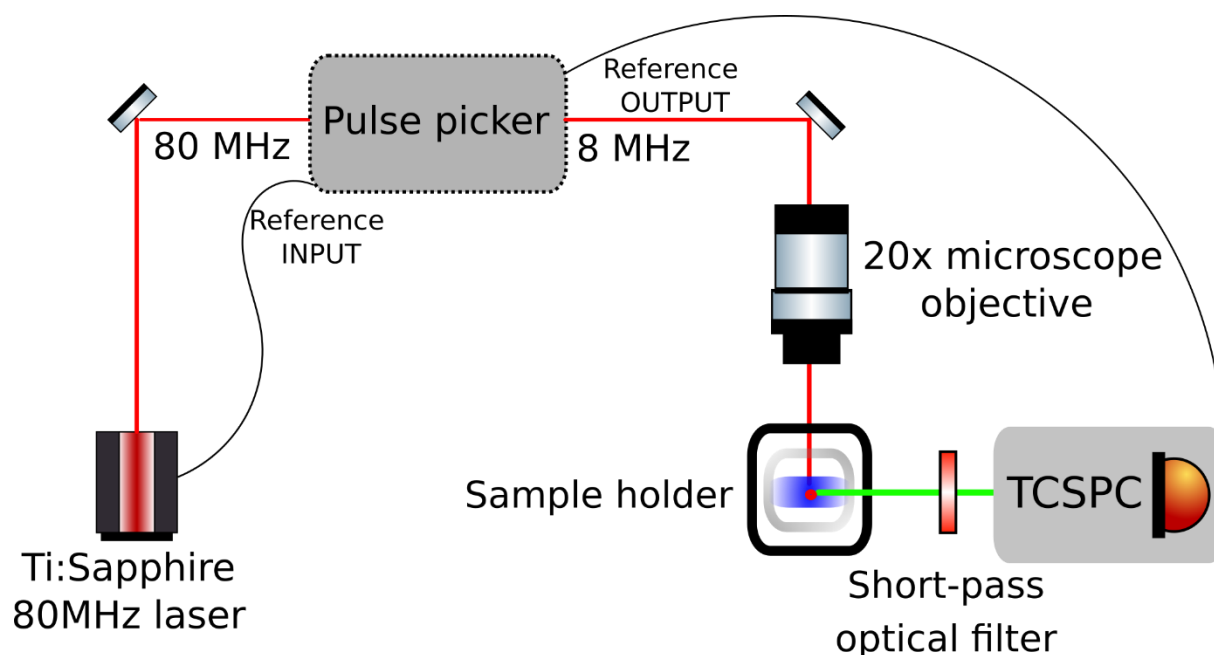


Figure 13. Scheme of the two-photon excited fluorescence lifetime measuring system.

After the assembly, the 2P TCSPC system was calibrated with 0.0001 M fluorescein dye solution (H₂O, pH 11). The sample was excited at 750 nm. The repetition rate was set to 8 MHz, creating a measuring window between pulses ~ 125 ns. The TCSPC coupled monochromator was set at 514 nm, the fluorescein emission maximum. A 700 nm short-pass optical filter was mounted, to cut off any scattered laser signal. A two-photon excited fluorescence decay curve (Figure 14, red curve) was collected over 60 seconds. The data collected from the 2P TCSPC system was compared with the data from the 1P TCSPC (Figure 14, black curve) experiment. 1P TCSPC system used the same detection path (Acton monochromator and HPM detector), but the excitation source was a 375 nm pulsed laser diode with a repetition rate of 20 MHz. The sample was excited directly with a laser diode, without

the microscope objective, required in two-photon measurements and the resulting fluorescence was collected with the same short-pass filter mounted. After the measurement, both decay curves were imported into the OriginLab software and fitted with one-exponential decay functions. The obtained results are presented in two tables shown in Figure 14. The fluorescence lifetimes determined from 1P and 2P TCSPC measurements were equal to 4.238 ± 0.008 ns and 4.211 ± 0.009 ns, respectively. The obtained values were close to the ones reported in the literature on the subject, oscillating between 4.1 ns and 4.2 ns.^{190, 191} Moreover, the difference between 1P and 2P measurements was smaller than 1%, proving that the 2P TCSPC system works correctly.

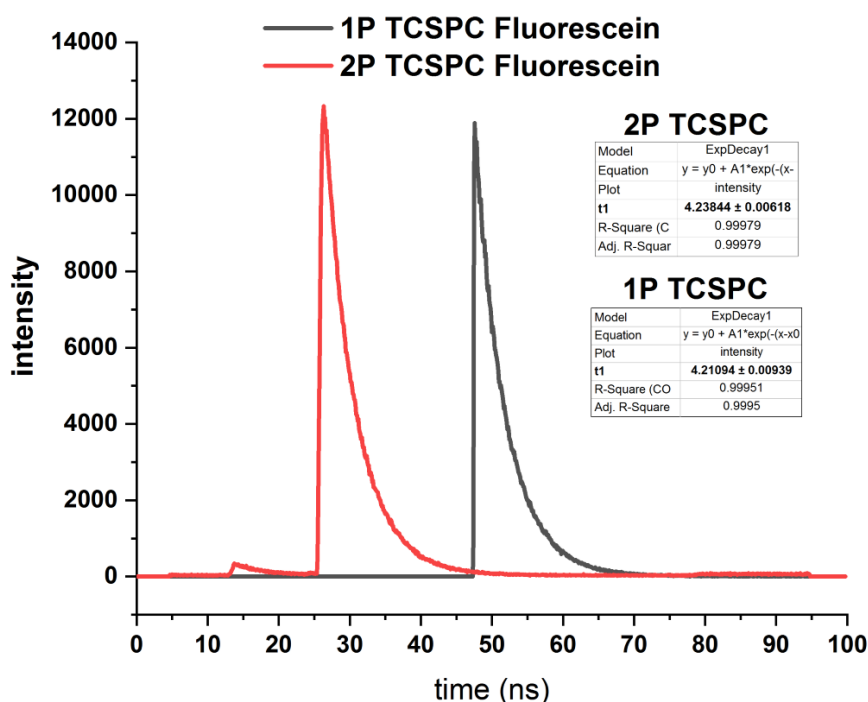


Figure 14. One- (1P TCSPC) and two-photon (2P TCSPC) excited fluorescence decay curve of fluorescein. The attached tables show the fluorescence lifetimes determined by analyzing both signals with a single-exponential curve.

Apart from my research on the fluorescence properties of chiral nanoclusters, the developed 2P TCSPC system was also vital to the studies on the two-photon excited fluorescence of amyloids conducted in collaboration with Manuela Grelich-Mucha.¹⁹² We discovered that the maximum of fluorescence of lysozyme amyloids red-shifts under two-photon excitation: from 450 nm under 1P excitation to 490 nm under 2P excitation (Figure 15). The origin of this behavior was explained by different relaxation pathways following both types of photoexcitation, which was confirmed by 1P and 2P TCSPC measurements resulting in average fluorescence lifetimes equal to 2.87 ns and 1.16 ns (lysozyme fibrils incubated without NaCl) and 2.99 ns and 2.08 ns (lysozyme fibrils incubated with 50 mM NaCl), respectively. Thus, further confirming the importance of this type of system in any research concerning the two-photon excited fluorescence and its origin.

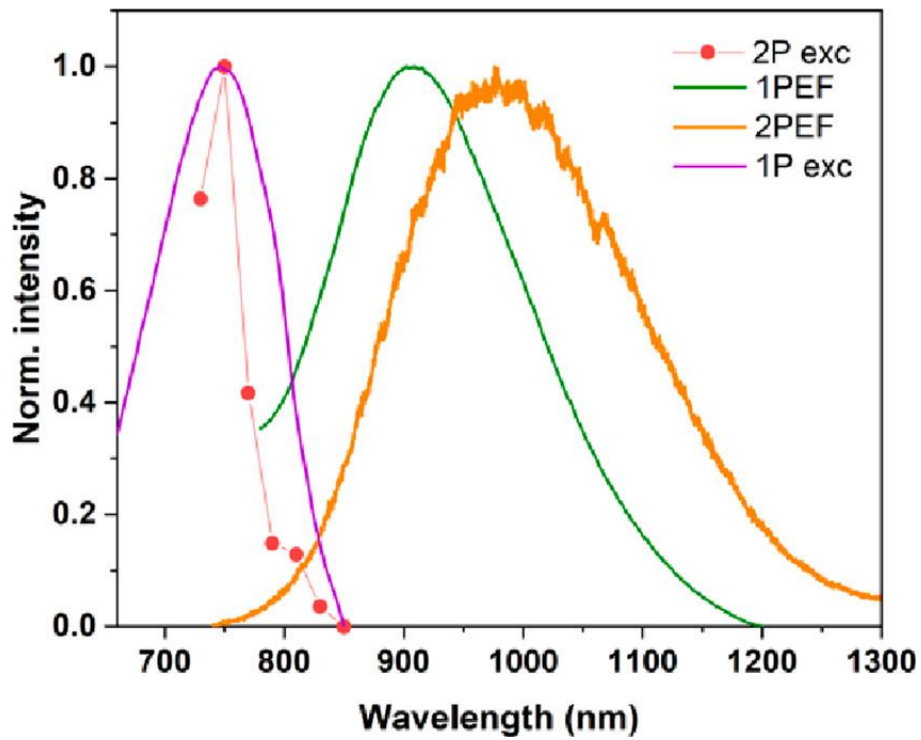


Figure 15. One-photon and two-photon excited autofluorescence of lysozyme amyloids. Correlation between normalized two-photon (2P exc) and one-photon (1P exc) excitation spectrum and between normalized one-photon (1PEF) and two-photon (2PEF) excited emission spectrum of lysozyme fibrils incubated without NaCl. Reprinted from reference no.¹⁹² under Creative Commons Attribution 4.0 (CC BY 4.0) license.

Results

VII. Chiroptical properties of chiral gold nanoclusters

Hypothesis: *The chirality transfer from chiral ligands to achiral gold nanocluster can influence their absorption properties and induce circularly polarized luminescence*

Recent years have shown a growing interest in chiral nanomaterials due to their controllable and unique optical properties. As was already mentioned in the introductory part of this thesis, gold nanoclusters are no exception. Thanks to easy surface modification with appropriate ligands, even non-chiral nanoclusters can gain chiral optical properties.¹⁶⁰ However, the non-linear chiral optical properties of gold nanoclusters are still neither well explored, nor understood. Last year, Pniakowska et al. showed in their work the two-photon circular dichroism (TPCD) of gold nanoclusters, which was much stronger than its one-photon counterpart.¹⁶⁵ However, there are no published reports about the two-photon circularly polarized luminescence of gold nanoclusters and its possible origins.

One of the hypotheses I want to answer in this dissertation concerns the chiral non-linear optical properties of chiral gold nanoclusters. As was already mentioned in the literature review, gold nanoclusters possess non-linear properties such as strong two-photon excited fluorescence or high two-photon absorption cross-sections.¹⁴⁵ However, there are only a few works on their chiral non-linear optical properties, which were discussed in more detail in the chapter IV. 3.

This chapter presents my research on the chiroptical properties of gold nanoclusters stabilized with 6-aza-2-thiothymine (ATTAuNCs), which become chiral after functionalization with L-arginine (L-Arg/ATTAuNCs) and D-arginine (D-Arg/ATTAuNCs) ligands. It shows my findings concerning the circularly polarized luminescence of nanoclusters mentioned above, measured under both, one-photon and two-photon photoexcitation. This chapter also contains a discussion on the discovered chiral optical properties of ATTAuNCs and their possible origin.

VII. 1 Materials & methods

Materials

6-Aza-2-thiothymine (Alfa Aesar Chemicals), gold (III) chloride trihydrate ($\text{HAuCl}_4 \cdot 3\text{H}_2\text{O}$, >99.99%, Sigma-Aldrich), L-arginine ($\geq 98\%$ (TLC), Sigma-Aldrich), D-arginine ($\geq 98\%$ (TLC), Sigma-Aldrich), Sodium Hydroxide (NaOH , $\geq 98\%$, Sigma Aldrich), Fluorescein (Sigma-Aldrich), Europium tris[3-(trifluoromethylhydroxymethylene)-(+)-camphorate] ($\text{Eu}(\text{facam})_3$). Percentages in brackets indicate the purity of a given reagent.

Methods

Optical properties characterization: Because of the high concentration of gold nanocluster stock solutions after synthesis and functionalization, each type of nanocluster was diluted with a water buffer (pH10, NaOH) to a final concentration of 0.1 mg/mL. The absorption spectra of all samples were measured using a JASCO V-670 spectrometer. All absorption spectra shown in this chapter are drawn after subtracting the reference signal (water buffer pH10) from the sample signal. The fluorescence emission and excitation spectra of all samples were measured using FS5 Spectrofluorometer (Edinburgh Instruments). During fluorescence emission spectra measurements, the samples were excited at 412 nm and during the fluorescence excitation spectra measurements the signal was monitored at 530 nm. Both absorption and fluorescence spectra were measured using 0.5 mL quartz cuvettes.

Fluorescence lifetimes measurements: One-photon fluorescence lifetimes were measured using the TCSPC (time-correlated single-photon counting) module of FS5 Spectrofluorometer (Edinburgh Instruments) and two-photon fluorescence lifetimes were measured using the home-built 2P-TCSPC system described in the chapter VI.2. One-photon fluorescence decay curves were excited with a pulsed picosecond diode laser at 450 nm and collected at 530 nm. Two-photon fluorescence decays were excited with a Ti:Sapphire femtosecond laser at 825 nm and also collected at 530 nm with a mounted short-pass 700 nm optical filter.

Chiroptical properties characterization: Circular dichroism spectra of all samples were measured using a Jasco J-1500 spectropolarimeter using the 0.5 mL quartz cuvettes. Spectra were collected in the range from 320 nm to 500 nm, accumulated three times, and then averaged. Each spectrum shown in the dissertation was corrected with a signal from a reference sample – the water buffer with pH10. Circularly polarized luminescence spectra were measured using a CPL Solo II from OLIS (in collaboration with Dr. Guillermo Martínez-Denegri and Dr. Piotr Ślęczkowski from Łódź University of Technology) with an excitation wavelength of 405 nm. Each CPL signal shown in the dissertation is an averaged spectrum from 100 continuous scans.

Non-linear chiroptical properties characterization: Two-photon excited circularly polarized luminescence spectra were collected using the 2P-CPL setup described in detail in chapter VI. 1 from the Experimental Methods section. All nanocluster samples were excited at 825 nm. The excitation power was ~ 10 mW and it was filtered with a 750 nm longpass filter (FELH0750, Thorlabs).

VII. 2 Synthesis, purification and functionalization of ATT-AuNCs

ATT-AuNCs were synthesized following the protocol reported in other papers on the subject, exploring the properties of these nanoclusters.^{20, 165, 193} First, 80 mM of 6-Aza-2-thiothymine was dissolved in a 5 ml MiliQ water solution with 0.2 M NaOH, resulting in pH~10. Then, 5 ml of 10 mg/mL H₂AuCl₄·3H₂O was added to the ATT solution via fast injection using an automatic pipette. The mixture was stirred at room temperature (23°C) for around one hour. While stirring, a solution colour change was observed - from dark red to light yellow. Then nanoclusters solution was filtered during ultrafiltration with 50 kDa Millipore filters at 7 000 rpm for 10 min. After the filtration, the nanoclusters were dissolved in 5 ml of the same pH~10 aqueous solution as used for dissolving ATT. As-prepared nanoclusters were stored in the dark at 4°C.

Functionalization of ATT-AuNCs started with dissolving the powder forms of both chiral ligands, L- and D-arginine in MiliQ water solution (0.2 M NaOH, pH~10) to obtain 40 mM solutions. Then, in two separate vials, 2 mL of ATTAuNCs were mixed with 230 µL of each ligand solution and left for 24 hours in a thermoblock at 37 °C without stirring. After the functionalization, L-Arg/ATTAuNCs and D-Arg/ATTAuNCs were stored in the dark at 4°C.

After functionalization, both Arg-coated samples were purified again using column chromatography. 2 mL of each stock solution of Arg/ATT-AuNCs were passed through the filtration medium (Sephadex G50) dissolved in the previously used MiliQ/NaOH aqueous solution. During the chromatography, both samples were divided into two separate fractions characterized by different colours (Figure 16a). The first fraction denoted as L1 for L-Arg/ATTAuNCs and D1 for D-Arg/ATTAuNCs was yellow-brown, meanwhile the second fraction (L2 and D2, respectively) was yellow-green. Each fraction was collected in a separate glass vial and characterized using UV-Vis spectroscopy.

VII. 3 Optical characterization of ATT-AuNCs before and after the functionalization with arginine

As presented in Figure 16b (black line), ATT stabilized gold nanoclusters, measured after synthesis and purification, were characterized with two bands, localized at 415 nm and 480 nm. Absorption spectra of arginine functionalized ATT gold nanoclusters (Figure 16b, blue and red lines) were characterized with three bands. The differences seen in absorption (ABS) spectra of ATTAuNCs and Arg/ATTAuNCs are reported to be connected with distortion of the nanocluster core during the arginine functionalization.¹⁹³ There was a visible difference between the bands in spectra of fractions L1/D1 and L2/D2. On the other hand, fractions denoted with the same numbers (L1 and D1, L2 and D2) strongly resembled each other, indicating that changing the chirality of the ligand itself does not have a major impact on the absorption spectrum. The absorption bands of L1 and D1 fractions were located at 400 nm, 475 nm, and 500 nm meanwhile the bands of L2 and D2 fractions were located at 405 nm, 465 nm, and 505 nm. Since the number and localization of ABS bands of L2 and D2 fractions agreed the most with the previous reports on ATT and Arg-ATT gold nanoclusters,^{20, 165} I have used them in all further experiments.

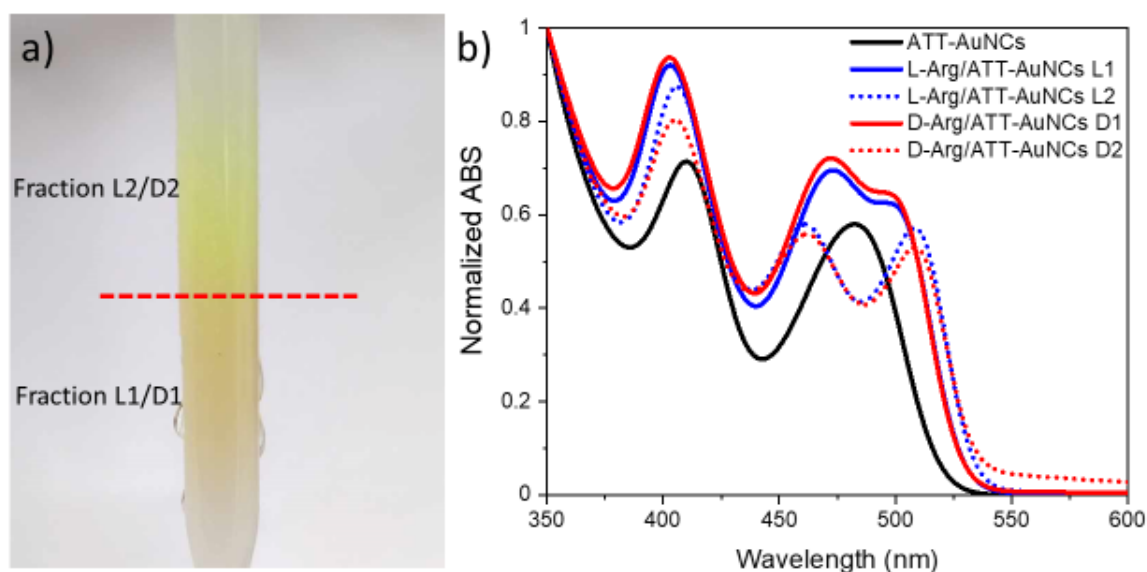


Figure 16. Column chromatography and normalized absorption spectra of ATT stabilized gold nanoclusters. The photo showing two fractions separated during column chromatography of L-Arg/ATT-AuNCs (a). Normalized absorption spectra of ATTAuNCs (black line) and both fractions of L-Arg/ATT-AuNCs (blue lines) and D-Arg/ATTAuNCs (red lines) (b).

After confirming the absorptive properties of ATTAuNCs, I measured their fluorescence excitation and emission spectra, presented in Figure 17a and Figure 17b, respectively. In the excitation spectra of ATTAuNCs (Fig 17a, black line) the bands were located at 325 nm, 410 nm and 490 nm. Fluorescence excitation bands measured for L-Arg and D-Arg coated gold nanoclusters had a similar shape and were located at similar wavelengths: 330 nm, 405 nm, 455 nm and 510 nm. Comparing the fluorescence excitation bands above 400 nm with corresponding absorption spectra shows that in the case of all three samples they are located in a similar wavelength range.

Fluorescence emission spectra were measured upon excitation at 410 nm to excite the strongest band visible in the excitation spectra of arginine-coated ATTAuNCs. The maxima of fluorescence emission spectra of ATTAuNCs (Figure 17b, black line), L-Arg/ATTAuNCs (Figure 17b, blue line) and D-Arg/ATTAuNCs (Figure 17b, red line) were all located at 530 nm. It confirmed that functionalizing ATTAuNCs with chiral arginine ligands does not shift the emission band. However, it strongly influenced the fluorescence intensity, since the PL emission intensity of ATTAuNCs was two orders of magnitude smaller than the fluorescence intensity of Arg-coated gold nanoclusters. Such differences in the fluorescence intensities before and after arginine functionalization are reported to be caused by a large increase in fluorescence quantum yield after the functionalization. It increases from 0.3% - 1.3% reported for ATTAuNCs to 58.4% and 63.2% reported for D-Arg/ATTAuNCs and L-Arg/ATTAuNCs.^{165, 193} According to research by Deng *et al*,²⁰ coating the ATTAuNCs with chiral L-arginine and D-arginine ligands rigidifies the nanocluster structure, which reduces intrastructural vibration and rotation. As a result, the impact of non-radiative relaxation pathways lowers, meanwhile the share of radiative relaxation pathways increases, resulting in the strong increase in photoluminescence quantum yield and intensity, which was also confirmed by the presented experiment.

In the end, before measuring the chiroptical properties of ATTAuNCs and Arg/ATTAuNCs, I measured their two-photon excited photoluminescence, presented in Figure 17c. All 2PL spectra were excited at 825 nm. The two-photon excited emission maximum of all samples was located at the same wavelength as in the case of one-photon excitation (Figure 17b) and equal to 530 nm. Moreover, similarly to 1PF spectra, the intensity of Arg/ATTAuNCs 2PL was two orders of magnitude higher than ATT-AuNCs, which, as explained before, is connected to differences between the quantum yields of both type of samples. All in all, this experiment has confirmed, that ATTAuNCs and Arg/ATTAuNCs are efficient two-photon excited fluorescence emitters, which made it possible to study their two-photon excited CPL, described later in this chapter.

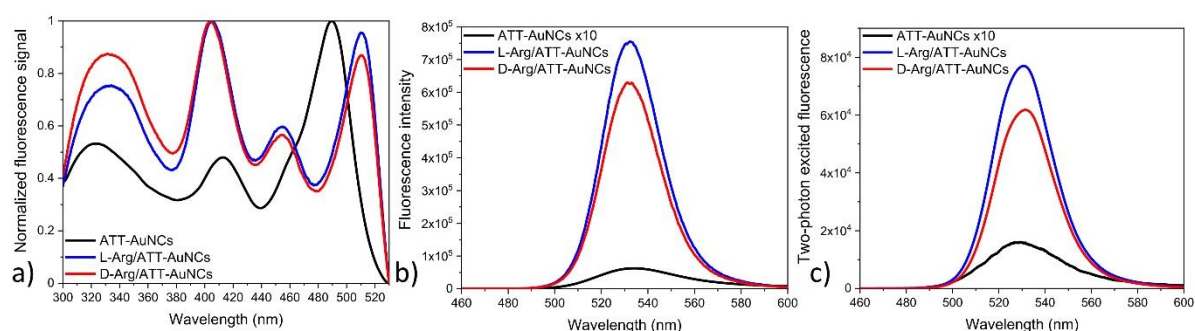


Figure 17. Fluorescence spectra of ATT and Arg/ATT gold nanoclusters. Fluorescence excitation spectra (a) are normalized to better represent the differences between unfunctionalized and functionalized ATT gold nanoclusters. In one-photon excited (b) and two-photon excited (c) fluorescence emission spectra, the emission spectrum of ATTAuNCs (black line) is multiplied 10 times. Fluorescence excitation spectra were monitored at $\lambda_{em} = 530 \text{ nm}$ and fluorescence 1P and 2P emission spectra excited at $\lambda_{exc} = 412 \text{ nm}$ and $\lambda_{exc} = 825 \text{ nm}$, respectively.

VII. 4 Linear chiroptical properties

I started measuring the chiral optical properties of ATTAuNCs and Arg/ATTAuNCs from their circular dichroism spectra, presented in Figure 18. The signal from ATTAuNCs (Figure 18, black line) was equal to 0 mdeg within the whole measuring range, extending from 320 nm to 550 nm. On the other hand, the CD signal of two chiral enantiomers (Figure 18, blue and red lines) clearly showed three mirror-reflected bands: the first one located at 350nm, the second one at 415 nm and the last one at 460 nm. The CD spectrum of L-Arg/ATT-AuNCs (Figure 18, blue line) was characterized by negative values in the range up to -30 mdeg at the maximum of the strongest bands located at 415 nm, pointing at stronger absorption of right-handed circularly polarized light. Meanwhile, the CD spectrum of D-Arg/ATT-AuNCs (Figure 18, red line) was characterized by positive values up to +32 mdeg at the maximum of the strongest band, also located at 415 nm, which pointed at overall stronger absorption of left-handed circularly polarized light. Comparing the CD signals of ATTAuNCs before and after the functionalization with chiral arginine ligands clearly shows that the emergence of chiral optical absorptive properties in Arg/ATTAuNCs is connected with the chiral coating of intrinsically achiral gold nanocluster. Moreover, the results I presented agreed with the CD spectra of ATTAuNCs and Arg/ATTAuNCs gold nanoclusters reported by Pniakowska *et al.*¹⁶⁵ However, apart from the three strong bands, already reported in the literature, I have also observed a fourth band with magnitude around 1 mdeg, located at 505 nm and visible in the CD

of both L-Arg/ATTAuNCs and D-Arg/ATTAuNCs (inset in Figure 18). Since the location of these weak band coincides with the location of the most red-shifted bands visible in the ABS spectra of both enantiomers (Figure 16b), my measurements prove that also these bands are sensitive to circular polarization of light, which was not reported before.

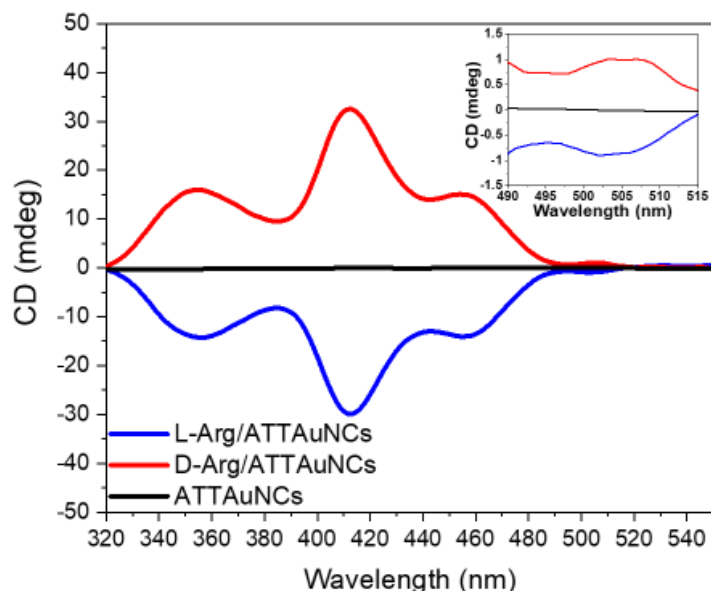


Figure 18. Circular dichroism spectra of ATTA and Arg/ATTA gold nanoclusters.

After confirming CD of Arg/ATTAuNCs I checked if the chirality is also conserved in the emission of studied gold nanoclusters by measuring the circularly polarized luminescence, presented in Figure 19. The CPL spectra were measured in cooperation with Dr. Guillermo Martínez-Denegri and Dr. Piotr Ślęczkowski from the International Centre for Research on Innovative Biobased Materials, at Łódź University of Technology. The results are presented both as intensity differences ($I_{L-CPL} - I_{R-CPL}$) and luminescence dissymmetry factors (g_{1Plum}), commonly used to compare the chiral emitting samples, and calculated according to the formula (eq. 14) described in the chapter VI.1. Surprisingly L-Arg/ATTAuNCs, characterized by negative CD signal, (Figure 19a) emitted stronger left-handed circularly polarized luminescence as proved by both positive signal after calculating the intensity difference and g_{1Plum} values. The maximum difference between CPL intensities was located at 535 nm, slightly off the photoluminescence emission maximum reported for this sample and the g_{1Plum} was oscillating around +0.001 in the whole measured range (510 nm to 550 nm). In case of D-Arg/ATTAuNCs (Figure 19b), the CPL signal agreed with the measured CD signal, also stronger emitting the left-handed circularly polarized luminescence, proven by both positive intensity difference with maximum at 532 nm and the higher g_{1Plum} oscillating around +0.0015. Since both enantiomers emitted the CPL of the same sign, which raised a question about its origins, I also checked the CPL signal of unfunctionalized, achiral ATTAuNCs. As could be seen in Figure 19c, ATTAuNCs also emitted circularly polarized luminescence of the same sign as both enantiomers. The left-handed CPL was again stronger than its right-handed counterpart and g_{1Plum} was oscillating around +0.002 in the whole measured range.

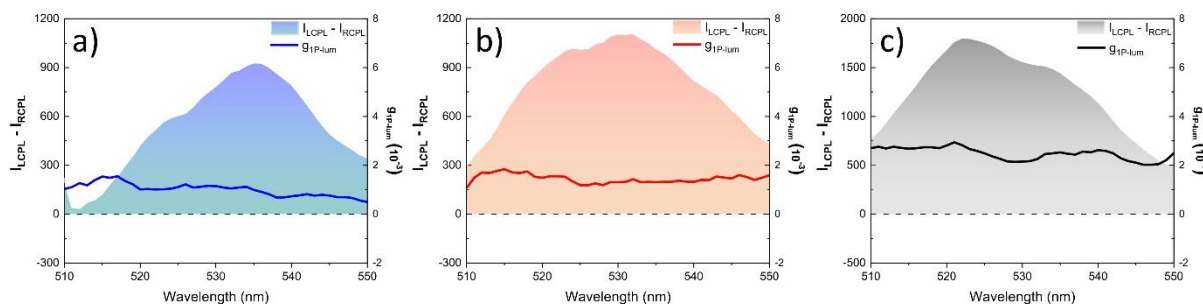


Figure 19. Circularly polarized luminescence spectra of ATTAuNCs (a), L-Arg/ATTAuNCs (b) and D-Arg/ATTAuNCs (c). Each figure presents the intensity difference between left-handed and right-handed circularly polarized luminescence (shaded bands) and luminescence dissymmetry factors (solid lines) calculated from those differences.

However, why did all three types of nanoclusters emit circularly polarized luminescence of the same sign and order of magnitude while having different mirror-like circular dichroism spectra?

According to the literature, the gold nanocluster's luminescence can originate from the kernel-structure relaxation¹⁹⁴ or ligand-to-metal charge transfer¹⁹⁵. Meanwhile, their optical absorption is connected not only to the nanocluster core but, most importantly, their surface: the staple motifs and ligands coating the nanoclusters.¹⁹⁴ The circular dichroism spectra (Figure 18) presented in this chapter confirmed that chirality of ATTAuNCs could be observed only after functionalization with chiral ligands – L-Arg and D-Arg. On the other hand, CPL spectra (Figure 19) showed that even ATTAuNCs without chiral ligand coating can emit circularly polarized luminescence. This means that the origin of the observed effect lies in the nanocluster core. Both Deng²⁰ and Wei¹⁹⁶ have reported that ATT gold nanoclusters surface functionalization does not affect their core, which, as they both stated, plays a major role in ATT gold nanoclusters luminescence. Also, Zhong *et al.* have shown that functionalization rigidifies the ATTAuNCs structure, lowering the impact of non-radiative relaxation and strongly increasing their luminescence quantum yields, but does not change the nanocluster core.¹⁹³ Taking all of that into account, it is possible that functionalizing the ATTAuNCs surface with L-Arg and D-Arg ligands decreases the influence of non-radiative relaxation on their luminescence, but does not change the chirality of its excited state, which is intrinsically connected with the electronic transitions within the ATTAuNCs nanoclusters core.

VII. 5 Non-linear chiroptical properties

In the end, I also checked if a similar broken symmetry between chiral emission and absorption could be observed in non-linear chiroptical properties of ATTAuNCs and Arg/ATTAuNCs nanoclusters. I measured their two-photon excited circularly polarized luminescence, which is presented in Figure 20. Similarly to one-photon excited CPL measurements, ATTAuNCs and its two arginine-coated enantiomers emitted strong left-handed circularly polarized luminescence. The two-photon excited luminescence dissymmetry factors (g_{2P-lum}), shown in Figure 20 as solid one-coloured lines, were calculated using the eq. 15 described in chapter VI.1. Unlike one-photon measurements, in all three differential spectra ($I_{2P-LCPL} - I_{2P-RCPL}$) and g_{2P-lum} there was a visible maximum, located at 531 nm:

the wavelength corresponding to emission maximum measured in both one-photon (Figure 17b) and two-photon (Figure 17c) excited luminescence spectra. Moreover, similarly to g_{1P-lum} , the calculated values of g_{2P-lum} of all three samples were comparable: +0.043, +0.048 and +0.048 for L-Arg/ATT-AuNCs (Figure 20a) and D-Arg/ATT-AuNCs (Figure 20b) and ATTAuNCs (Figure 20c), respectively. What is important, the luminescence dissymmetry factors of ATTAuNCs were higher (L-Arg/ATTAuNCs) or equal (D-Arg/ATTAuNCs) to g_{2P-lum} of both chiral enantiomers, proving that 2PCPL of ATTAuNCs is not connected to the chiral ligands but the nanocluster core, similarly to 1PCPL.

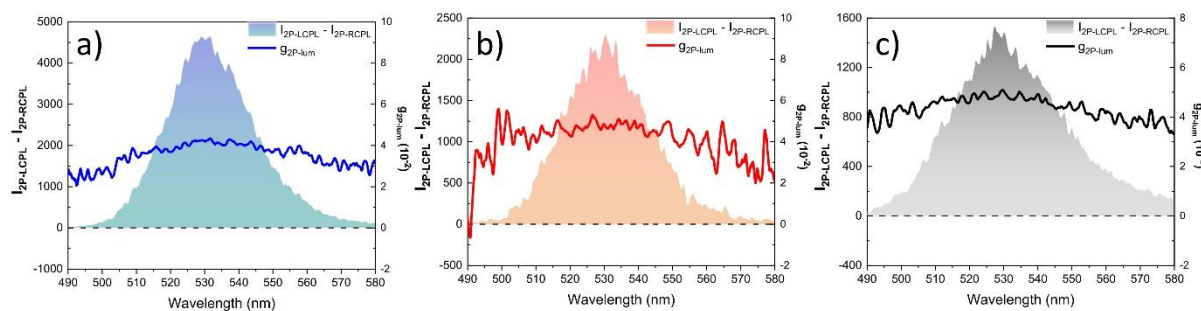


Figure 20. Two-photon excited circularly polarized luminescence spectra of ATT (a) and Arg/ATT (b, c) gold nanoclusters. Each figure presents the intensity difference between left-handed and right-handed circularly polarized luminescence (shaded bands) and luminescence dissymmetry factors (solid lines) calculated from those differences.

However, comparing the values of luminescence dissymmetry factors calculated from 1PCPL and 2PCPL shows, that CPL resulting from the non-linear optical process is characterized by a stronger chiral response of order 10^{-2} compared to 10^{-3} from 1PCPL. If the luminescence in both cases results from the same lowest excited state, it should result in CPL of similar sign and strength. 1PCPL and 2PCPL of Arg/ATT and ATT gold nanoclusters are characterized by the same handedness, but differ in the order of magnitude of luminescence dissymmetry factors. The effect of the system could be excluded because measurements of chiral reference $\text{Eu}(\text{facam})_3$ (Figure 12c, d), presented in the section on the principles of work of the 2PCPL system, showed that the luminescence dissymmetry factor values calculated from 1PCPL and 2PCPL coincide. Moreover, according to the scarce literature on two-photon excited CPL studies of other materials, mostly strongly chiral europium complexes, the luminescence dissymmetry factors calculated from 1PCPL and 2PCPL studies could be slightly different, but never by the order of magnitude.^{189, 197} In addition, a matter of sample preparation also could be excluded since both types of CPL were measured using the same samples, with the same sample concentrations. The source of the observed differences should therefore be sought in the behaviour of this particular sample under one-photon and two-photon photoexcitation. If the radiative relaxation pathways following one-photon and two-photon absorption are different, then the luminescence comes from different excited states, which could give different chiral responses. To verify that I measured both one-photon excited and two-photon excited luminescence lifetimes. Both measurements were based on the time-correlated single-photon counting (TCSPC) method. One-photon excited PL lifetimes (Figure 21a, b) were measured using the fluorescence lifetime measuring system of FS5 spectrofluorometer (one-

photon TCSPC) and two-photon excited PL lifetimes (Figure 21c, d) were measured with the home-built system described in detail in chapter VI.2.

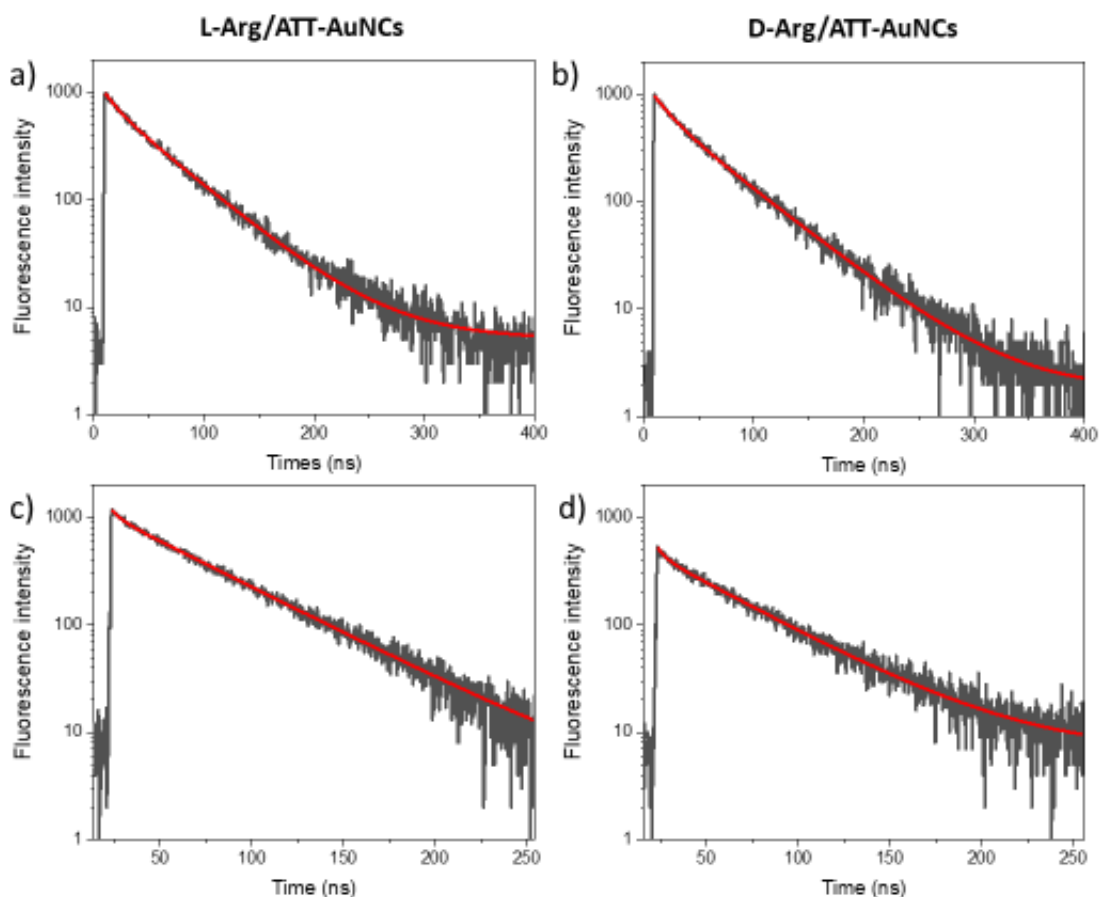


Figure 21. One-photon (a, b) and two-photon (c, d) excited luminescence decay curves of L- and D-Arg/ATT-AuNCs. Red lines show the software-determined exponential decay curves that best fit each of the luminescence decays.

Table 1. One-photon and two-photon excited fluorescence lifetimes of L-Arg/ATT-AuNCs and D-Arg/ATT-AuNCs. The contribution of each lifetime component is shown as a percentage.

	τ_1 [ns]	τ_2 [ns]	τ_{avr} [ns]
One-photon excited photoluminescence			
L-Arg/ATT-AuNCs	12.5 ± 1.0 33.5%	50.9 ± 0.6 66.5%	46.7 ± 0.9
D-Arg/ATT-AuNCs	16.8 ± 1.0 38.2%	54.3 ± 0.8 61.8%	48.3 ± 0.9
Two-photon excited photoluminescence			
L-Arg/ATT-AuNCs	6.0 ± 0.6 83.5%	51.5 ± 0.4 16.5%	34.4 ± 0.6
D-Arg/ATT-AuNCs	5.3 ± 0.6 91.7%	47.9 ± 0.6 8.3%	24.5 ± 0.6

All PL decays were fitted using two-exponential decay curves, therefore, in both cases, relaxation occurred through two electronic states with different lifetimes. All lifetimes determined from the 1P-TCSPC and 2P-TCSPC measurements of L-Arg/ATT-AuNCs and D-Arg/ATT-AuNCs, together with the percentage contribution of each of the lifetime components to their average, are shown in Table 1. Photoluminescence lifetimes determined from one-photon measurements were equal to $\tau_1 = 12.5$ ns and $\tau_2 = 50.9$ ns for L-Arg/ATT-AuNCs and $\tau_1 = 16.8$ ns and $\tau_2 = 54.3$ ns for D-Arg/ATT-AuNCs, resulting in the average lifetimes equal to 46.7 ns and 48.3 ns, respectively. In the case of both nanoclusters, the shorter lifetime components constituted 33.5% and 38.2 % meanwhile, the longer ones were responsible for 66.5% and 61.8% of their average lifetimes, respectively. Photoluminescence lifetimes determined from two-photon measurements were equal to $\tau_1 = 6.0$ ns and $\tau_2 = 51.5$ ns for L-Arg/ATT-AuNCs and $\tau_1 = 5.3$ ns and $\tau_2 = 47.9$ ns for D-Arg/ATT-AuNCs, resulting in average lifetimes equal to 34.4 ns and 24.5 ns, respectively. However, in this case, the shorter lifetime components constituted 83.5% and 91.7 % meanwhile, the longer lifetimes were responsible for 16.5% and 8.3% of the average lifetimes of L-Arg/ATT-AuNCs and D-Arg/ATT-AuNCs, respectively. The average PL lifetimes measured during one-photon measurements agree well with the values given in the literature, ranging from 42 ns to 86 ns, depending on the report,^{20, 165} and strongly resemble PL lifetimes reported by Pniakowska et al.,¹⁶⁵ equal to 42.7 ns for L-Arg/ATT-AuNCs and 42.9 ns for D-Arg/ATT-AuNCs. However, the two-photon PL lifetimes are observably shorter. Since it cannot be explained by the technical differences between the two measuring systems, as proved by similar one-photon and two-photon lifetimes of reference dyes (see Experimental Methods), the source of differences could lie in different relaxation pathways upon one-photon and two-photon excitation. First of all, the smaller two-photon excited PL lifetime components are much shorter than their one-photon counterparts. Firstly, this is indicated by shorter τ_1 lifetimes determined from two-photon excited PL decays. Moreover, they fit within the range of average lifetimes reported for unfunctionalized ATTAuNCs spanning from 3.5 ns to 7.1 ns.^{165, 193} Secondly, the shorter lifetime components derived from 2PTCSPC measurements contribute almost three times as much to average lifetimes as their one-photon counterparts (83.5% vs 33.5% for L-Arg/ATT-AuNCs), which may indicate that, in opposition to one-photon excited lifetimes, they play a major role during radiative relaxation following two-photon excitation L-Arg/ATT-AuNCs and D-Arg/ATT-AuNCs. Taking into account both arguments presented above, my research indicates that in the case of L-Arg/ATT-AuNCs and D-Arg/ATT-AuNCs, there are different radiative relaxation paths following one-photon and two-photon excitation, which can explain the observed differences in CPL efficiency.

VII. 6 Conclusions

In this chapter, I presented my research concerning the optical properties of chiral nanoclusters L-Arg/ATT-AuNCs and D-Arg/ATT-AuNCs as well as unfunctionalized ATTAuNCs. By performing the column chromatography, I showed that after the arginine functionalisation of ATTAuNCs surface, two fractions can be distinguished in enantiomer samples, characterized by distinct absorption spectra. Moreover, I explored the fluorescent properties of all three nanoclusters and confirmed that functionalization influences both their fluorescence excitation, by shifting the band locations and introducing new ones, and emission,

by strongly increasing the fluorescence quantum yields of L-Arg/ATTAuNCs and D-Arg/ATTAuNCs. In addition, strong two-photon excited fluorescence spectra of all three samples confirmed that all of them are efficient two-photon emitters. To check the influence of chiral arginine ligands on the chiroptical properties of ATTAuNCs, I measured their circular dichroism spectra and circularly polarized luminescence spectra, both one-photon and two-photon excited. Collected CD of L-Arg/ATTAuNCs and D-Arg/ATTAuNCs confirmed that coating the achiral ATTAuNCs with chiral arginine ligands induces a strong mirror-like chiral response in their optical absorption. The spectrum of ATTAuNCs was CD silent meanwhile the spectra of both chiral enantiomers were characterized with four bands of different signs (+CD for D-Arg/ATTAuNCs and -CD for L-Arg/ATTAuNCs), located at 350 nm, 415 nm, 460 nm and 505 nm. Surprisingly, one-photon and two-photon excited CPL studies, have not only shown that all three samples, including ATTAuNCs, could emit strong circularly polarized luminescence but also – that it is of one-handedness, independently from the geometry of ligands coating the ATTAuNCs. The luminescence dissymmetry factors were of the order of magnitude of 10^{-3} and 10^{-2} for one-photon and two-photon excited CPL, respectively. The discovered broken symmetry between chiral absorption and chiral emission of L-Arg/ATTAuNCs and D-Arg/ATTAuNCs was explained by the nanocluster core origin of circularly polarized luminescence, since according to other reports, it remains unchanged during the nanocluster functionalization. Furthermore, I presented and analysed the one-photon and two-photon excited luminescence lifetimes of all three samples, to explain the observed differences in strength of one-photon and two-photon excited CPL. These results indicated, that one-photon excited luminescence and two-photon excited luminescence follows a different radiative relaxation pathway, which could result in differences between the 1P and 2P excited CPL of discussed nanomaterials. All in all, the results and discussion presented in this chapter of my dissertation have proved the hypothesis put forward at the beginning of the chapter: the chirality transfer from chiral arginine ligands to achiral ATTAuNCs gold nanocluster influenced their absorption properties, confirmed via CD measurements. However, it does not influenced the chirality of both one-photon and two-photon excited photoluminescence.

VIII. Optical properties of chiral heterostructures with gold nanoclusters

Hypothesis: *Optically achiral gold nanoclusters can obtain chiral optical properties upon binding to liquid-crystalline helical nanofilaments.*

As stated in the literature review of this dissertation, intrinsically non-chiral gold nanoparticles can gain chirality via different modifications – functionalization with chiral ligands, helical self-assembly using dipolar interactions, or assembly due to binding to a chiral template. From all the reported templates, liquid crystalline materials seemed to be especially interesting, since they allow to switch the chirality of chiroptical properties of such heterostructures by controlling the template.¹⁹⁸ Moreover, Szustakiewicz¹⁷⁸ and Bagiński³⁵ reported that functionalizing the surface of different shapes of gold NPs with two specific ligands and mixing it with a liquid crystal matrix resulted in the creation of helical heterostructures showing immense chiral plasmonic response. However, all these works focused on plasmonic nanoparticles. The question of whether similar interactions between the thermotropic liquid crystal and gold nanoparticles could also helically assemble ultra-small gold nanoclusters and induce similar chiral properties was still open.

This chapter presents my research exploring this topic to answer if liquid-crystal template-driven helical assembly of gold nanocluster is possible and, if yes, what new properties can emerge. It is divided into four parts, describing the major steps in my research on that topic. The first part describes the synthesis and characterization, both optical and structural, of achiral Au₂₅(PET)₁₈ gold nanoclusters. The second part focuses on the properties of liquid-crystal template and its ability to form helical nanofilaments. The third part explores the functionalization of Au₂₅(PET)₁₈ gold nanoclusters with two ligands and their influence on the nanocluster optical properties as well as mixing with the template material. The last part shows the morphology and optical properties of the sample which formed helical nanofilaments coated with gold nanoclusters. It also presents the chiroptical properties of gold nanoclusters gained due to the helical assembly and discusses their possible origin.

Part of the results shown in this chapter have been published in Lipok, M.; Obstarczyk, P.; Parzyszek, S.; Wang, Y.; Bagiński, M.; Buergi, T.; Lewandowski, W.; Olesiak-Bańska, J. *Advanced Optical Materials* 2023, 11, (3), 2201984.

VIII. 1 Materials & methods

Materials

Toluene (HPLC grade), Methanol (HPLC grade), Tetrahydrofuran (HPLC grade), Dichloromethane (HPLC grade), Phenylethanethiol (98%), Sodium borohydride ($\geq 98\%$), Gold (III) chloride trihydrate ($\geq 99.9\%$), Tetra-n-octylammonium bromide (TOABr), Milli-Q® Type 1 Ultrapure water, 4-[(16-sulfanylhexadecanoyl)oxy]phenoxy-4-(hexadecyloxy)benzoate (L ligand), 1,3-phenylenebis[4-(4-oleyloxyphenyliminonetyl)benzoate] (oleylo-imino matrix, OIM), dodecanethiol (DDT ligand). L ligand, dodecanethiol and OIM were synthesized by Dr. Maciej Bagiński from the University of Warsaw. All other chemicals apart from water were bought from Sigma-Aldrich. Percentages in brackets indicate the purity of a given reagent.

Methods

Optical properties characterization: All absorption and fluorescence spectra presented in this chapter were measured with a JASCO V-670 spectrophotometer and Edinburgh Instruments FS5 spectrofluorometer, respectively. The concentration of all measured gold nanoclusters and OIM toluene solutions was 0.05 mg/ml. The dry samples, such as OIM helical nanofilaments, DF AuNC layer and DF AuNC HA, were prepared on microscope coverslips using the helical nanofilament formation protocol described further in the chapter. All fluorescence excitation spectra of gold nanoclusters were monitored at 840 nm and fluorescence emission spectra were excited at 450 nm. In case of the OIM template, the fluorescence excitation spectra were monitored at 550 nm and fluorescence emission spectra excited at 450 nm. The same samples, poured into 0.5 mL quartz cuvettes, were used in both fluorescence and absorption measurements.

Structural characterization: The MALDI-TOF mass spectra presented in this chapter were measured with a Bruker Autoflex spectrometer. The samples were measured in positive linear mode using the nitrogen laser and Trans-2-[3-(4-tert-Butylphenyl)-2-methyl-2-propenylidene]-malononitrile as a matrix. Before the measurements, 10 μL of each of the gold nanoclusters samples dissolved in toluene were mixed with the same volume of the matrix (concentration 35 mg/mL, toluene) and then 2 μL was drop-casted onto a MALDI plate and dried. SAXRD signal was collected in the transmission mode using the Bruker Nanostar with Cu $K\alpha$ radiation and Kapton foil substrate.

Morphology characterization: Two methods were used to characterize the samples described in this chapter: transmission electron microscopy (TEM) allowed to verify the interaction of gold nanoclusters with the liquid crystalline matrix meanwhile atomic force microscopy (AFM) confirmed their helical nature and twist direction on microscope slides, used further for measurements of chiroptical properties. For AFM imaging I have used Veeco Dimension V microscope in the tapping mode, with the SS probe mounted. TEM imaging was done with a JEM 1400 microscope at the Nencki Institute of Experimental Biology of the Polish Academy of Sciences.

Chiroptical properties characterization: Circularly polarized luminescence was measured using the home-built CPL microscope system described in detail in chapter VI.1. The CPL from

samples with AuNCs was collected with 800 nm longpass filter (FELH0800, Thorlabs) and for OIM measurements, the 800 nm longpass filter was changed to 550 nm (FELH0550, Thorlabs).

VIII. 2 Synthesis and characterization of achiral gold nanoclusters Au₂₅(PET)₁₈

VIII. 2.1 Synthesis and purification of Au₂₅(PET)₁₈

At the beginning, 1 g of gold salt and 1.64 g of TOABr were dissolved in a glass flask with 125 mL of tetrahydrofuran. Then, the solution was mixed for 1 h at 23°C using the magnetic stirrer and after this time, 1.62 mL of phenylethanethiol was added. When the solution lost all the colour and became transparent, 25 mL of 1M sodium borohydride dissolved in ice-cold water was fast-injected into the solution and left stirring for 48 h at 0°C. After two days, the dark-brown colour of the solution indicated the successful synthesis of Au₂₅(PET)₁₈. To purify the nanoclusters, the aqueous phase was separated from the organic phase using the glass separator funnel. The organic phase was gravity-filtered and evaporated to remove the remaining THF and dissolved in 20 mL of toluene. Then, inside the separatory funnel, nanoclusters were washed four times with MiliQ water to remove the left TOABr counter-ions. After the aqueous phase was cast out, the remaining organic phase was dried out in a rotary evaporator and the remaining residue was washed with methanol to clean excessive free thiols and different by-products of the process. Purified Au₂₅(PET)₁₈ nanoclusters were stored in the glass vial in the refrigerator at -18°C.

VIII. 2.2 Optical properties of Au₂₅(PET)₁₈

To prove that the synthesized gold nanoclusters possessed the reported optical properties of Au₂₅(PET)₁₈,¹³² I measured their optical properties such as absorption and fluorescence spectrum. The absorption spectrum of Au₂₅(PET)₁₈, denoted with a solid black line in Figure 22, presented three distinct bands at 400 nm, 450 nm and 688 nm. Both, the shape and location of the bands agreed well with the previous reports on Au₂₅(PET)₁₈ optical properties, confirming that the synthesis was successful.^{132, 199, 200} According to the literature, the band at 400 nm is connected with the intraband electronic transitions, the one at 450 nm with the mixed intraband and interband transitions and the last band located at 688 nm is connected with the transition from HOMO to LUMO.¹²² In case of excitation spectra, drawn with a dark grey dashed line in Figure 22, two bands could be recognized, one located at 440 nm and the second one at 580 nm. One of the most characteristic features of Au₂₅(PET)₁₈ gold nanoclusters is their NIR fluorescence emission. My experiments have confirmed that - the fluorescence emission maximum (Figure 22, dotted grey line) was located at 840 nm.

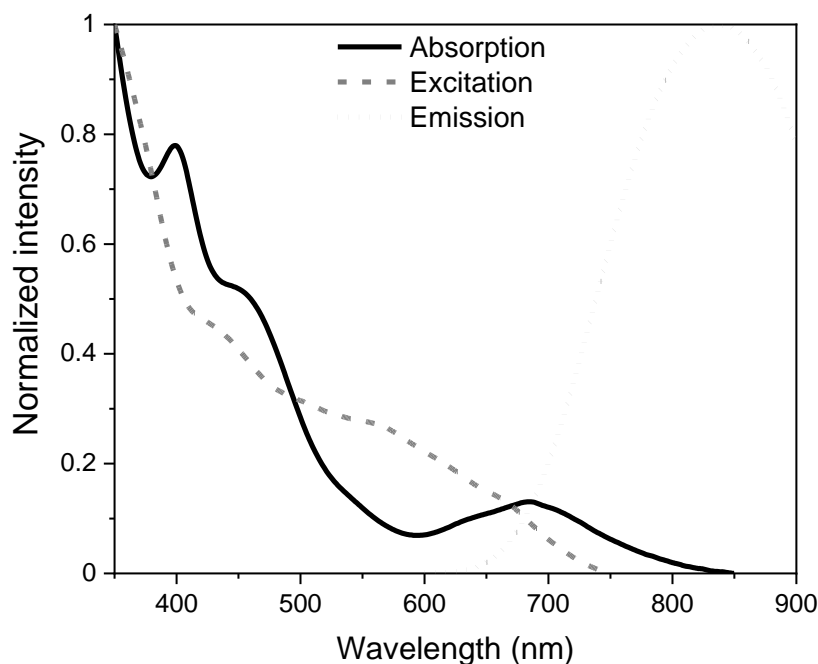


Figure 22. Normalized absorption, fluorescence excitation and emission spectra of $\text{Au}_{25}(\text{PET})_{18}$ gold nanoclusters. The absorption spectrum is denoted with a solid black line, the fluorescence excitation spectrum with a dark grey dashed line and the fluorescence emission spectrum with a bright grey dotted line. The fluorescence excitation spectrum was monitored at 800 nm and the fluorescence emission spectrum was excited at 450 nm.

VIII. 2.3 Structural properties of $\text{Au}_{25}(\text{PET})_{18}$

For the success of this research, it was also important that the structure of $\text{Au}_{25}(\text{PET})_{18}$ was already well understood. In order to better understand the interactions between the nanocluster and the chiral matrix, crucial to the formation of chiral heterostructures, it was important to first determine the structure of synthesized gold nanoclusters. $\text{Au}_{25}(\text{PET})_{18}$ nanoclusters are built of 13 gold atoms creating an icosahedral core and 6 staple-like motifs made of gold and sulphur atoms arranged in the pattern “SR–Au–SR–Au–SR”.²⁰¹ As can be seen in Figure 23, the Au_{25} nanocluster structure is made of four symmetrically connected layers. The first layer is the aforementioned nanocluster core (B), made of thirteen gold atoms. The second one (C) is made of twelve sulfur atoms arranged into another icosahedron. The third layer (D) is an irregular polyhedron made of gold atoms and the last layer (E) is a sulphur octahedron.

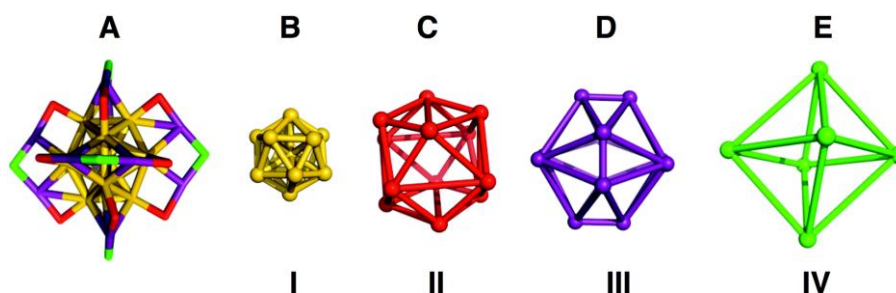


Figure 23. Crystal structure of $\text{Au}_{25}(\text{PET})_{18}$. Panel A shows the whole structure of $\text{Au}_{25}(\text{PET})_{18}$. Panels B – E show four symmetrically connected layers made of different atoms and building the nanocluster. Image reprinted from reference no.²⁰¹ under Creative Commons Attribution 3.0 Unported (CC BY) Licence.

To determine the structure of synthesised gold nanoclusters, MALDI-TOF mass spectra were measured (Figure 24a) by Dr. Yanan Wang and Prof. Thomas Buerger from the Department of Physical Chemistry at the University of Geneva (Switzerland). The strong peak at 7393 m/z confirmed the presence of $\text{Au}_{25}(\text{PET})_{18}$.²⁰² The MALDI experiment also caused the fragmentation of the studied nanocluster, resulting in the strong signal from $\text{Au}_{21}(\text{PET})_{14}$ with its peak located at 6057 m/z. This type of nanocluster is commonly created after $\text{Au}_4(\text{PET})_4$ are fragmented from $\text{Au}_{25}(\text{PET})_{18}$.²⁰² Meanwhile, the weak peaks at 7061 m/z, 6725 m/z and 6391 m/z, indicate the presence of intermediate sizes - $\text{Au}_{24}(\text{PET})_{17}$, $\text{Au}_{23}(\text{PET})_{16}$ and $\text{Au}_{22}(\text{PET})_{15}$, respectively.²⁰² Apart from the mass spectra also the size of synthesized gold nanoclusters was defined using small-angle X-ray diffraction (SAXRD), a technique often used to assess the size of various nanoparticles and nanoclusters.²⁰³ The measurements were carried out with the help of Dr. Sylwia Parzyszek and Prof. Wiktor Lewandowski from the University of Warsaw. The maximum of the band presented in Figure 24b was at the angle $2\theta \sim 5.73^\circ$ which corresponded to the nanocluster size around 1.5 nm, which fit well within the values reported for $\text{Au}_{25}(\text{PET})_{18}$.²⁰⁴

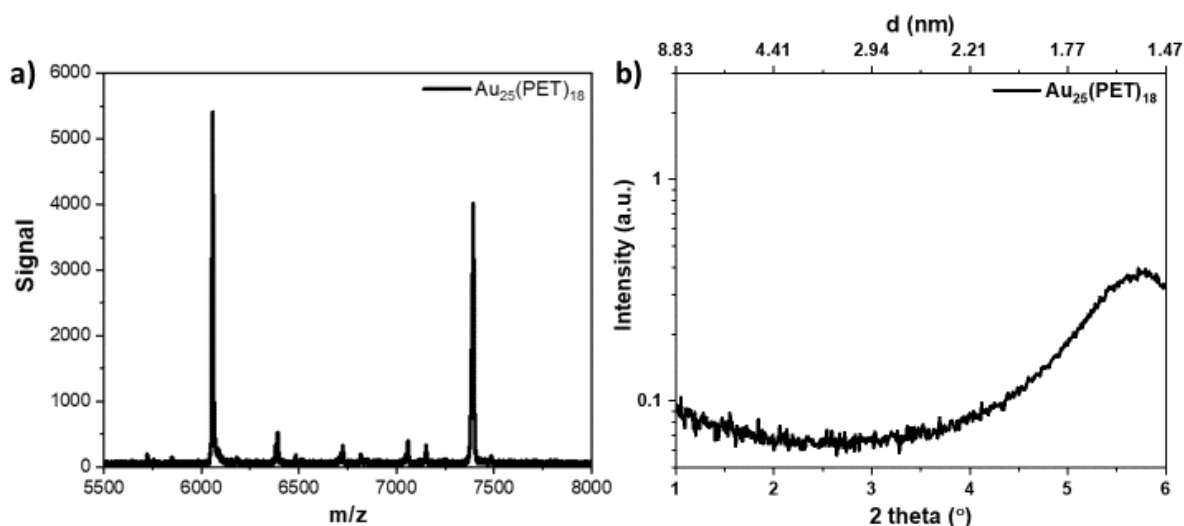


Figure 24. MALDI-TOF mass spectra (a) and SAXRD spectra (b) of $\text{Au}_{25}(\text{PET})_{18}$ gold nanoclusters.

VIII. 2.4 Thermal stability of $\text{Au}_{25}(\text{PET})_{18}$

As was stated in the introduction, gold nanoclusters often lose their stability in high temperatures,²⁰⁵ required to prepare liquid-crystalline helical nanofilaments.^{35, 178, 206} Thus, before preparing the chiral heterostructures, it was important to find the highest temperature that does not influence the nanocluster stability, and does not impair their optical properties. The thermal stability of $\text{Au}_{25}(\text{PET})_{18}$ was monitored via its absorption spectra after pre-heating the nanocluster solution to three temperatures: 30°C, 80°C and 130°C, as presented in Figure 25. Heating the solution to 30°C (Figure 25, black line) did not visibly affect the nanoclusters, and their spectrum resembled the one measured after their purification, shown in Figure 22. After pre-heating the solution to 80°C (Figure 25, red line) all three bands were slightly flattened, but still easily recognizable, confirming that the nanoclusters are stable. However, heating the solution to 130°C (Figure 25, green line), the temperature used for helical nanofilament formation in previous experiments with chiral heterostructures using a similar

matrix,^{35, 178, 206} caused serious nanocluster decomposition, since the bands at 450 nm and 700 nm were barely visible and the band located at 400 nm completely vanished. Based on these results, further experiments on chiral heterostructures were conducted at 80°C.

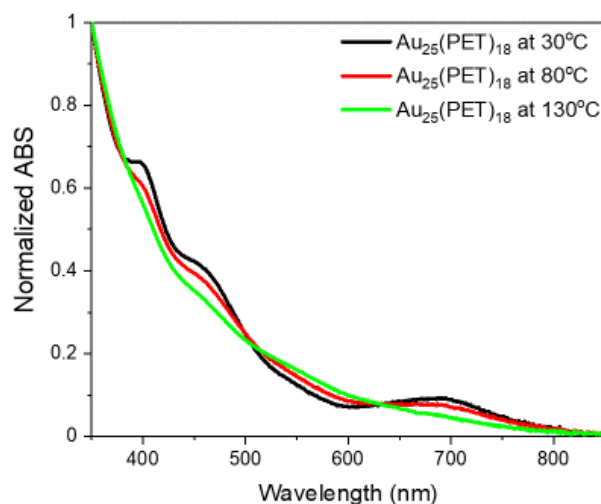


Figure 25. Absorption spectra of pre-heated $\text{Au}_{25}(\text{PET})_{18}$ gold nanoclusters.

VIII. 3 Liquid crystalline matrix characterization

VIII. 3.1 OIM - nature and structure

As was presented in the literature review of this dissertation, a vital part of creating chiral heterostructures is finding the correct template, that will interact with chosen nanomaterials and allow their control. I have chosen liquid crystalline material 1,3-phenylenebis[4-(4-olexyloxyphenyliminonetyl)benzoate] (oleylo-imino matrix, OIM), due to its similarity to matrices already used to create chiral heterostructures with plasmonic gold nanoparticles.^{35, 178} OIM was synthesized by Dr. Maciej Bagiński from the University of Warsaw. Its chemical structure is presented in Figure 26a. The bent-core geometry of this type of liquid-crystalline molecules allows them not only to create layered structures but also, due to internal layer frustration, form helical nanofilaments (HNF) of both handedness.^{207, 208} OIM is a thermotropic liquid crystalline material, meaning that it can transit between the isotropic and anisotropic phases with different properties after changing its temperature.²⁰⁹ In case of liquid crystalline materials similar to OIM, like dimeric L-L molecule reported by Bagiński *et al*,³⁵ helical nanofilaments are formed after firstly heating the molecule to 130°C, to their isotropic phase, and then slowly cooling them (3°C/min) to 30°C, to allow the orientation of molecules into helical nanofilaments phase.

VIII. 3.2 Helical nanofilaments preparation

In the previous parts, I have shown that $\text{Au}_{25}(\text{PET})_{18}$ gold nanoclusters are stable upon heating to 80°C. I needed to verify if the OIM matrix can form helical nanofilaments after heating to such temperatures, lower than reported 130°C. To check that, I modified the protocol used for chiral heterostructure assembly in a paper by Bagiński *et al*³⁵ and prepared two samples to assess the morphology of resulting helical nanofilaments, one at the TEM grid and the second one at the glass microscope slide. The protocol used for creating helical nanofilaments of OIM is shown in Figure 26b. First, 3 milligrams of OIM were dissolved in 1 mL of toluene. Then,

respectively, 10 μL and 100 μL of OIM solution were drop-casted on a TEM grid and microscope glass slide. Both substrates were heat annealed using the microscope heating stage with a controlled speed of $30^\circ\text{C}/\text{min}$ to 80°C and afterward, slowly ($3^\circ\text{C}/\text{min}$) cooled to 30°C . After that, the TEM grids with OIM were imaged using TEM (Figure 26c) and the microscope glass slides with OIM were imaged with AFM (Figure 26d). TEM (Figure 26b) showed that nanofilaments had a twisted ribbon geometry with a width around 30 nm and a helical pitch around 200 nm. AFM images (Figure 26c) determined that OIM molecules form long HNF aggregated into hierarchical structures. Both imaging methods confirmed that the modified procedure resulted in the formation of helical nanofilaments.



Figure 26. OIM structure and its helical nanofilaments. The chemical structure of OIM is shown in picture (a). The protocol leading to the formation of OIM helical nanofilaments is shown in picture (b). Pictures (c) and (d) present the helical morphology of OIM nanofilaments imaged using TEM (c) and AFM (d). Picture (c) is reprinted from reference no.²¹⁰ under the Creative Commons Attribution-NonCommercial-NoDerivatives 4.0 International (CC-BY-NC-ND) license.

VIII. 3.3 Optical and chiroptical properties of OIM

One of the main goals of this research was to check if chiral heterostructures with gold nanoclusters will cause them to exhibit chiral optical properties such as circularly polarized luminescence. However, it required first understanding the optical properties of OIM matrix to confirm in the later experiments, that the observed signal comes from the nanoclusters. First, I measured the absorption and fluorescence spectra of OIM solutions, presented in Figure 27a. The absorption spectrum was characterized by a single peak at 360 nm. OIM also possessed a single fluorescence excitation band with a maximum at 454 nm (Figure 27a, red line). Upon excitation at that wavelength, a broad fluorescence emission band was measured, with a maximum at 510 nm, slowly decreasing up to 700 nm (Figure 27a, blue line).

I measured the CPL from helical OIM nanofilaments, using the home-built 1P-CPL system described in chapter VI.1 with appropriate optical filters mounted, to collect the OIM luminescence. The luminescence exhibited by OIM nanofilaments was clearly observable (Figure 27b), After collecting left- and right-CPL from the sample, I calculated the luminescence dissymmetry factors, using the formula (equation 7) presented in chapter II.5. As can be observed in Figure 27c, g_{lum} values of OIM helical nanofilaments were of the order of 10^{-1} which meant they not only showed chirality in their morphology but were also characterized by a strong chiral emission.

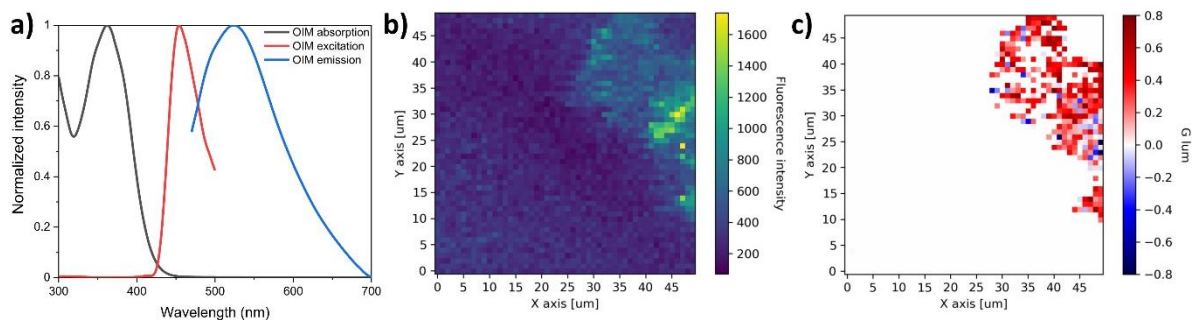


Figure 27. Optical properties of OIM. Normalized absorption (black line), fluorescence excitation (red line) and fluorescence emission (blue line) spectra of OIM, measured from 3mg/mL toluene solution, are shown in the picture (a). CPL signal from OIM nanofilaments (b) and g_{lum} calculated from this signal (c). Spectra shown in (a) were measured from toluene OIM solution meanwhile (b) and (c) from the glass slide with OIM helical nanofilaments. Pictures (b) and (c) are reprinted from reference no.²¹⁰ under the Creative Commons Attribution-NonCommercial-NoDerivatives 4.0 International (CC-BY-NC-ND) license.

VIII. 4 Nanocluster functionalization and chiral heterostructure preparation

VIII. 4.1 Functionalization of $Au_{25}(PET)_{18}$

Previous reports on creating chiral heterostructures made of HNFs and plasmonic nanoparticles showed, that nanoparticle surfaces need to be functionalized with specifically designed ligands to ensure compatibility with the organic template.^{35, 178, 206} For my experiments, I have chosen dodecanethiol (DDT, Figure 28a), one of the ligands used in those reports, and liquid crystalline ligand derived from the OIM template: 4-[(16-sulfanylhexadecanoyl)oxy]phenoxy-4-(hexadecyloxy)benzoate (L, Figure 28b) and synthesized by Dr. Maciej Bagiński from the University of Warsaw. Moreover, the works cited on this topic indicated that the best compatibility between the organic template and NPs was observed when the NP surface was double-functionalized with both ligands.³⁵ For this reason, before creating the chiral heterostructures, I tested how each of the ligands influenced both AuNCs optical properties and interaction with the OIM template. I prepared three samples: $Au_{25}(PET)_{18}$ functionalized with DDT ligand (further referred to as AuNC + DDT), $Au_{25}(PET)_{18}$ functionalized with L ligand (further referred to as AuNC + L) and $Au_{25}(PET)_{18}$ double-functionalized with both DDT and L (further referred to as DF AuNC).

The functionalization started with dissolving both $Au_{25}(PET)_{18}$ (1 mg/mL), DDT (10 mM) and L (12 mg/mL) in toluene. In the first sample, $Au_{25}(PET)_{18}$ was mixed with DDT to the final molar concentration of DDT equal to 0.4 μ M. In the second one, $Au_{25}(PET)_{18}$ was mixed with L to the final molar concentration of L ligand equal to 0.27 μ M. In the last one, $Au_{25}(PET)_{18}$ was mixed with both DDT and L ligands to their final molar concentration of 0.13

μM . Then, solutions were poured into Eppendorf 1.5 mL tubes and stirred at 1200 rpm for 12h at 23°C in Eppendorf ThermoMixer. After that, all three solutions were purified using column chromatography with a silica substrate to obtain functionalized nanoclusters with no impurities. Samples were dried and stored at -5°C .

MALDI-TOF mass spectra (Figure 28c-e) were measured to confirm that AuNCs were successfully functionalized with both ligands. First of all, the peak at 7393 m/z, visible in spectra from all three samples, confirmed the presence of $\text{Au}_{25}(\text{PET})_{18}$. In the mass spectra of DDT functionalized AuNCs (Figure 28c) one could recognize two peaks (denoted with x) corresponding to $\text{Au}_{25}(\text{PET})_{17}\text{DDT}_1$ and $\text{Au}_{25}(\text{PET})_{16}\text{DDT}_2$, confirming the exchange of PET ligands into DDT. The peaks of L-coated nanoclusters (Figure 28d) were located above 8000 m/z due to the higher ligand mass. The peak at 8619.7 m/z and marked with * at the Figure X7d inset, corresponded to the $\text{Au}_{25}(\text{PET})_{16}(\text{L})_2$ nanocluster. In the case of DF AuNCs (Figure 28e), two peaks corresponded to the calculated mass of double functionalized AuNC: $\text{Au}_{25}(\text{PET})_{16}(\text{DDT})_1(\text{L})_1$ at 8073 m/z and $\text{Au}_{25}(\text{PET})_{15}(\text{DDT})_2(\text{L})_1$ at 8135 m/z. Moreover, in the same sample there were also peaks characteristic to nanoclusters functionalized with a single ligand, such as those marked with *, located around 7500 m/z similar to the DDT functionalized nanoclusters. Taking all of that into account, the mass spectra have not only proven the stability of $\text{Au}_{25}(\text{PET})_{18}$ during the functionalization but also confirmed that both single- and double-functionalization of AuNC with DDT and L ligands were successful.

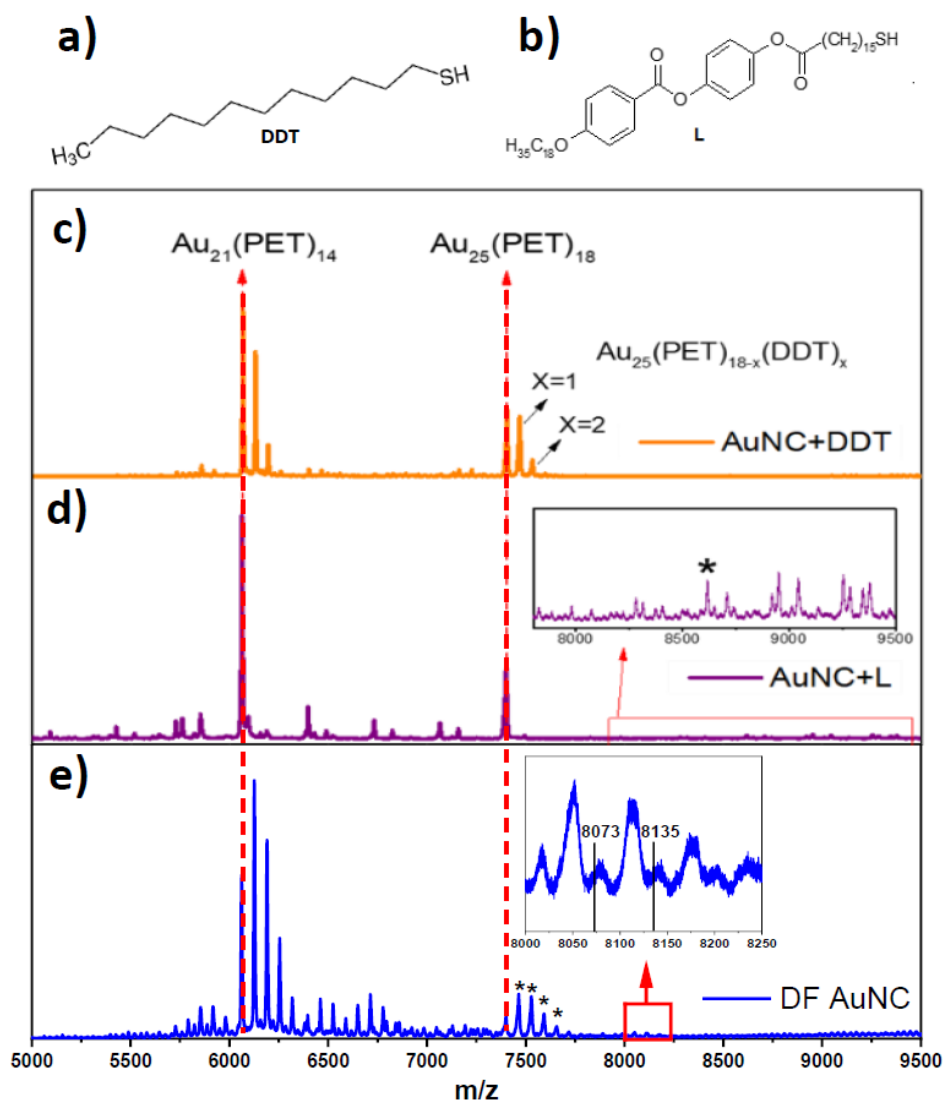


Figure 28. Chemical structure of DDT and L ligands with mass spectra of nanoclusters after their addition. Chemical structure of DDT (a) and L (b) ligands. MALDI-TOF mass spectra of $Au_{25}(PET)_{18}$ gold nanocluster after functionalization with DDT (c), L (d) and DDT+L (e). Images (b) – (e) are reprinted from reference no.²¹⁰ under the Creative Commons Attribution-NonCommercial-NoDerivatives 4.0 International (CC-BY-NC-ND) license.

VIII. 4.2 Optical properties of functionalized $Au_{25}(PET)_{18}$

After confirming the successful functionalization of $Au_{25}(PET)_{18}$, I checked how it influenced the nanocluster's optical properties by measuring their absorption (Figure 29a), fluorescence excitation (Figure 29b) and fluorescence emission (Figure 29c) spectra. Characteristic $Au_{25}(PET)_{18}$ peaks were visible in the absorption spectra of all three surface-functionalized samples, proving the optical stability of the studied nanocluster. The observable flattening of the bands could be attributed to the increasing heterogeneity of samples after the functionalization, as shown by multiple additional peaks visible in their MALDI-TOF spectra (Figure 28) as well as lower nanoclusters symmetry due to the addition of longer ligands (DDT and L are longer than PET). However, there were some observable band shifts in fluorescence excitation and emission spectra. In all three functionalized samples, the excitation peak at 450 nm shifted to 525 nm, and the one at 600 nm shifted to 675 nm, 680 nm and 690 nm, for

AuNC+DDT, AuNC+L and DF AuNC, respectively. In case of fluorescence emission spectra, all three bands red-shifted for about 10 nm, to 850 nm. This red-shift could be explained by the strengthened electron transfer from coating ligands to the nanocluster kernel caused by exchanging the original ligands (PET) with longer ones (DDT, L).²¹¹

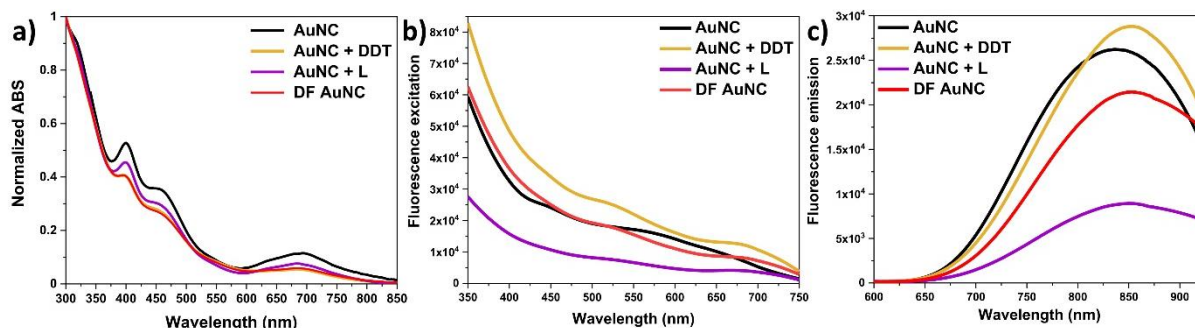


Figure 29. Optical properties of Au₂₅(PET)₁₈ gold nanocluster after surface functionalization. Normalized absorption (a), fluorescence excitation (b) and fluorescence emission (c) spectra of Au₂₅(PET)₁₈ after functionalisation with DDT, L and both ligands. Image (c) is reprinted from reference no.²¹⁰ under the Creative Commons Attribution-NonCommercial-NoDerivatives 4.0 International (CC-BY-NC-ND) license.

VIII. 4.3 Interaction with the liquid crystal template

After confirming that the optical properties of Au₂₅(PET)₁₈ nanoclusters are stable after both single and double functionalization, the next step focused on preparing the chiral heterostructures with all four studied types of nanoclusters to check, under what conditions they mix with OIM molecules the most effectively. All structures were prepared according to the protocol shown in Figure 26. First, 3 μ L of 1 mg/mL toluene solutions of all four nanocluster types were mixed with 1 μ L of 3 mg/mL OIM toluene solution, then dropcasted on TEM grids, heated to 80°C and slowly cooled to 30°C. TEM images of all four samples after the helical nanofilament formation are shown in Figure 30. Au₂₅(PET)₁₈ nanoclusters (Figure 30, AuNC) showed no interaction with the hosting matrix since they assembled into separate conglomerates laying on top of it. Nanoclusters functionalized with DDT (Figure 30, AuNC + DDT) showed greater interaction with OIM since they formed anisotropic assemblies following the template curvature. On the other hand, L functionalized nanoclusters (Figure 30, AuNC + L) coated some edges of helical nanofilaments, showing that this ligand is crucial for efficient nanocluster-host interdigitation. Finally, double-functionalized nanoclusters (Figure 30, DF AuNC) fully coated all of the imaged helical nanofilaments, with no sign of any spare anisotropic assemblies around. Moreover, the nanofilaments seemed to assemble into bigger domains, a few micrometers wide. The experiment has proven that the double-functionalization of the nanocluster surface led to the best interaction of studied gold nanoclusters with the OIM matrix, similar to conclusions drawn from the experiments with plasmonic nanoparticles.^{35, 178}

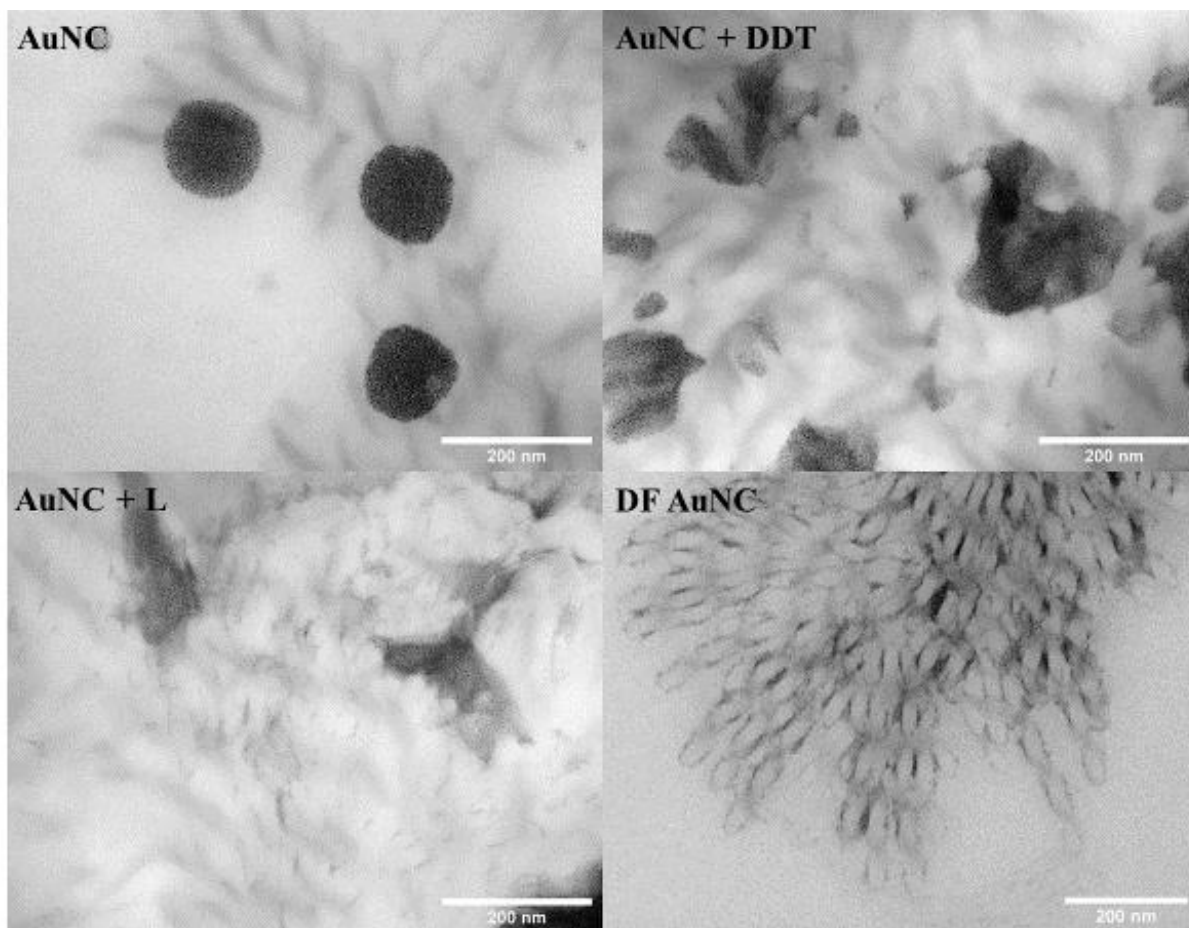


Figure 30. Morphology of chiral heterostructures created by mixing OIM template with all four types of studied gold nanoclusters. Images of AuNC, AuNC + DDT and AuNC +L are reprinted from reference no.²¹⁰ under the Creative Commons Attribution-NonCommercial-NoDerivatives 4.0 International (CC-BY-NC-ND) license.

VIII. 4.4 Chiroptical properties of functionalized gold nanoclusters

Before measuring the optical properties of chiral heterostructures, I tested the chiroptical properties of $\text{Au}_{25}(\text{PET})_{18}$ nanoclusters before (Figure 31a-c) and after (Figure 31d-e) the double-functionalization to check if the functionalization endowed them with chirality. Similarly to OIM helical nanofilaments, I measured their ability to generate circularly polarized luminescence using the system described in chapter VI.1. As could be seen from their 2D fluorescence intensity maps, there were no noticeable differences between the intensity of left-handed CPL and right-handed CPL, both for AuNC (Figure 31a, b) and DF AuNC (Figure 31d, e). It led to luminescence dissymmetry factor values oscillating around 0 (AuNC, Figure 31c, DF AuNC Figure 31f). However, there was an observable increase in non-zero g_{lum} values in maps of DF AuNC. Since such differences could be caused by fluctuations in nanocluster solutions, I also calculated the average luminescence dissymmetry factors from both maps. It was equal to $3.71 \pm 3.42 * 10^{-5}$ for AuNC and $4.74 \pm 3.79 * 10^{-3}$ for DF AuNC. $\text{Au}_{25}(\text{PET})_{18}$ are achiral nanoclusters,^{186, 212} so the g_{lum} of magnitude 10^{-5} could be ascribed to the CPL system detection limit. However, the two-order of magnitude increase in DF AuNC g_{lum} values could indicate some level of chirality, gained due to double-functionalization.

However, verifying that require in-depth theoretical studies on how both ligands influence the nanocluster's structure, which is beyond the scope of this work.

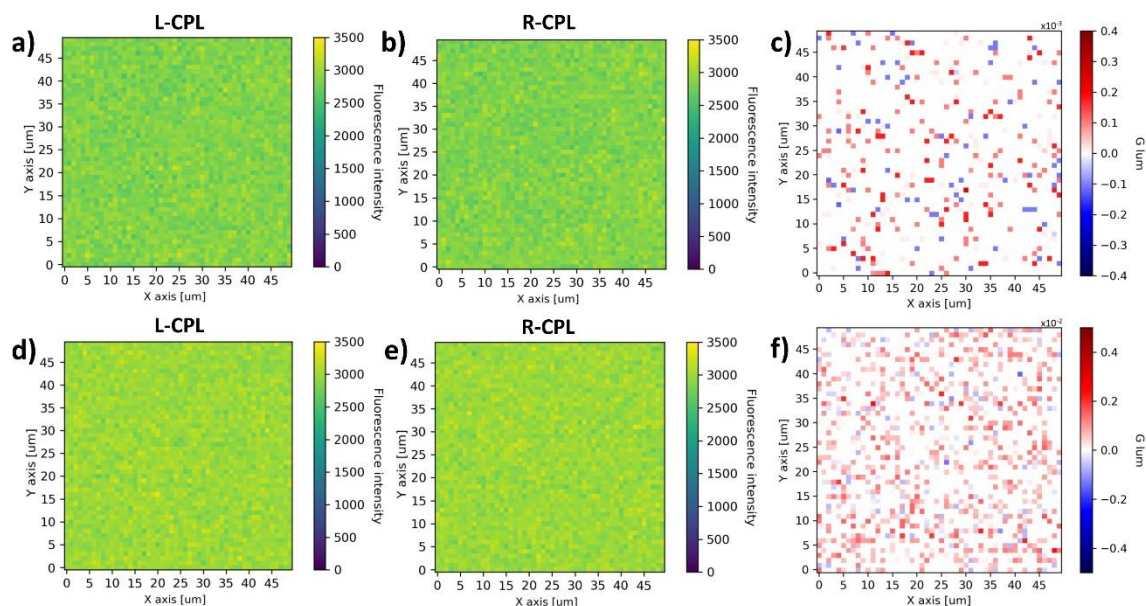


Figure 31. 2D maps showing circularly polarized luminescence and luminescence dissymmetry factors of AuNC and DF AuNC. The maps shows L-CPL (a, d) and R-CPL (b, e) of both AuNC(a, b) and DF AuNC (d, e). Pictures c and f present the maps of luminescence dissymmetry factors calculated from AuNC (order of magnitude 10^{-3}) and DF AuNC (order of magnitude 10^{-2}), respectively. Images a, c, d and f are reprinted from reference no.²¹⁰ under the Creative Commons Attribution-NonCommercial-NoDerivatives 4.0 International (CC-BY-NC-ND) license.

VIII. 5 Results & discussion

VIII. 5.1 Morphology of chiral heterostructures with gold nanoclusters

Before measuring the optical properties of chiral heterostructures with gold nanoclusters, I checked their morphology using AFM. The samples were prepared using the same protocol as TEM grids, imaged in Figure 30. As shown in Figure 32, the OIM matrix not only formed nanofilaments with visible helical twists but also created domains built of nanofilaments with different handedness. The counter-clockwise twist visible in Figure 32a corresponded to left-handed nanofilaments and the clockwise twist shown in Figure 32b, to right-handed nanofilaments. Moreover, the average HNF width was equal to 38 ± 8 nm and the average helical pitch was 153 ± 44 nm.

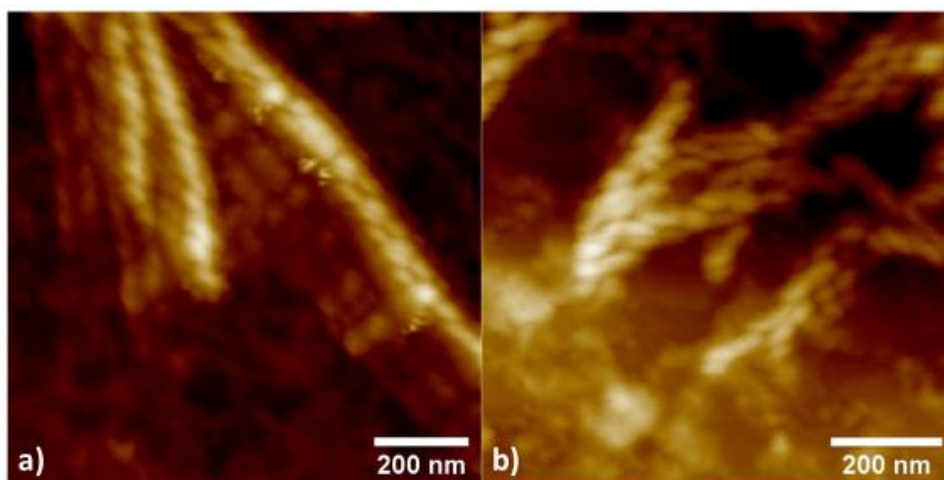


Figure 32. Morphology of helical nanofilaments coated with double-functionalized $\text{Au}_{25}(\text{PET})_{18}$. AFM Images (a) and (b) present left-handed and right-handed helical nanofilaments, respectively. Images are reprinted from reference no.²¹⁰ under the Creative Commons Attribution-NonCommercial-NoDerivatives 4.0 International (CC-BY-NC-ND) license.

VIII. 5.2 Optical properties of chiral heterostructures

I started measuring the optical properties of chiral heterostructures made of DF AuNC and OIM chiral template from measuring their absorption, fluorescence excitation and fluorescence emission spectra. Along the sample with HNF (DF AuNC HA), I also measured the properties of a dry layer of DF AuNC (DF AuNC Layer) prepared following the same protocol as helical nanofilaments, but without the addition of an OIM template, to monitor how the heating/cooling cycle influences the properties of double-functionalized nanoclusters.

The absorption spectra of both samples submitted to the heating/cooling cycle (Figure 33a, blue and green line) showed that they have kept some of the characteristic features of non-heated $\text{Au}_{25}(\text{PET})_{18}$ nanoclusters before and after the double-functionalization (Figure 33a, black and red lines): the bands at 450 nm and 700 nm were still clearly visible. The band at 400 nm was visible only in the sample without helical nanofilaments, since OIM molecules strongly absorb in the range below 400 nm (Figure 27a), probably covering the nanocluster band.

The excitation spectrum of DF AuNC layer (Figure 33b, blue line) resembled the one from the solution of double-functionalized nanoclusters (Figure 33b, red line) with the same bands visible in both. In the spectrum of helical assemblies with DF AuNCs (Figure 33b, green line), one can also recognize two bands localized at 675 nm and 575 nm, characteristic to a double-functionalized sample. However, there was also a new band at 400 nm, which could not be attributed to DF AuNC, nor OIM template (Figure 27a). Thus, its origin could be the helical assembly of $\text{Au}_{25}(\text{PET})_{18}$.

The fluorescence emission spectra (Figure 33c) of both dry samples were strongly red-shifted. From 850 nm reported for DF AuNC to the wavelength above 925 nm, beyond the spectral range of the detector used (Hamamatsu R928P). Valenta *et al* reported that the emission band of $\text{Au}_{25}(\text{PET})_{18}$ nanoclusters should not shift upon heating 80°C.²¹³ However, as was shown in my paper, it could be explained by the increased electronic coupling between the neighbouring gold nanoclusters.²¹⁰ Based on the TEM images, I found out that inside those two

samples, gold nanoclusters formed close-packed assemblies with the intercluster distance equal to 3.58 ± 0.54 nm for the DF AuNC layer and 3.24 ± 0.55 nm for DF AuNC HA. Huang *et al* reported, that 6.21 ± 1.14 nm intercluster distance is enough for effective electronic coupling between the nanoclusters.¹⁴⁴ Thus, the distance between nanoclusters in both samples explored in my studies was sufficient for electronic coupling to occur.

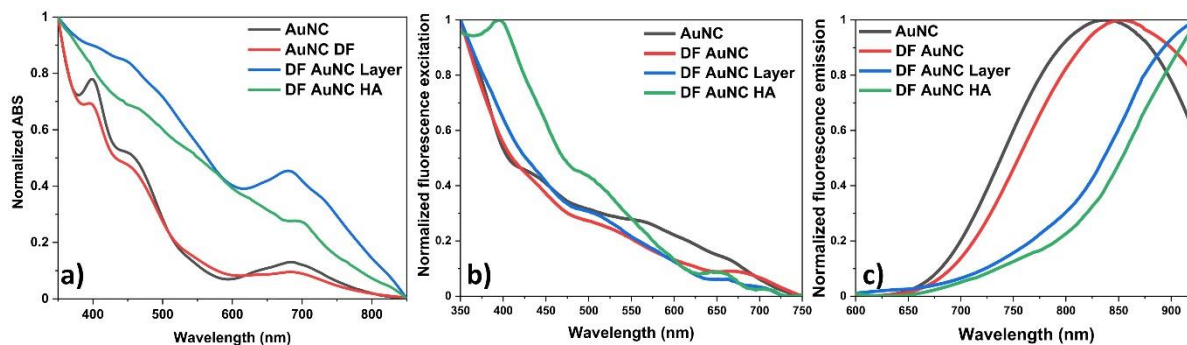


Figure 33. Morphology of helical nanofilaments coated with double-functionalized Au₂₅(PET)₁₈. Images taken using TEM (a, b) and AFM (c, d). Images (c) and (d) present left-handed and right-handed helical nanofilaments, respectively. Images (a) and (c) are reprinted from reference no.²¹⁰ under the Creative Commons Attribution-NonCommercial-NoDerivatives 4.0 International (CC-BY-NC-ND) license.

VIII. 5.3 Chiroptical properties of chiral heterostructures

In the end, I measured the circularly polarized luminescence (Figure 34) from the chiral heterostructure made of a double-functionalized AuNC and OIM template (DF AuNC HA). Comparing the 2D maps of L-CPL (Figure 34a) and R-CPL (Figure 34b), one could notice that depending on the location, the sample exhibited stronger positive or negative circularly polarized luminescence. Calculating the luminescence dissymmetry factors (Figure 34c) revealed that observed CPL signals originate from two micrometre-size domains of opposite chirality, possibly created from the helical nanofilaments of similar twist, like those shown in Figure 31. Interestingly, the research on chiral absorption of HNF coated with plasmonic nanoparticles reported similar domains.¹⁷⁸ Both domains observed in DF AuNC HA were characterized by very high g_{lum} values, reaching +0.32 and -0.37 for left and right CPL, respectively. The highest values ever reported for helically assembled gold nanoclusters. As was discussed in the theoretical section of this dissertation, chiral gold nanoclusters are often characterized with g_{lum} values of order 10^{-3} and, until my research, the only nanocluster samples with g_{lum} of order 10^{-1} were helical superstructures such as chiral photonic cellulose gold nanocluster films.⁶⁷ This experiment has shown, that template-assisted helical assembly of gold nanoclusters using liquid-crystal templates can result in chiral heterostructures with strongly chiral luminescence. A new type of circularly polarized light emitter in the NIR range of wavelengths.

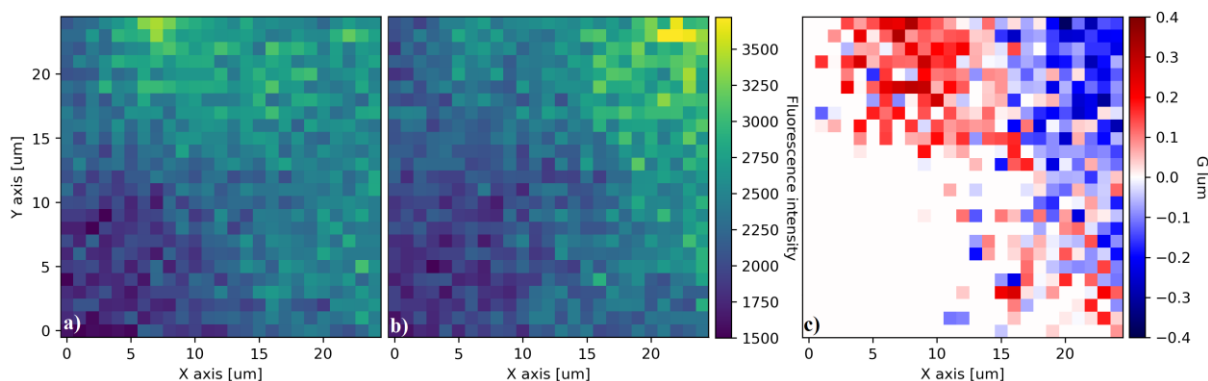


Figure 34. 2D maps showing circularly polarized luminescence and luminescence dissymmetry factors of DF AuNC HA. L-CPL and R-CPL are presented in images (a) and (b), respectively. Luminescence dissymmetry factors are shown in image c. Images are reprinted from reference no.²¹⁰ under the Creative Commons Attribution-NonCommercial-NoDerivatives 4.0 International (CC-BY-NC-ND) license.

The question opened - since gold nanoclusters $\text{Au}_{25}(\text{PET})_{18}$ are achiral nanomaterials, what exactly caused the strong circularly polarized luminescence shown in Figure 34? TEM images of studied chiral heterostructures (Figure 30) showed that they are made of liquid-crystalline helical nanofilaments coated with gold nanoclusters. As shown in Figure 27c, HNF also emit circularly polarized luminescence leading to high luminescence dissymmetry factors of the same order of magnitude as chiral heterostructures with nanoclusters, but their luminescence (Figure 27a) is located in the range of wavelengths from 500 nm to 700 nm. The CPL of chiral heterostructures was measured using optical filters cutting off any signal below 800 nm, since the emission maximum of $\text{Au}_{25}(\text{PET})_{18}$ was located at 840 nm and, for DF AuNC HA, even above 900 nm (Figure 32c). Thus, the CPL signal shown in Figure 34 must come from the gold nanoclusters, which obtained the chirality due to chirality transfer from helical nanofilaments. Similar behaviour, but connected to the absorption properties of nanoparticles, was reported by Szustakiewicz *et al.*¹⁷⁸ Their work showed, that achiral plasmonic gold nanoparticles start exhibiting strong circular dichroism upon helical assembly using the liquid-crystalline template. Moreover, the reported nanoparticles gained chirality correlated to the local chirality of helical nanofilaments, similar to the samples I examined. Thus, my research proved that this type of template-driven helical assembly could not only be used to induce chiroptical properties in plasmonic nanoparticles but also in ultra-small gold nanoclusters.

VIII. 6 Conclusions

This chapter presented my research concerning the preparation and characterization of chiral heterostructures of gold nanoclusters made using the liquid-crystalline template helical assembly method. I described how the $\text{Au}_{25}(\text{PET})_{18}$ nanoclusters were synthesized and purified and confirmed it by measuring their optical properties and mass spectra. I checked that they are stable in temperatures needed for helical nanofilament assembly. I have shown that liquid-crystalline material OIM can create helical nanofilaments, which has been proven by both TEM and AFM imaging. Moreover, I verified that OIM HNF emits strong circularly polarized luminescence with dissymmetry factors of the order of 10^{-1} . Then, I presented the nanocluster surface functionalization process and mass spectra confirming that the surface $\text{Au}_{25}(\text{PET})_{18}$ gold nanoclusters has been successfully functionalized with both DDT and L ligands. Moreover, I explored how each of the ligands influences the optical properties of gold nanoclusters. I also measured the CPL of $\text{Au}_{25}(\text{PET})_{18}$ before and after double-functionalization and determined that their average g_{lum} values are of order 10^{-5} and 10^{-3} , respectively. Additionally, experiments with creating chiral heterostructures with gold nanoclusters with both single and double ligand coating have shown, that double-functionalization of $\text{Au}_{25}(\text{PET})_{18}$ with DDT and L ligands leads to the most efficient mixing with OIM template and, as a result, the best helical assembly of gold nanoclusters. Then, I analysed the morphology of those helical assemblies using both TEM and AFM imaging to determine the average size of helical nanofilaments as well as their hierarchical structure and tendency to create bigger, few μm large, domains. Furthermore, I explored how solvent evaporation and helical assembly influence the optical properties of gold nanoclusters and determined that it causes a strong red-shift in fluorescence emission, due to electronic coupling of neighbouring gold nanoclusters. In the end, I measured the circularly polarized luminescence exhibited by chiral heterostructures made of OIM and DF AuNC. The measurements have not only revealed that the sample was built of oppositely chiral domains but most importantly, that the helical assembly of gold nanocluster transfers the chirality from domains to nanoclusters, which was confirmed by their high luminescence dissymmetry factors equal to $+0.32$ and -0.37 . All of that has confirmed that achiral gold nanoclusters could obtain chiral optical properties upon binding to helical nanofilaments.

IX. Optical properties of chiral heterostructures with anisotropic plasmonic gold nanoparticles

Hypothesis: *The chirality can be transferred from the chiral protein matrix to single achiral gold nanoparticles upon binding them to the matrix*

Plasmonic nanoparticles are model materials for local detection of chirality due to their high sensitivity to environmental factors, which could influence the position of their localized surface plasmon resonance.²¹⁴ There are already reports showing their ability to detect the chirality of peptides¹⁰² or proteins⁵². It is often realized by the detection of new emerging circular dichroism located at the wavelength range corresponding to the LSPR of NPs. However, only a few reports show the induction of circular dichroism in chiral heterostructures where plasmonic nanoparticles are bound to protein aggregates, such as amyloid fibrils. As shown by Kumar *et al.*,²¹⁵ under such conditions, the chiral plasmonic effects are induced due to plasmon-coupling between the helically arranged anisotropic nanoparticles. However, it has not yet been reported if it is possible to transfer the chirality from amyloids to gold nanoparticles without their helical arrangement.

In this chapter, I will present my experiments leading to the creation and optical characterization of chiral heterostructures made of bovine insulin amyloids, acting as a chiral matrix, and two types of gold nanoparticles – gold nanobipyramids and gold nanorods. The first part describes how the gold nanobipyramids were synthesized and show their optical and chiroptical properties. The second part focuses on the chiral matrix – I describe in detail the preparation of insulin amyloids, their chiroptical properties and morphology. The third part describes the preparation of chiral heterostructures and explores how different factors influence their new chiroptical properties. The fourth part presents how new chiral effects depend on the chiral matrix and explores their origin. The last part describes the preparation of chiral heterostructures with gold nanorods and their optical properties.

Results shown in this chapter were published as a part of my two papers:

- M. Lipok, P. Obstarczyk, A. Żak, and J. Olesiak-Bańska, *Single Gold Nanobipyramids Sensing the Chirality of Amyloids*, J. Phys. Chem. Lett. 14, 49, 11084–11091 (2023)
- S. Chattopadhyay, M. Lipok, Z. J. Pfaffenberger, J. Olesiak-Bańska, J. S. Biteen, *Single-Particle Photoluminescence Measures a Heterogeneous Distribution of Differential Circular Absorbance of Gold Nanoparticle Aggregates near Constricted Thioflavin T Molecules*, J. Phys. Chem. Lett. 15, 1618-1622. (2024)

IX. 1 Materials & methods

Materials

Ascorbic acid (>99%), citric acid (>99.9%), hydrochloric acid (12.17 M), gold (III) chloride trihydrate (>99.99%), hexadecyltrimethylammonium bromide (>99.0%), hexadecyltrimethylammonium chloride (>95%), insulin from bovine pancreas (>25 USP units per mg), silver nitrate (>99%), sodium borohydride (>99.9%), thioflavin-T (>65%), Milli-Q® Type 1 Ultrapure water. All chemicals apart from water were bought from Sigma-Aldrich. Percentages in brackets indicate the purity of a given reagent.

Methods

Morphology measurements:

The morphology of insulin protein aggregates was imaged using Atomic Force Microscopy with a Veeco Dimension V microscope working in the tapping mode, with the mounted super-sharp probe. All measured samples were prepared on a mica substrate. First, they were diluted to a concentration of 0.01 mg/mL then 20 μ L of each of the solutions was drop casted on a mica substrate and dried.

The morphology of gold nanoparticles and chiral heterostructures was imaged using Transmission Electron Microscopy using a Hitachi H-800 microscope at a voltage of 150 kV by Dr. Andrzej Źak. All samples were prepared by drop casting 3 μ L of each solution with chiral heterostructures on a TEM grid (200 mesh carbon on a copper film) and then air drying for 24 hours at room temperature.

Optical properties measurements:

All extinction and circular dichroism spectra were measured with a Jasco J-1500 spectropolarimeter in a standard 0.5 mL quartz cuvette. All spectra presented include a reference in the form of an aqueous buffer, appropriate for each sample measured. Each spectrum is an averaged signal from three scans over the chosen range of wavelengths.

Structure measurements:

The structural analysis of protein aggregates is based on data measured with a Vertex 60v spectrometer using Fourier-transform infrared (FT-IR) spectroscopy with attenuated total reflectance (ATR) sampling. All spectra were measured with a resolution of 4 cm^{-1} in the range from 4000 cm^{-1} to 400 cm^{-1} . Each presented spectrum is an average signal from 64 scans. The signal of each of the second derivatives was calculated and analysed using the multiple peak fit function in the OriginPro software.

IX. 2 Optical properties of gold nanobipyramids

For my studies on the optical properties of chiral heterostructures with plasmonic nanoparticles, I have chosen gold nanobipyramids (BPs), one of the types of anisotropic gold nanoparticles. Anisotropic gold nanoparticles, such as gold nanobipyramids or gold nanorods (NRs), offer highly controllable surface plasmon resonance which could be tuned from the visible range to NIR, by modifying nanoparticle's size and aspect ratio.²¹⁶ Moreover, as was discussed in the literature part of this dissertation, studies focused on chiral heterostructures with gold nanorods, have already shown, that they can gain chiral optical properties via chiral assembly of NRs^{46, 217} or enhancement of the local chirality as nanoantennas²¹⁸. BPs are an interesting nanomaterial from the perspective of chirality sensing, due to their ability to enhance electric field near their sharp tips.^{219, 220} Deska *et al* have reported, that dimers of gold nanobipyramids, also gain strong chiroptical properties upon specific mutual orientation, proving that this type of nanoparticles could potentially be used as a biosensor based on BPs aggregation.²²¹ Zhao *et al* have shown that BPs co-assembled with chiral cellulose photonic crystals result in the CD plasmonic response due to plasmonic-photonic coupling.¹⁶ Also Dong *et al* reported that BP dimers assembled via DNA-directed assembly result in stronger chiroptical response than gold nanorods.²⁴

Gold nanobipyramids were synthesized according to seed-growth protocol reported by Sánchez-Iglesias *et al*.²²² The seed solution was composed of 3.5 mL of MiliQ water, 5 mL 0.1 M hexadecyltrimethylammonium chloride (CTAC), 0.025 mL 0.025 M citric acid and 0.025 mL of 0.1M gold (III) chloride trihydrate, put in a 20 mL glass scintillation vial vigorously stirring above the magnetic mixer. Then, 0.25 mL of 0.025 M ice-cold sodium borohydride solution was fast injected into the stirring solution. After the solution changed colour from yellow to brown, it was heated during the 1.5 h water bath at 80°C, until it turned red. The growth solution was prepared by mixing 100 mL of 0.1 M hexadecyltrimethylammonium bromide with 5 mL of 0.01 M gold (III) chloride trihydrate, 2mL of 1M hydrochloric acid, 1mL of 0.01 M silver nitrate, and 0.8mL of 0.1 M ascorbic acid. After that, 5 mL of seed solution was added to the growth solution and incubated at 30°C for 8h. To purify the nanobipyramids after the synthesis, similarly to nanorods, the solution was centrifuged two times (6500 RCF) and, the pellet obtained after the second centrifugation was filled with a neutral pH buffer composed of MiliQ water and 0.1 mM CTAB.

After the synthesis and purification of plasmonic nanoparticles, I measured their optical and chiroptical properties. Their extinction spectra (Figure 35a, black line) were characterized by two bands, the first one located at 524 nm, corresponding to transverse LSPR, and the second one located at 622 nm, connected to longitudinal LSPR. The measured spectrum confirmed that nanoparticles were synthesized correctly, resulting in extinction comparable to the ones reported by Sanchez-Iglesias²²². The circular dichroism spectra of BPs (Figure 35a, red line) oscillated ~ 0 mdeg in the whole measured range from 400 nm to 800 nm. Thus, the experiment confirmed that nanoparticles were optically achiral, excluding the presence of chiral dimers or bigger aggregates in the sample.

In the end, I determined the size and morphology of synthesized nanoparticles using transmission electron microscopy (Figure 35b). The average length of BPs was equal to 23.1

nm and the average width to 11.1 nm, leading to an aspect ratio of ~ 2.1 . Moreover, nanoparticles were separated from each other and no nanoparticle aggregates, such as dimers or trimers, were observed. Thus, both CD spectrum and TEM imaging have confirmed that synthesized BPs are optically achiral and without any dimers that could induce the potential chiroptical properties without outside factors.

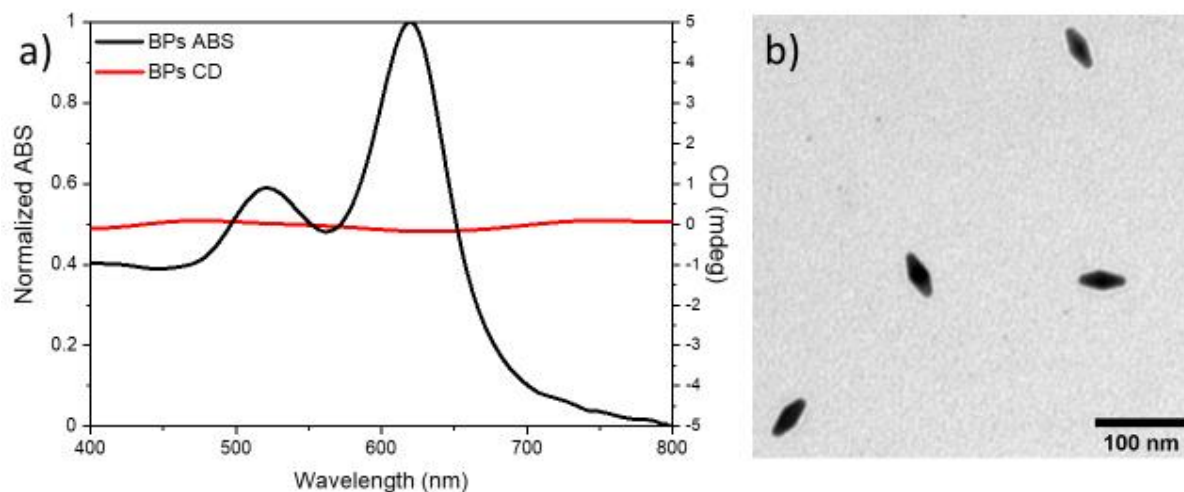


Figure 35. Optical properties and morphology of gold nanobipyramids. (a) Extinction (black line) and circular dichroism (red line) spectra of nanoparticles taken after the synthesis and purification. (b) TEM image of gold nanobipyramids.

IX. 3 Chiral protein aggregates of bovine insulin

As was discussed in the theoretical section of this work, chiral heterostructures with gold nanoparticles are often made of chiral organic templates and achiral gold nanoparticles. In the previous paragraphs, I have presented the optical and morphological properties of achiral gold nanobipyramids. Here, I would like to present my findings concerning the chiral optical matrix used to induce chiroptical properties in achiral nanoparticles.

For my experiments, I have chosen bovine insulin amyloids. Amyloids are ordered fibrillar protein aggregates of characteristic beta-sheet structure, which are associated with neurodegenerative disorders like Parkinson's or Alzheimer's.⁵⁷ In the natural environment, they arise as a result of aggregation of misfolded or partially-folded proteins due to a plethora of pathogenic mutations.²²³ In laboratory conditions, amyloids are usually obtained by incubating a protein solution in a specific buffer, temperature and pH for a prolonged time from a few hours to a few weeks.²²⁴ Recent research reported by Kumar *et al.* already showed that amyloids like alfa-synuclein can helically assemble anisotropic gold nanoparticles leading to a strong chiroptical plasmonic response.⁴⁶ Thus, such chiral nanomaterials are promising candidates for chiral matrices. Using insulin amyloids as a chiral scaffold for nanoparticle arrangement has not been reported yet, although they possess few features advantageous from the point of view of chiral heterostructures. First of all, bovine insulin amyloids can aggregate into chiral superstructures, with strong chiroptical properties.^{225, 226} Secondly, the chirality of insulin amyloids can be controlled by changing the amyloid incubation temperature²²⁷, pH²²⁸ or buffer

composition²²⁹. Additionally, insulin amyloids are polymorphic, so they can take on different sizes and shapes.²³⁰

The first step was to prepare the chiral insulin amyloids. In the case of amyloids, their chiroptical properties are commonly assessed by measuring the circular dichroism induced upon binding of one of the amyloid-specific dyes like thioflavin T (ThT).¹⁷ Thioflavin T composes of benzylamine and benzathine rings freely rotating around their common carbon-carbon bond.²³¹ After binding to one of the beta-sheet structures building amyloid fibrils, the rings become immobilized and the chiral twist between them, following the local twist of the beta-sheet structure, induces circular dichroism.²³²

Preparation of each pre-incubation bovine insulin solution started with diluting 5 mg of bovine insulin protein (in a powder form) in 0.5 ml of MiliQ water. Then, the appropriate amount of sodium chloride (NaCl) was added to the sample to reach the concentration of 100 mM. After that, the pH of each solution was lowered to ~ 2 using a 1 M aqueous (MiliQ water) solution of hydrochloric acid (HCl). The pH was monitored using a commercial electronic pH meter (Mettler Toledo). Then, all samples were vortexed for 30 s to ensure complete dilution of insulin protein powder in the buffer solution. After that, all samples were poured into 1.5 mL Eppendorf tubes, sealed and placed inside a thermoblock for amyloid incubation (Eppendorf ThermoMixer C). All samples were incubated for 48 hours with a mixing speed 1000 rpm (rounds-per-minute) in elevated temperatures. After the incubation, samples were stored in a fridge at 4 °C.

I investigated the influence of three factors on the chiroptical properties of insulin amyloids: temperature, pH and NaCl concentration. In the case of temperature, Dzwolak *et al* reported that changing the incubation temperature from 35 °C to 55 °C allows switching the sign of induced circular dichroism.²²⁷ In the case of pH, Kurouski *et al* demonstrated that the chirality of amyloids could also be controlled via pH since vibrational circular dichroism (VCD) of insulin amyloids incubated with pH in the range from 1.3 to 2.1 is reversed compared to amyloids incubated with pH in the range from 2.4 to 3.1.²³³ In the case of NaCl concentration, Dzwolak²²⁷ and Babenko²³⁴ have presented that chloride ions enable dense packing of insulin amyloid fibrils, leading to the creation of chiral superstructures with strong chiroptical properties.

The chiroptical properties of all explored insulin amyloids were determined using the circular dichroism they induce in ThT upon mixing the dye with the amyloids (Figure 36). The absorption band of ThT mixed with amyloids was located around 450 nm. The concentration of ThT in each sample was equal to 300 mM.

First, I checked the influence of temperature on the chiroptical properties of amyloids. Amyloids incubated in three different temperatures: 35 °C, 40 °C and 55 °C had three significantly different spectra (Figure 36a). Amyloids incubated at 35 °C (Figure 36a, golden line) showed no visible chiral response in the ThT absorption range. On the other hand, amyloids incubated at 55 °C (Figure 36a, red line) presented a strong (-11 mdeg) negative CD band at 450 nm. Incubation at 40 °C (Figure 36a, orange line) resulted in a more complicated

chiral response: the signal was positive (+7 mdeg) at 450 nm and then, in higher wavelengths, switched chirality to negative values with minimum (-9 mdeg) at 475 nm. Such sample behavior indicates the presence of the Cotton effect: the change from positive sign to negative sign (positive Cotton effect) or negative sign to positive sign (negative Cotton effect) of the optical rotatory dispersion and CD of a chiral molecule near the molecule absorption range. The Cotton effect visible in the CD of insulin amyloids stained with ThT has already been reported before, and research indicates that the source of this phenomenon is the interaction of aromatic ThT rings with specific parts of the insulin amyloid structure.²³⁵ Comparing all three samples showed that temperature has a major impact on the chiroptical properties of amyloids and higher temperatures, such as 55 °C, lead to stronger chiral signals. Thus – all further described samples were incubated at 55 °C.

Next, the influence of pH on the chiroptical properties of insulin amyloids was checked (Figure 36b). Amyloids were incubated with 3 different pH values within the limits reported by Kuorouksi²³³: pH 1.5, pH 2 and pH 2.5. The sample incubated in pH 1.5 (Figure 36b, blue line) was characterized by a negative band (- 8 mdeg) shifted to 460 nm. The one incubated at pH 2 (Figure 36b, purple line) exhibited a strong negative chiral response (-57 mdeg) at 450 nm. Amyloids incubated at pH 2.5 (Figure 36b, pink line) resembled the ones incubated at 40 °C and showed a chiral response characterized by a weak Cotton effect with a minimum shift to 470 nm. Analysis of all three samples indicated that pH 2 was the most optimal to obtain highly chiral samples.

The last factor checked was the influence of sodium chloride. Three samples were prepared based on the most optimal set of conditions gained from previous experiments (55 °C, pH 2). The concentration of sodium chloride was equal to 0 mM, 25 mM and 100 mM. The insulin sample incubated without sodium chloride (Figure 36c, yellow line) did not show any chirality. The amyloids incubated with 25 mM of NaCl (Figure 36c, bright green line) exhibited a strong (-50 mdeg) negative chiral band located at 450 nm. Interestingly, the sample incubated with the highest concentration of NaCl (Figure 36c, dark green line) exhibited extreme chiroptical response with CD values reaching -148 mdeg. What is more important, experiments with different concentrations of sodium chloride have shown that NaCl can controllably increase the chiroptical response of insulin amyloids.

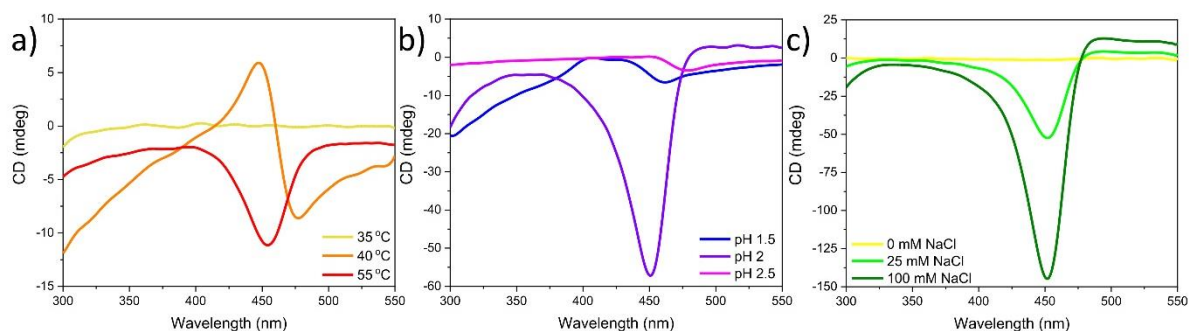


Figure 36. CD spectra of insulin protein aggregates incubated with controlled temperature (a), pH (b) and NaCl concentration (c).

After exploring how factors such as temperature, pH and NaCl concentration influence the chiroptical properties of insulin samples, I checked how they affect their morphology (Figure 37). Amyloids incubated in different temperatures are marked with the letter A, ones incubated with different pH are marked with the letter B and samples incubated with different NaCl concentrations are marked with the letter C. Amyloids incubated at 35 °C (Figure 37, A1) were made of thick, stiff fibrils reaching 1.7 µm in length with an average width of 52.3 ± 8.2 nm and average height of 16.5 ± 1.6 nm. Insulin fibrils incubated at 40 °C (Figure 37, A2) were shorter, more flexible and entangled with each other. The average length was equal to 583 ± 196 nm, average width to 42.3 ± 4.8 nm and average height to 4.7 ± 1.1 nm. Incubation at 55 °C (Figure 37, A3) led to the creation of insulin superstructures with sizes of a few µm and height above 100 nm. The lowest checked pH value (Figure 37, B1) caused the formation of short and thin fibrils with an average length of 330 ± 15 nm, average width of 31.0 ± 6.0 nm and average height of 7.3 ± 2.2 nm. One could also notice amorphous protein aggregates lying around the fibrils. Incubation in pH 2 (Figure 37, B2) resulted in straight single fibrils with a visible helical twist. Their average length was equal to 793 ± 85 nm, average width 29.3 ± 1.5 and average height 4.6 ± 1.6 nm. The sample incubated at pH 2.5 (Figure 37, B3) did not create any fibrillar forms. Instead, the samples were full of amorphous protein aggregates with a diameter of ~ 100 nm. All samples incubated with different sodium chloride concentrations resulted in the formation of mature amyloid fibrils. Insulin incubated without NaCl (Figure 37, C1) created long fibrils with visible helical twist equal to 87.6 ± 15.9 nm. Their average length was equal to 705 ± 212 nm, average width to 21.0 ± 3.0 nm and average height to 4.52 ± 0.67 nm. As could be observed in Figure 37, C2, incubation with 25 mM NaCl caused aggregation among some fibrils. They were longer and thicker than fibrils incubated without NaCl, with an average length of 784 ± 180 nm, an average width of 31.6 ± 6.4 nm and an average height of 9.81 ± 2.12 nm. Their helical twist was equal to 76.3 ± 17.1 nm. Samples incubated with the highest NaCl concentration (Figure 37, C3) caused further aggregation. They were made of fibril aggregates with an average length of 869 ± 250 nm, average width of 34.6 ± 5.2 nm and average height of 9.23 ± 2.97 nm. The average helical twist of individual fibrils included in the aggregates was equal to 93.0 ± 18.6 nm.

Analysing the morphology of all samples in the context of their incubation conditions shows that pH plays a major role in the formation of amyloid structures and sodium chloride controls their aggregation. Experiments showed, that in conditions of pH ~ 2 and high sodium chloride concentration (0.1 M NaCl), any incubation temperature from 35 °C to 55 °C will result in the formation of insulin amyloid structures, but with significantly different morphology (Figure 37, A1-A3). On the other hand, pH noticeably different from 2, like 1.5 or 2.5, results in the creation of samples full of small, short fibrils and unreacted proteins (Figure 37, B1) or no amyloids at all (Figure 37, B3). Interestingly, sodium chloride seems to control the aggregation of insulin fibrils. The sample incubated without NaCl (Figure 37, C1) resulted in long, single fibrils, the one incubated with 25 mM NaCl (Figure 37, C2) showed a certain degree of aggregation, meanwhile insulin incubated with 100 mM NaCl (Figure 37, C3) created bigger aggregates with no single fibrils around them. Since creating chiral heterostructures with gold nanoparticles requires a homogenous chiral matrix exhibiting strong chiroptical properties, for further research I decided to choose fibrils incubated with different NaCl concentrations. These

samples presented high homogeneity in terms of morphology and controllable chiroptical properties. Moreover, it was reported that observed fibrillar aggregation is possible due to electrostatic screening caused by the ionic strength of chloride ions.²³⁴ Such an effect could also be beneficial in the case of interaction with gold nanoparticles, which could be repelled from the fibrils due to their surface charge.

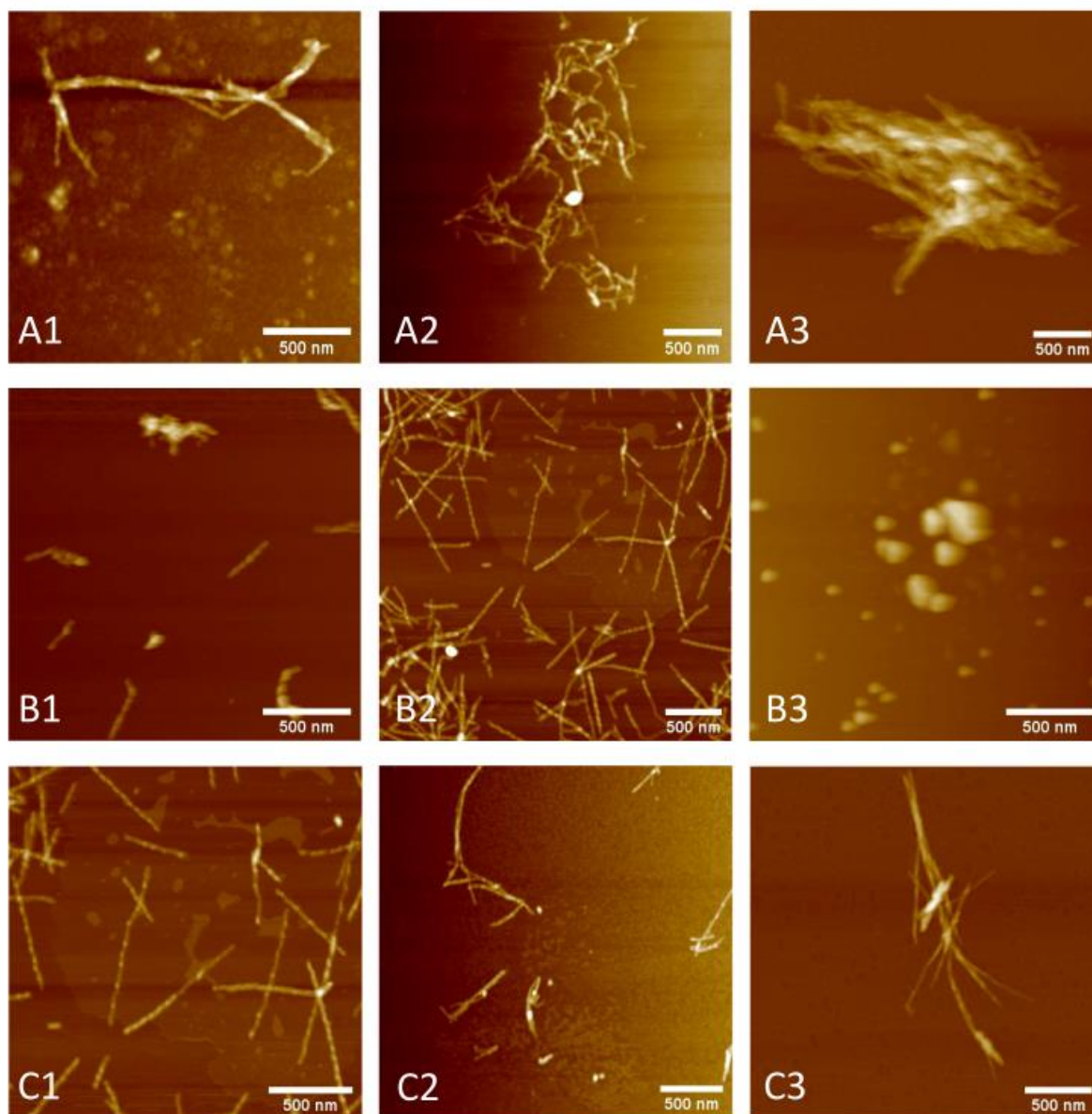


Figure 37. Morphology of insulin protein aggregates incubated with controlled: temperature (A1-3, 35 °C - 55 °C), pH (B1-3, pH 1.5 – 2.5) and NaCl concentration (C1-3, 0 mM – 100 mM). All scans are based on the samples presented in Figure 2, diluted 1000 times with MiliQ water before drop-casting on mica substrate.

IX. 4 Chiral heterostructure sample preparation

After preparation and analysis of different chiral insulin aggregates, I started working on the creation of chiral heterostructures. As was discussed in detail in the literature review, mixing gold nanoparticles with chiral amyloids, can induce CD signal in their plasmonic range. In the case of samples described by Kumar,⁴⁶ it was possible due to the chiral arrangement of

nanoparticles governed by the chiral matrix - α -synuclein amyloid fibrils. Thus, my main goal was to achieve a sample in which mixing gold nanobipyramids with chiral insulin amyloids will lead to similar chiral optical effects. The necessary conditions for inducing the chiroptical properties of AuBPs upon binding to amyloids were verified by measuring the circular dichroism (Figure 38a-c) and extinction (Figure 38d-f) spectra. The amyloid selected for these studies was the sample incubated with 100 mM NaCl, presenting the strongest chiroptical properties (Figure 36c, dark green line).

The first factor checked was the influence of sodium chloride. Gold nanobipyramids used in these studies were functionalized with CTAB ligands, so the surface of the nanoparticles was positively charged.²³⁶ As confirmed by Psonka-Antonczyk *et al.*, the charge of insulin amyloids in acidic conditions is also positive.²³⁷ This would lead to repulsive electrostatic interactions between amyloids and nanoparticles. However, in the presence of sodium chloride, Na⁺ and Cl⁻ ions could screen electrostatic interactions between the BPs surface and amyloids, promoting their mutual binding.²³⁸ To confirm that, I prepared two samples made of BPs mixed with insulin amyloid: without additional NaCl in the mixture (Figure 38a, light-green line) and with a 100 mM final concentration of NaCl in the mixture (Figure 38a, dark-green line). In the CD spectra of the first sample, one could notice a negative chiral signal with magnitude -1 mdeg at ~550 nm. The signal was strongly blue-shifted from the BPs LSPR maximum located at 622 nm (Figure 38b, dashed line). As could be seen in the results reported by Kumar *et al.*, strongly shifted bands could originate from the aggregates of nanoparticles.⁴⁶ However, the extinction spectra of the same sample (Figure 38b, light-green line) showed no noticeable LSPR band shifts, which may indicate that the observed signal comes from a few large aggregates constituting a minority among all BPs in the sample. Interestingly, the sample prepared in conditions of high sodium chloride concentration presented a stronger chiral signal of magnitude -3.5 which was located at the LSPR band maximum - 622 nm. Moreover, high salt content did not cause any shift in the extinction spectra of BPs (Figure 38b, dark-green line). Taking all of that into account, this experiment confirmed, that high sodium chloride concentration increases the mutual amyloid-BP interaction which could be observed by the increased magnitude of the induced chiral signal in the plasmonic range.

The second explored factor that could influence the amyloid-BP interaction was their mutual concentration ratio in the final sample. The mutual ratio was verified by the extinction ratio, the relationship between the intensity of amyloid extinction intensity measured at 275 nm and BPs LSPR intensity measured at 622 nm. Under the conditions determined in the previous experiment (100 mM NaCl), 5 samples were prepared and measured, characterized by amyloid/BPs extinction ratios equal to 1, 1.5, 2.5, 5 and 7.5. As could be seen in their CD spectra (Figure 38c) amyloid/BPs extinction ratios between 1 and 2.5 did not show any sign of a chiral plasmonic signal. The sample with amyloid/BPs extinction ratio equal to 5 (Figure 38c, orange line) presented a weak negative band, visible in the range from 620 nm to 650 nm. Only the extinction ratio equal to 7.5 resulted in a strong (-4.5 mdeg) negative chiral signal, with a maximum located at 625 nm. In addition, no shift of the bipyramid LSPR bands was observed in any of the measured samples (Figure 38d). The conducted experiment showed that the most

optimal extinction ratio of bipyramid to chiral matrix for this type of heterostructure was equal to 7.5 and this ratio was used in all further experiments.

The last tested factor was time needed for the proper binding of BPs to chiral insulin aggregates and stabilizing their chiroptical properties. To check that, another sample was prepared, with 100 mM NaCl and amyloid/BPs extinction ratio equal 7.5, and its CD (Figure 38e) and ABS(Figure 38f) were measured every 15 minutes. As shown by the CD spectrum taken immediately after sample preparation (Figure 38e, bright green line), the induction of chiral optical properties occurs instantaneously, as proved by -2 mdeg negative band located around 600 nm. With time, the maximum of the observed chiral band shifts to the LSPR maximum, reaching it after 30 minutes (Figure 38e, light-blue line). The chiral signal stabilized after 60 minutes, reaching the magnitude of -4.5 mdeg (Figure 38e, dark-blue line). Moreover, the extinction spectra showed that the LSPR of BPs does not shift over time (Figure 38f). To sum up, the experiment has shown that the induction of chirality is immediate upon mixing the BPs with insulin amyloids. However, the signal magnitude increases over time, reaching its maximum after 60 minutes.

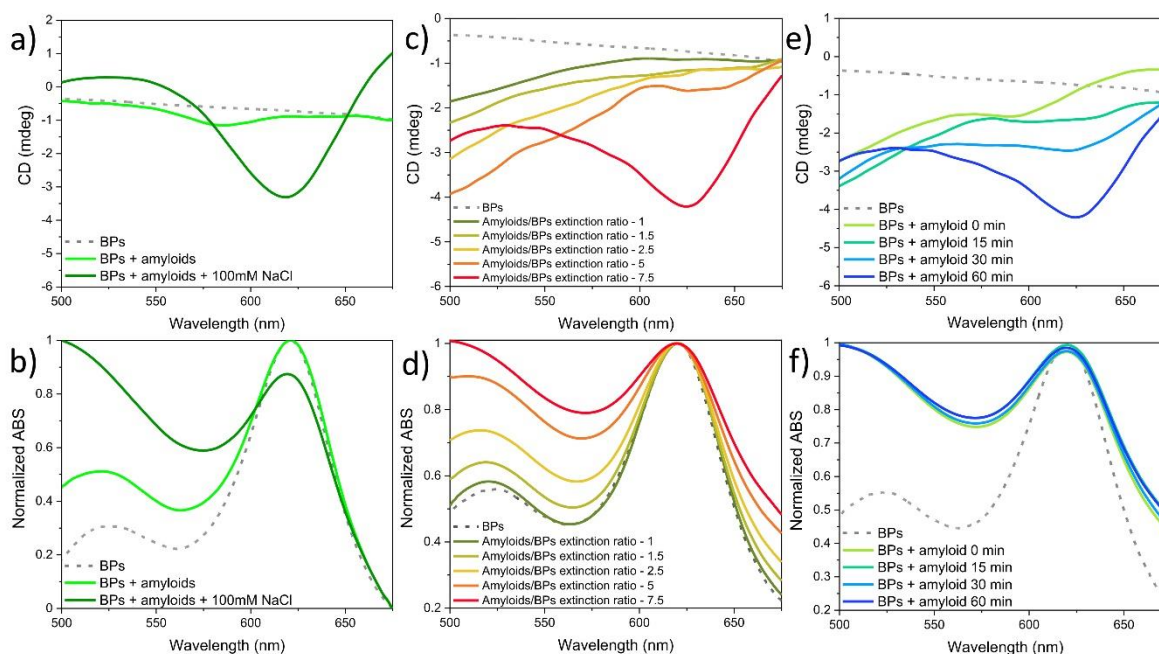


Figure 38. Optical properties of gold nanobipyramids mixed with chiral insulin matrix in different conditions. Images (a) and (d) show heterostructures created with various NaCl concentrations, images (b) and (e) created with different amyloid/BPs ratios and images (c) and (f) - after different amounts of time.

The most optimal set of parameters was determined based on the presented experiments with creating chiral heterostructures in various conditions. Chiroptical properties measurements of heterostructures prepared with and without sodium chloride showed that Na^+ and Cl^- ions allow efficient induction of chiral plasmon signal (Figure 38a), without causing any aggregation of nanoparticles (Figure 38b). Experiments with different Amyloid/BP extinction ratios (Figure 38c, d) determined the proportions required to observe the strongest induced CD signal.

However, monitoring their chiroptical properties over time (Figure 38e, f), showed that the induced chiral signal increases with time and achieves stable value after ~60 minutes.

IX. 5 Exploring the chirality transfer between chiral insulin matrix and gold nanobipyramids

After determining the conditions required for efficient induction of chiral optical properties in gold nanobipyramids upon binding to insulin amyloids, I checked how the amyloid itself would affect the observed chirality transfer. To explore that topic, I mixed the BPs with three chiral matrices: pre-incubation solution of insulin proteins (native insulin), insulin amyloids incubated in pH~2 at 55 °C without sodium chloride (amyloids type 1), and insulin amyloids prepared in the same conditions, but with 100 mM NaCl (amyloids type 2). Mixing BPs with native insulin proteins did not induce any chiral properties in nanoparticles (Figure 39a, black line). On the other hand, mixing them with both types of amyloids resulted in a chiral plasmon. Amyloid type 1 induced a negative chiral signal with a magnitude of -1 mdeg located at 585 nm (Figure 39a, red line) and amyloid type 2 induced a stronger negative chiral signal with a magnitude around -4 mdeg, located at 625 nm (Figure 39a, blue line). Moreover, mixing the BPs with all three types of insulin has caused a minor red-shift ~ 2 nm of the longitudinal LSPR band of BPs, as presented by their extinction spectra (Figure 39b). However, a small few-nm shift in LSPR peak location can be explained by a changed BPs environment upon binding to amyloids.²³⁹

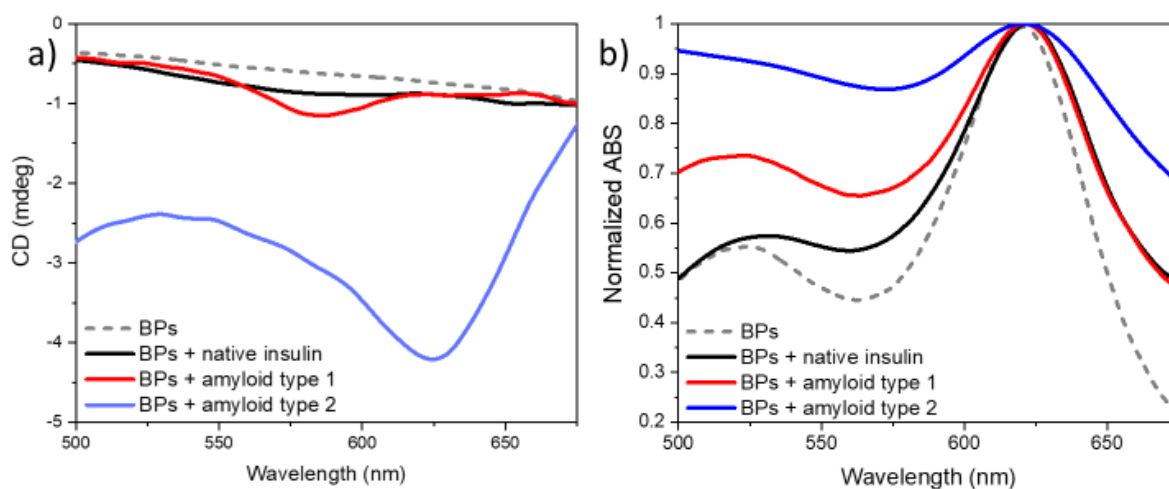


Figure 39. Chirality transfer between gold nanobipyramids and different types of chiral protein aggregates. Circular dichroism (a) and normalized extinction (b) spectra of gold nanobipyramids mixed with three types of insulin samples. Images are reprinted with permission from reference no.²⁴⁰ Copyright © 2023 American Chemical Society.

After confirming that different protein aggregates influence the chirality transfer differently, I explored what is the origin of the observed effect. First of all, I checked the morphology of all three chiral heterostructures to see if the observed chiroptical effects come from the chiral arrangement of nanoparticles upon binding to amyloids. TEM images of BPs mixed with native insulin (Figure 40a) showed that nanoparticles are coated with proteins and separated from each other. In the case of TEM images of BPs mixed with amyloid type 1 (Figure 40b), all visible BPs were bound to the amyloid surface. BPs were strongly separated from each

other with an average separation distance equal to 176.87 ± 129.66 nm. Upon mixing with amyloid type 2, more BPs were bound to the amyloid surface (Figure 40c). However, the behaviour of BPs was similar – all visible nanoparticles were bound to the amyloid surface and were separated from each other. The average separation distance in this case was equal to 96.92 ± 50.67 nm. No local chiral ordering of BPs was observed in any of the three samples. In addition, the BPs separation distance in samples prepared with amyloids type 1 and 2 were equal to 7.7 and 4.2 times the size of BPs, respectively. Thus, plasmon-coupling, which may be responsible for chiroptical properties in helically assembled NPs aggregates with nanoparticles located near each other, was negligible in the studied samples.²⁴¹

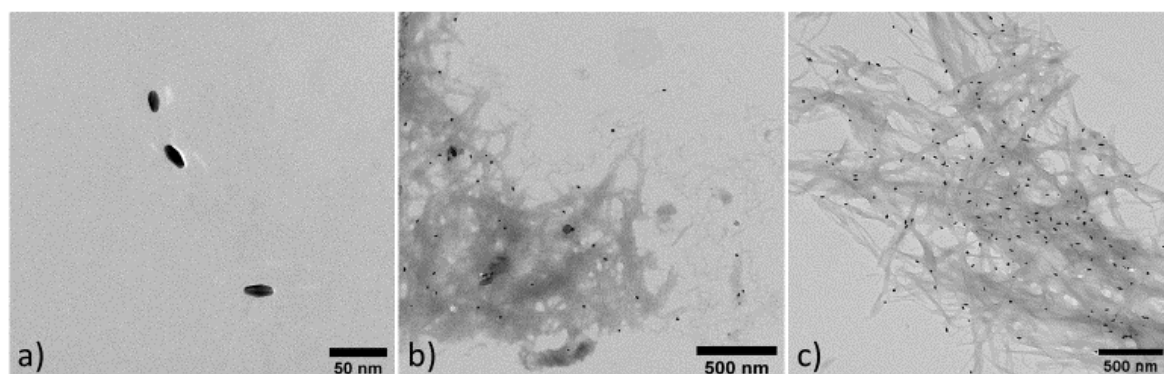


Figure 40. Morphology of gold nanobipyramids and different types of chiral protein aggregates. TEM images of BPs mixed with native insulin (a), amyloid type 1 (b) and amyloid type 2 (c). Images are reprinted with permission from reference no.²⁴⁰ Copyright © 2023 American Chemical Society.

As mentioned before, chiral optical properties of nanoparticles could also be induced by mutual chiral arrangement even in small aggregates like dimers or trimers.⁵² In order to check if similar effects could explain the origin of chiroptical properties in studied samples, I did a statistical analysis of BPs forms present in the chiral heterostructures, based on their TEM images. In the case of BPs mixed with amyloid type 1, monomers constitute almost 100% of the nanoparticles visible in the images (Figure 40b). However, after mixing with amyloid type 2, one could also observe BPs dimers, trimers and bigger aggregates, denoted as oligomers in the analysis (Figure 41a). The majority of BPs (90.2%) were still in a monomer form with aggregates constituting only 9.8%. Dimers and trimers accounted for 8.7% and 0.8%, respectively. Only 0.3% of nanoparticles assembled into bigger aggregates. Taking into consideration, that nanoparticle aggregates constituted less than 10% of the whole population and no major shift of LSPR bands was observed, they most probably played a minor role in the registered induction of chiroptical properties.

The lack of chiral aggregates or helical arrangement of nanoparticles led to the search for the source of chirality in other described effects. As mentioned in the literature part of this dissertation, there are three mechanisms leading to the chiroptical activity of achiral anisotropic nanoparticles.²⁴² Apart from the chiral assembly of nanoparticles, which was not observed for the presented samples with BPs, chiroptical properties can be induced *via* chiral field enhancement due to antenna-like properties of plasmonic nanoparticles²¹⁸ or *via* Coulombic

interactions between the nanoparticles and their chiral surrounding¹⁰². Among these two, Coulombic interactions are more specific – the strength of such interaction depends on the distance between the nanoparticle and chiral molecule, the size of the nanoparticle, the mutual dipole orientation or the distance between CD/absorption bands of both structures taking part in the interaction.¹⁰¹

In the three studied chiral heterostructures made of BPs mixed with insulin, the nanoparticles were bound to the amyloid surface made of chiral proteins (amyloid type 1 and 2) or chiral proteins themselves (native insulin), so the distance between the nanoparticles and chiral molecules allowed for efficient Coulombic interaction in all three samples. Presented samples were prepared using the same stock solution of BPs so the average size of nanoparticles present in all three samples is similar and equal to 23 x 11 nm. The first difference that could influence the ability to induce chiroptical activity in BPs was the interaction between protein and BPs dipoles in three samples. Upon mixing BPs with native insulin, the proteins coated the whole surfaces of nanoparticles, resulting in the random ordering of protein dipoles with respect to BPs dipole, preventing the induction of any chirality based on the Coulombic interactions theory.⁵⁴ On the other hand, BPs bound to the amyloid surface at a certain angle could interact with their ordered β -sheet structure with locally aligned molecular dipoles, leading to efficient chirality transfer. CD experiments (Figure 39) have proven that in the case of studied chiral heterostructures, the induction of chirality is observed only in samples with amyloids, which agrees with that concept. Thus, in the next step, I explored the distribution of angles between the long axis of amyloids and BPs. The mutual angle orientation was determined based on TEM images of both heterostructures with amyloids, using the ImageJ software (Figure 41b). For BPs mixed with amyloid type 1 (Figure 41c, red columns), most of the nanoparticles were oriented along the long fibril axis, with angles in range from 0° to 15°. In the case of BPs mixed with amyloid type 2 (Figure 41c, blue columns), the majority of BPs were oriented in the range from 15° to 30°. In both cases, there was a favourable angle of BP orientation with respect to the amyloid long axis, resulting in a fixed dipole arrangement, allowing the induction of chirality. The last factor influencing the Coulombic interaction that needs to be discussed is the separation between the absorption bands of chiral molecules and nanoparticles. According to measured ABS spectra, amino-acids related absorbance of insulin is located around 275 nm (Figure 41d, red line) meanwhile BPs are characterized with two plasmon bands, located at 524 nm and 620 nm (Figure 41d, black line), respectively. This would lead to NP-molecule band separation of amyloid and BPs equal around 350 nm, which should result in a relatively weak signal. However, the optical extinction of insulin is diminishing slowly in the VIS range and is equal to 0.05 at 620 nm, zeroing above 700 nm. As could be seen in the ABS spectra of BPs mixed with insulin amyloids (Figure 41d, blue line), the signal from amyloids overlaps with the LSPR of BPs, increasing the ABS value from 0.15 to 0.2. This would mean, that BPs could still interact with the chiral molecule due to ABS spectra overlap in this range. Moreover, it also implies that this type of chirality transfer effect may not work with nanoparticles characterized by more red-shifted LSPR, such as gold nanorods or even bigger nanobipyramids.

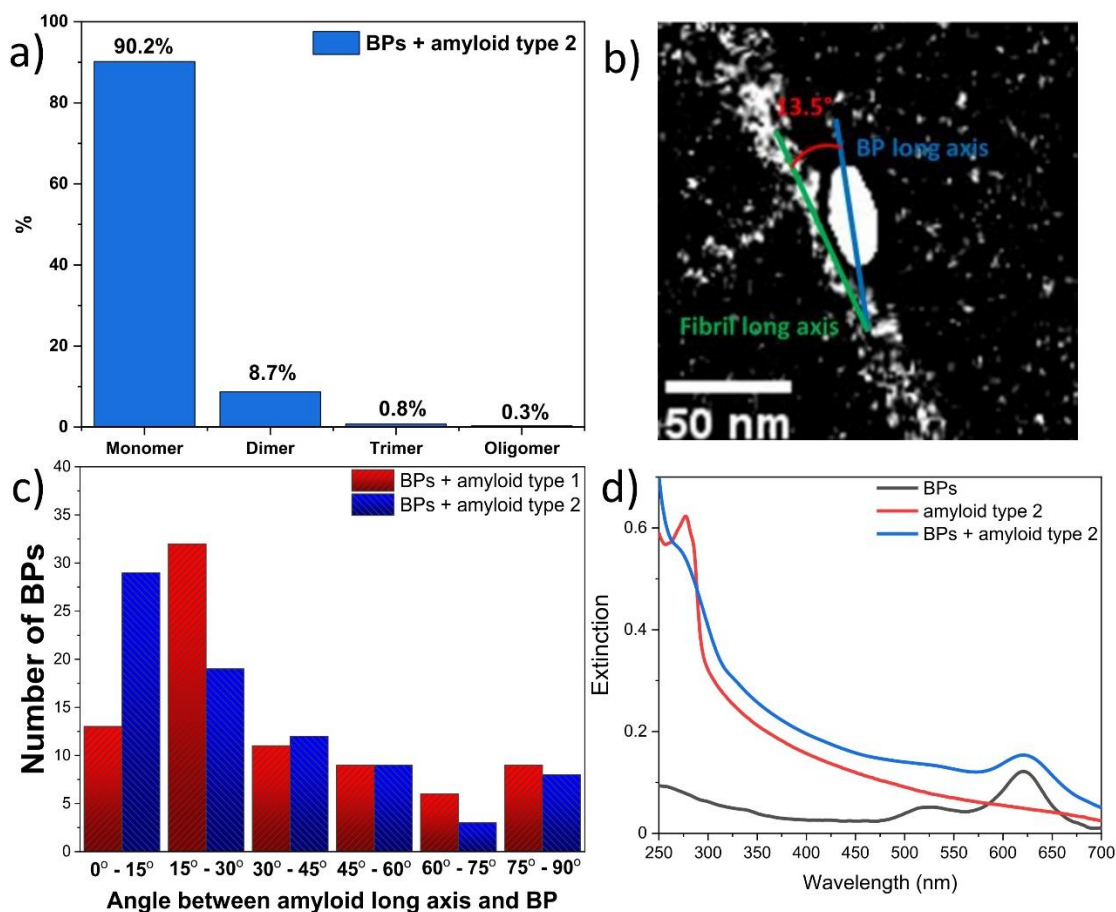


Figure 41. Statistical analysis of gold nanobipyramids and different types of chiral protein aggregates. Statistical analysis of aggregation stage of BPs bound to amyloid type 2 (a). Scheme showing how the angles between insulin fibril long axis and BPs long axis were determined (b). Statistical distribution of orientation angles of BPs in respect to fibril long axes in chiral heterostructures made with amyloid type 1 and type 2 (c). Extinction spectra of BPs and amyloid type 2 (d), before and after creating chiral heterostructures. Images (a) and (c) are reprinted with permission from reference no.²⁴⁰ Copyright © 2023 American Chemical Society.

After explaining the possible origin of the observed chirality transfer from the chiral matrix to gold nanoparticles, one last question remained - what features of protein aggregates do the BPs sense?

To understand this, a more detailed structural analysis of the chiral matrices used was performed, based on their CD spectra measured after the incubation and without thioflavin T (Figure 42a). The CD spectrum of amyloid type 1 (Figure 42a, red line) was characterized by one strong (-270 mdeg) negative band located at 221 nm. As reported by Bouchard *et al*, such a signal is often ascribed to the presence of extensive β -sheet structure.²⁴³ Interestingly, in the CD spectrum of amyloid type 2 (Figure 42a, blue line), apart from the strong band located at 221 nm, two more appeared – located at 255 nm and 275 nm. According to a study by Kelly *et al*, these bands may originate from aromatic amino acids present in insulin: the band at 255 nm could be attributed to phenylalanine, and the band at 275 nm to tyrosine.²⁴⁴ Comparing the spectra of amyloids incubated with and without NaCl confirmed that sodium chloride alters not only the chiroptical properties of amyloids, but also their secondary structure, probed by CD.

To check if BPs are sensing any of these specific structural features, I decided to create another type of chiral heterostructures, mixed with insulin amyloids incubated with 25 mM NaCl (amyloid type 3). Its circular dichroism spectrum (Figure 42a, green line) showed that this sample contained intermediate features between amyloids type 1 and 2 – an extensive β -sheet band located at 221 nm and a second band located at 275 nm, which could be attributed to tyrosine residues. More importantly, after mixing with BPs in the same conditions as previous chiral heterostructures, an induced chiral plasmon signal was observed (Figure 42b), located at 620 nm. This result proved that BPs stronger interact with insulin amyloid incubated with sodium chloride. Extensive NaCl was present in all three solutions with chiral heterostructures, but only amyloid types 2 and 3 resulted in strong induced chiral plasmon located in the correct wavelength range. The morphology of BPs mixed amyloid type 3 (Figure 42c) was similar to that of chiral heterostructures created with amyloid type 2. The BPs covered only the amyloid surfaces and were separated from each other with an average distance equal to 126.15 ± 86.35 nm (~ 6 times the length of BPs). Moreover, the statistical analysis (Figure 42d) showed that most (90%) of the BPs bound to amyloid type 3 are monomers with dimers and trimers constituting accordingly 7.6% and 2% of the whole BPs population in this sample. All of that led me to the conclusion that BPs could sense the chirality from tyrosine residues, present in amyloid type 2 and 3, which get exposed due to incubation with NaCl.²²⁹

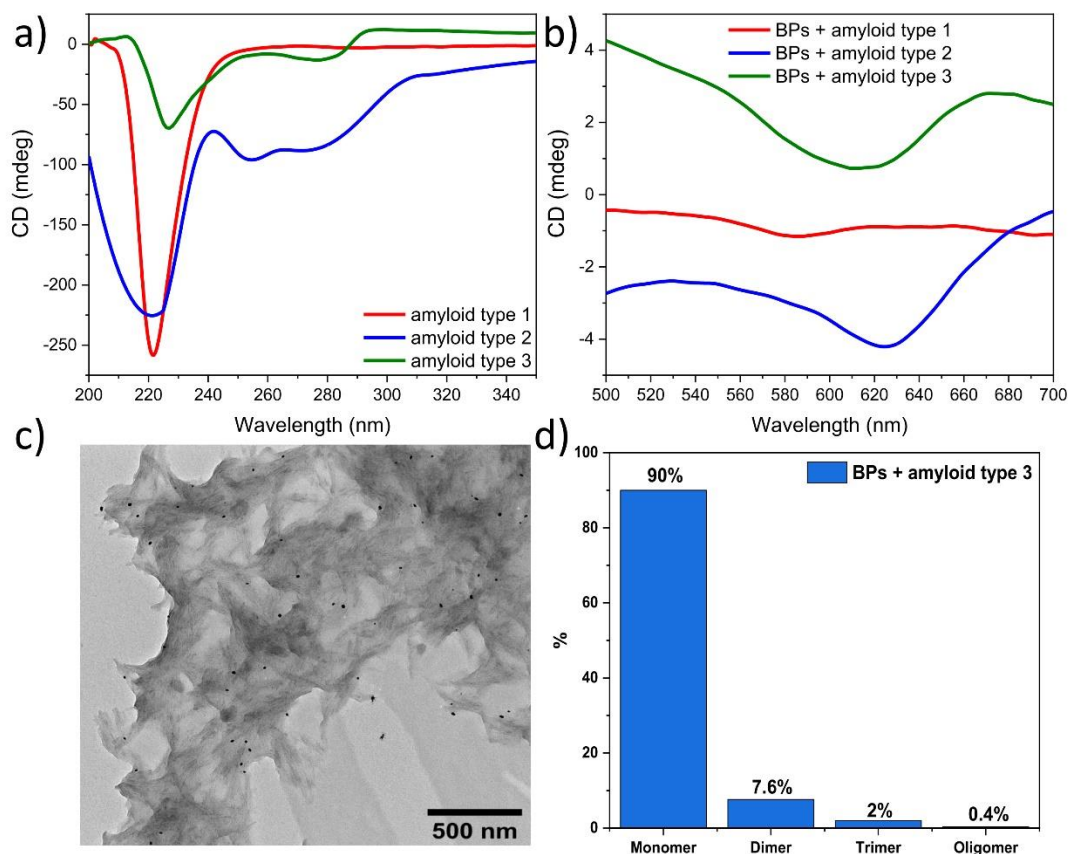


Figure 42. Chiroptical properties and morphology of chiral heterostructures. Circular dichroism spectra of three types of amyloids (a) and chiral heterostructures their created upon mixing with BPs (b). TEM image (c) along the statistical distribution (d) of BPs aggregation state in chiral heterostructure created with BPs and amyloid type 3. Images are reprinted with permission from reference no.²⁴⁰ Copyright © 2023 American Chemical Society.

IX. 6 Chirality transfer between the plasmonic nanoparticles and amyloid fibrils at single-particle level

After proving that chirality can be transferred from chiral protein aggregates to achiral gold nanoparticles, I started a scientific collaboration to check if chirality could be transferred between single amyloid fibrils and single gold nanoparticles. In this case - gold nanorods. Research on this topic was carried out in collaboration with Professor Julie Biteen and Dr Saaj Chattopadhyay from the University of Michigan, Ann Arbor (USA), both specializing in single-molecule and single-particle microscopy of nanoparticles. In this chapter, I will present my work on this topic, which has focused on sample preparation and CD experiments made with bulk samples.

The first step was the preparation of an appropriate chiral matrix. Since the main goal of this project was to explore the chirality transfer between single amyloid fibrils and single gold nanoparticles, the matrix needed to consist of long, unaggregated fibrils. As in the case of the chiral heterostructures with BPs, bovine insulin protein was chosen as the matrix material. The insulin was first dissolved in deionized water resulting in a concentration of 10 mg/ml, then the solution pH was lowered to 2 and it was incubated at 70 °C for 18h at a mixing speed of 700 rpm. After the incubation, amyloids were sealed and stored in a fridge at 4 °C. After the incubation, I checked the morphology of amyloids using AFM (Figure 43a). The sample was prepared similarly to the samples shown in Figure 37, using the protocol described in the experimental part at the beginning of this chapter. The described incubation conditions resulted in long amyloid fibrils. Their average length was equal to $1.37 \pm 0.64 \mu\text{m}$, average width to $17.7 \pm 0.4 \text{ nm}$ and average height to $3.49 \pm 0.34 \text{ nm}$. Moreover, diluting the sample to a final concentration of protein equal to 10^{-5} mg/ml made it possible to obtain single, separated fibrils (Figure 43b), which was the condition required for performing single-molecule microscopy on these samples. After confirming the morphology of amyloids, their chiroptical properties were measured. The CD spectra (Figure 43c) confirmed that this type of amyloid can also induce chirality in dye molecules bound to them. The induced ThT CD band was located at 450 nm and characterized by a negative signal of magnitude around -3 mdeg.

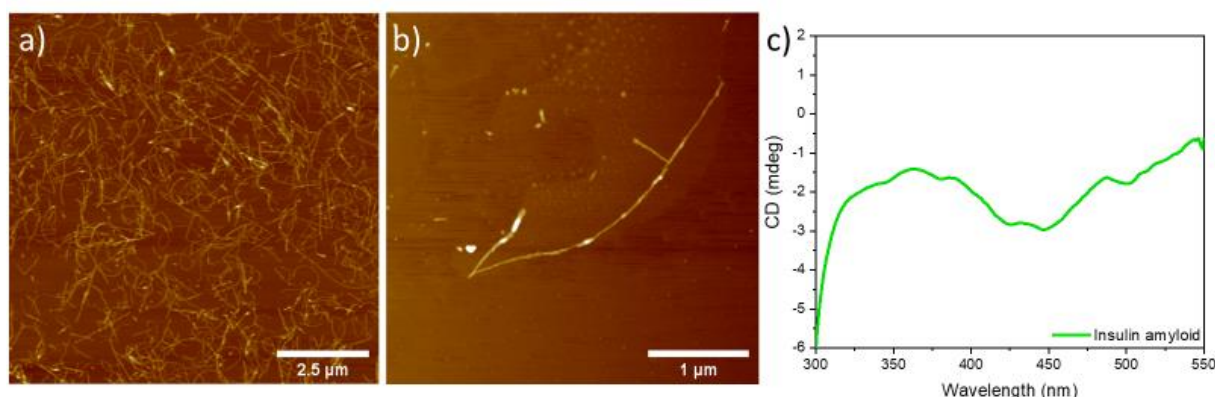


Figure 43. Morphology and chiroptical properties of insulin amyloids. AFM images of insulin amyloid solutions diluted 1000 (a) and 1000 000 (b) times. Circular dichroism spectra (c) of insulin amyloids stained with ThT.

After determining the morphology and chiroptical properties of insulin amyloids, I explored the conditions required for chiral transfer between chiral insulin and achiral gold nanorods (AuNRs). AuNRs, similarly to BPs, were stabilized with CTAB and dispersed in deionized water. They were purchased from Nanopartz Inc. and their size was 80 nm x 40 nm. First, the nanorods were mixed with amyloids in conditions determined from experiments with gold nanobipyramids. CD spectra confirmed that gold nanorods were achiral (Figure 44a, dashed line) and extinction spectra (Figure 44b, dashed line) showed that their LSPR was located in the visible range, at 640 nm. After mixing with insulin amyloids (using the same ratios as in experiments with BPs), the signal decreased with increasing wavelength (Figure 44a, purple line). However, no induced chiral band located at or near the LSPR wavelength was observed. The extinction spectrum of AuNRs (Figure 44b, purple line) also remained unchanged. After the addition of NaCl, to reach the final concentration equal to 100 mM, the CD signal slightly increased (Figure 44a, blue line), but still no chiral plasmon was observed, showing that conditions determined from the experiments with BPs could not induce chiral plasmon in much bigger gold nanorods. Moreover, the extinction spectrum of AuNRs has visibly changed (Figure 44b, blue line) – the intensity of the transverse LSPR band has lowered and a new peak appeared located at 610 nm, between transverse and longitudinal LSPR bands. The appearance of a new band indicated that the addition of sodium chloride caused a strong aggregation of a large amount of nanoparticles present in the solution. Target samples were to be stained with Thioflavin T so that the amyloid signal could be easily localized under the microscope and separated from the nanoparticle signal. Because of that, I also checked how ThT will influence the chiroptical properties of explored chiral heterostructures with AuNRs. As could be observed in Figure 44a (green line), the addition of 100 μ M ThT to the solution did not result in any chiral plasmon signal. The extinction spectrum (Figure 44b, green line) also resembled the one measured before the addition of the dye. In the end, I prepared a sample with chiral heterostructures created in similar conditions but without the addition of sodium chloride responsible for strong AuNRs aggregation. Interestingly, in the CD spectrum of this sample (Figure 44a, red line), both a band originating from the dye, located at 450 nm and a broad negative band located near the LSPR of the nanoparticles could be seen. Moreover, the extinction spectrum (Figure 44b, red line) has confirmed that there was no major nanoparticle aggregation since both LSPR bands were located in the same range as bands from pure AuNRs solution and no new band was observed. Therefore, these conditions were selected for further research.

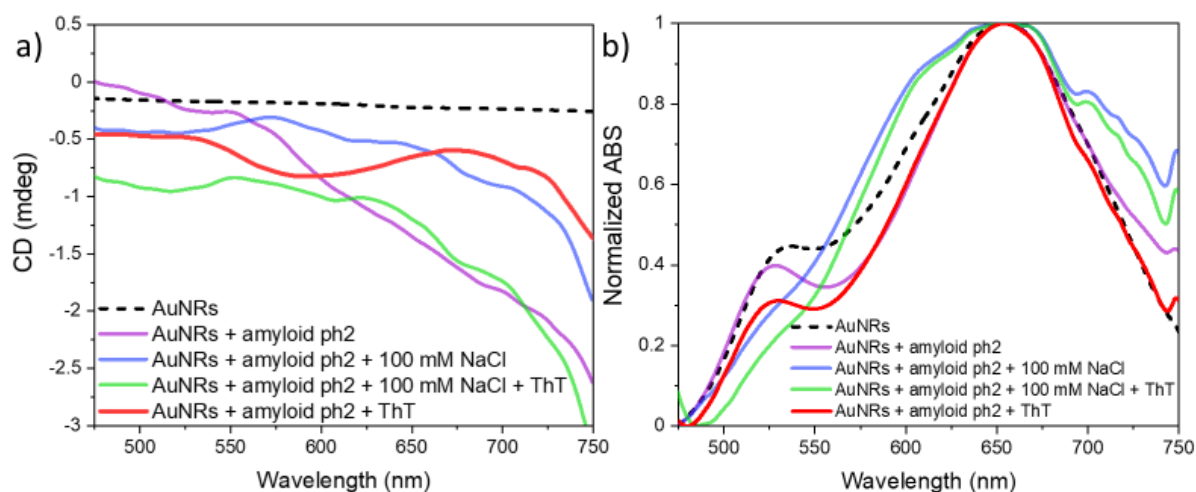


Figure 44. Chiroptical properties of gold nanorods mixed with insulin amyloid in different conditions. Circular dichroism (a) and extinction (b) spectra.

After conducting experiments with different conditions, it turned out that the induction of a chiral plasmon in samples with large nanorods is also possible, but in different conditions than BPs. The last factor I checked was the pH of amyloids. According to research by Psonka-Antonczyk *et al*, the charge of insulin amyloid fibrils at low pH is positive, meanwhile, in neutral pH it is negative.²³⁷ According to the information provided by the AuNRs manufacturer, the zeta potential of the nanorods is equal to +38 mV. Thus, without a repulsive interaction screening agent like sodium chloride, the nanoparticles cannot bind efficiently if mixed with amyloids prepared at low pH. In the next experiment, the pH of insulin amyloid fibrils was increased from 2 to 6, to decrease the repulsive interactions between them and nanoparticles. The circular dichroism spectra of gold nanorods mixed with insulin fibrils (Figure 45a, green line) did not show any chiral signal coming from nanoparticles or their aggregation. However, after the addition of Thioflavin T, a new negative broad band appeared (Figure 45a, blue line), spanning in the range from 500 nm to 750 nm, with a maximum located at 640 nm. Despite such a wide band range, the extinction spectrum (Figure 45b, blue line) did not show the presence of any nanoparticle aggregates in the sample.

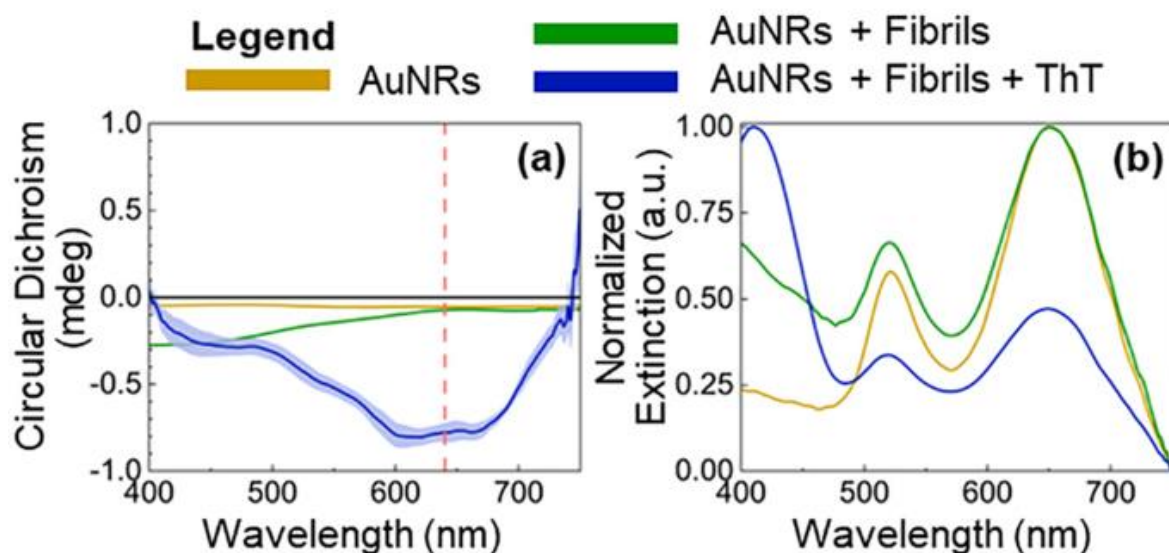


Figure 45. Chiroptical properties of chiral heterostructures made of chiral insulin fibrils and gold nanorods. Circular dichroism (a) and extinction (b) spectra of chiral heterostructures made of gold nanorods and insulin fibrils with pH risen to 6. The standard deviation of the received signal, based on measurements of 10 samples, is marked in light blue. Images are reprinted with permission from reference no.²⁴⁵ Copyright © 2024 American Chemical Society.

Further research on that topic was done by Dr. Saaj Chattopadhyay, who aimed to understand the origin of observed chirality transfer from insulin fibrils to gold nanorods using the single-particle approach.²⁴⁵ The samples prepared in conditions determined during my experiment were imaged with polarization-resolved single-molecule fluorescence and single-particle photoluminescence imaging. However, the sensitivity of the implemented single-particle polarimeter was not enough to detect the chirality of insulin fibrils at the single-particle level. Moreover, the experiments presented that, at the single-particle level, single gold nanorods bound to insulin fibrils did not show any induced chirality. Thus, the chiral signal observed from the ensemble sample during the CD experiments might come from the few bigger aggregates of AuNRs present in the sample, not the Coulombic interactions, contrary to experiments on chiroptical properties of chiral heterostructures made of chiral insulin amyloids and gold nanobipyramids.

IX. 7 Conclusions

To summarize, I presented my results concerning the optical properties of chiral heterostructures made of chiral insulin amyloids mixed with gold nanobipyramids and gold nanorods. First, the presented nanoparticle synthesis resulted in achiral mini gold nanobipyramids with the size of 23 x 11 nm and an LSPR band located at 622 nm. Secondly, the experiments on bovine insulin amyloids confirmed, that factors such as temperature, pH and NaCl concentration can control not only their chiroptical properties, as probed by different intensities of induced circular dichroism of Thioflavin T molecules labelling the amyloids, but also strongly influences their morphology. Moreover, as observed during AFM imaging, sodium chloride strongly influences the aggregation of insulin fibrils, allowing the creation of chiral superstructures. I successfully created chiral heterostructures made of insulin amyloids, as chiral matrix, and achiral gold nanobipyramids. Furthermore, assembling heterostructures induced new chiroptical properties in BPs – a chiral signal, visible in CD spectra, located at the wavelength corresponding to the LSPR of nanoparticles and with sign corresponding to chiroptical properties of the matrix. However, this was only possible under certain conditions – 100 mM concentration of sodium chloride in the reaction solution and the appropriate extinction ratio of nanoparticles to chiral matrix equal to 7.5. Additionally, the shape and location of the induced chiral signal depends on the type of chiral matrix itself – the sample made with amyloids incubated without NaCl induced a low-intensity (-1mdeg) negative band at 585 nm, meanwhile the sample made with amyloids incubated with 100 mM NaCl, stronger (-4 mdeg) negative band at the precise location of BPs LSPR. The induced chiral signal was amyloid-specific since no signal was observed upon mixing the BPs with the pre-incubation solution of insulin proteins. Subsequent research focused on explaining the origin of the observed phenomenon. TEM imaging of studied heterostructures confirmed that BPs were not arranged in a chiral or helical manner and were separated by a distance that prevents effective plasmon coupling between them. Additionally, the statistical analysis of BPs aggregation form proved that, in the case of both samples where the induced chiral signal was observed, the majority of the nanoparticles are in monomeric form, with less than 10% constituting dimers, trimers any bigger aggregates. Because of that, I looked at other effects that could explain the observed effects, such as Coulombic interactions between BPs and chiral protein molecules. Further research on that topic has proven, that created heterostructures meet all the conditions necessary for these interactions to occur: negligible nanoparticle to chiral molecule distance, homogenous size of nanoparticles, overlapping absorption spectra and favoured orientation angles of BPs bound to amyloid fibrils, enabling efficient interaction between BPs and amyloids transition dipole moments. In the end, creating and exploring the optical properties of the chiral heterostructure with a third type of amyloid, incubated with a lower NaCl concentration equal to 25 mM, showed that induced chiral signal could be connected with the internal structure of amyloids, probably sensing the chiral tyrosine residues. Thus, bipyramids can be used as selective biosensors of various forms of insulin amyloids.

I also created chiral heterostructures made of different type of insulin amyloids, characterized by long single fibrils, and gold nanorods with sizes 80 x 40 nm. The measurements of chiroptical properties showed that the conditions determined during the experiments with BPs are not universal and every type of nanoparticle requires other parameters

to induce chiral signal in achiral nanoparticles. In the case of nanorods, NaCl caused strong aggregation of nanoparticles and the final pH of the solution, elevated from 2 to 6, turned out to be crucial. Moreover, the induction of chiral effects in nanoparticles was observed only after staining the heterostructures with an amyloid-specific dye, Thioflavin T. However, no further investigation was performed to understand why the presence of dye is necessary to observe chiral plasmonic effects. Additionally, these samples were also examined by polarization-resolved single-molecule microscopy, which presented that, at the single-particle level, single gold nanorods bound to insulin fibrils did not show any induced chirality.

Conclusions & perspectives

This work presented my research on the optical properties of selected chiral heterostructures with gold nanoparticles. The first part contained the literature review on the topics of chiral nanomaterials, chiral heterostructures, as well as, plasmonic gold nanoparticles and nanoclusters. It is followed by a literature review of the optical properties of selected types of chiral heterostructures, investigated experimentally later in the work. Moreover, the work presented the experimental methods developed to measure the chiroptical properties of studied materials. Thus, obtained results and conclusions could be of interest to anyone working with chiral nanomaterials or chiral molecules.

First of all, my research on Arg/ATT-AuNCs showed that chiral biomolecule-protected gold nanoclusters could emit both one-photon and two-photon excited circularly polarized luminescence. Moreover, 2PCPL was stronger than 1PCPL, as confirmed by their luminescence dissymmetry factors which were of the order of magnitude of 10^{-3} and 10^{-2} for one-photon and two-photon excited CPL, respectively. This observation agreed with the previously published results concerning one-photon and two-photon CD, where the two-photon excited signal was also stronger.¹⁶⁵ **Therefore, this proves that indeed two-photon excited circularly polarized luminescence and circular dichroism of Arg/ATT-AuNCs and ATT-AuNCs are stronger than their one-photon counterparts.** As proposed in this dissertation, it may be caused by the different radiative relaxation pathways of one-photon and two-photon excited luminescence, confirmed by the different photoluminescence lifetimes. What is even more interesting, my experiments have shown a broken symmetry between chiral luminescence and chiral absorption. Both, 1PCPL and 2PCPL spectra proved that both, L-Arg/ATT-AuNCs and D-Arg/ATT-AuNCs emit CPL of one-handedness. This has been explained by the core origin of observed CPL and confirmed by 1PCPL and 2PCPL signals of the same intensity and handedness as enantiomers, observed from unfunctionalized ATT-AuNCs. However, the final explanation of this issue will require a thorough understanding of the structure of Arg/ATT-AuNCs and performing in-depth calculations considering their chiroptical properties, which was out of the scope of this work. Nevertheless, this study has shown that chiral biomolecule-protected nanoclusters possess exceptionally strong non-linear chiroptical properties which, together with their comparatively high two-photon cross-sections^{145, 165} and biocompatibility, make them a promising candidate for next-generation fluorescent markers.

Secondly, the results considering **liquid-crystalline template-directed assemblies of gold nanoclusters proved that the surface-functionalization and co-assembly method used to helically assemble plasmonic gold nanoparticles could be successfully used to helically assemble ultra-small gold nanoclusters.**³⁵ Therefore, it is one of the first reported template-driven assembly methods that could be used with gold nanoparticles of various sizes, also with diameters $< 2\text{nm}$. It required a double-functionalization of $\text{Au}_{25}(\text{PET})_{18}$ surface with two ligands, L and DDT, ensuring correct interaction with OIM matrix molecules. Moreover, as confirmed by absorption spectra and MALDI mass spectrometry, such a way of AuNCs assembly neither impair the nanocluster structure, nor their optical properties. However, the assembly leads to photoluminescence redshift, caused by electronic coupling. Additionally, as

proved by AFM imaging and CPL measurements, the helical AuNC-coated nanofilaments created domains of both handedness, emitting positive and negative CPL. Thus, my work has resolved another of the issues concerning the chiral heterostructures with gold nanoclusters, by broadening the short list of templates that could be used not only to assemble them into hierarchical structures but also to tune their optical properties. Additionally, the **CPL measurements of double-functionalized Au₂₅(PET)₁₈ before and after the helical assembly as well as OIM helical nanofilaments without the nanoclusters confirmed that chiral luminescence originates from the helical assembly of gold nanoclusters.** The CPL signal of OIM nanofilaments was of the same order of magnitude ($g_{lum} \sim 10^{-1}$), but blue-shifted for around 300 nm compared to the signal collected from the helical assemblies of AuNCs. Therefore, in opposition to the results reported by Zhang *et al.*,⁶⁷ my work proved that template-directed helical assembly of gold nanoclusters could induce CPL from the nanoclusters, not enhanced CPL from the matrix due to co-assembly.

During the work on this thesis, I also explored the chiral heterostructures with plasmonic gold nanoparticles – gold nanobipyramids assembled with chiral insulin aggregates. Interestingly, contrary to previous reports on assemblies with amyloids, such heterostructures exhibited induced circular dichroism in the plasmonic range without any helical assembly. **TEM imaging correlated with the CD study showed that observed effects come from the monomers or dimers of gold nanobipyramids interacting with the local chiral field of the matrix due to dipole coupling, not the helical assembly.** Furthermore, the location and intensity of the signal depended on the insulin amyloid structural features, such as the exposed Tyr residues. Thus, proving that gold nanobipyramids could potentially be more specific and easily applicable biosensors than gold nanorods in the detection of amyloid fibrils.⁴⁶ However, both *in vitro* and *in vivo* studies on the interaction of AuBPs with neurodegenerative-disease-connected proteins such as amyloid β are still needed to fully check their biosensing potential. The studies on AuBP-insulin heterostructures also formed the foundation for a project aimed at investigating the interactions between the gold nanoparticles and chiral molecules at the single-molecule level. In collaboration with the team of Professor Julie Biteen, I explored the interaction between single gold nanorods and single insulin fibrils and discovered that in an ensemble solution, it leads to an induced chiral plasmon signal. **Although, as confirmed by polarization-resolved single-molecule microscopy, at the single-particle level, single gold nanorods bound to insulin fibrils did not show any induced chirality.** It is possible, however, that the chiral interactions were too weak to be observed because the system sensitivity was determined to be 5%. Thus, to resolve this issue, further studies using more sensitive measurement systems coupled with theoretical calculations are needed.

Last but not least, it is worth noting that all three experimental parts presented in this dissertation required a novel, interdisciplinary approach and, in some cases, also constructing new measurement setups. Topics covered during the work on my doctoral thesis involved areas such as biology, chemistry, physics, and materials engineering. Moreover, in each presented topic, I was responsible for both sample preparation and its measurements. Furthermore, it required not only substantial knowledge about chiral nanomaterials and their properties, but also the technical skills required to correctly design and build new spectroscopic and

microscopic systems. Understanding the source of the broken symmetry observed for Arg/ATT-AuNCs was possible due to the construction of a two-photon excited fluorescence lifetime measuring system. A system, that also played a vital role in understanding the origin of two-photon excited autofluorescence of lysozyme amyloids.¹⁹² Research on the helical assemblies of gold nanoclusters required developing a methodology for measuring the optical properties of thin layers under non-destructive conditions. Moreover, a new one-photon CPL microscopy setup was built to explore the chiroptical properties gained by gold nanoclusters due to helical assembly. In the end, one of the first reported two-photon excited CPL measuring systems was designed, built and calibrated to explore the 2PCPL of arginine-coated gold nanoclusters.

In conclusion, each of the explored topics broadened the knowledge about the optical properties of the specific type of chiral heterostructures. The research on chiral gold nanoclusters presented in this dissertation is one of the first proofs of the broken symmetry between chiroptical properties of chiral nanomaterials, which gives them a ground-breaking character and may inspire searching for other nanomaterials of this type. After all, isn't the fact that there is more matter than antimatter in the universe, which allowed the creation of life and the world as we know it, a universal example of broken symmetry? Thus, understanding the processes at work behind it is absolutely crucial to unraveling the mysteries of the world around us. Moreover, the record-breaking non-linear and linear chiroptical properties of Arg-ATT/AuNCs and helical assemblies of Au₂₅(PET)₁₈, prove that gold nanoclusters might be counted among the strongest known chiral emitters and encourage other studies of such chiral heterostructures. On the other hand, chiral heterostructures with gold nanobipyramids showed their possible application as biosensors of structural changes in protein aggregates. As we delve deeper into the study and application of chiral heterostructures, it becomes clear that these materials are poised to play a pivotal role in addressing some of the most significant challenges facing modern science and technology. Their unique optical properties not only hold promise for advancing fundamental research in physics and chemistry, but also present tangible solutions to practical problems in areas such as biosensing, bioimaging, and advanced materials. The exploration of these materials offers exciting prospects for the future, with the potential to shape the next generation of technological innovations.

Bibliography

1. Firouzeh, S.; Hossain, M. A.; Cuerva, J. M.; Álvarez de Cienfuegos, L.; Pramanik, S. *Accounts of Chemical Research* **2024**, 57, (10), 1478-1487.
2. Kwon, J.; Choi, W. J.; Jeong, U.; Jung, W.; Hwang, I.; Park, K. H.; Ko, S. G.; Park, S. M.; Kotov, N. A.; Yeom, J. *Nano Convergence* **2022**, 9, (1), 32.
3. Vovk, I. A.; Baimuratov, A. S.; Zhu, W.; Shalkovskiy, A. G.; Baranov, A. V.; Fedorov, A. V.; Rukhlenko, I. D. *Scientific Reports* **2017**, 7, (1), 45925.
4. Li, S.; Xu, X.; Xu, L.; Lin, H.; Kuang, H.; Xu, C. *Nature Communications* **2024**, 15, (1), 3506.
5. Biswas, A.; Cencillo-Abad, P.; Shabbir, M. W.; Karmakar, M.; Chanda, D. *Science Advances* 10, (8), eadk2560.
6. Li, L.; Zhu, F.; Tang, Y.; Zhu, D.; Wang, L.; Wang, J. *Journal of Analysis and Testing* **2024**.
7. Wang, G.; Zhang, H.; Kuang, H.; Xu, C.; Xu, L. *Matter* **2023**, 6, (6), 1752-1781.
8. Ma, W.; Kuang, H.; Wang, L.; Xu, L.; Chang, W.-S.; Zhang, H.; Sun, M.; Zhu, Y.; Zhao, Y.; Liu, L.; Xu, C.; Link, S.; Kotov, N. A. *Scientific Reports* **2013**, 3, (1), 1934.
9. Yan, W.; Xu, L.; Xu, C.; Ma, W.; Kuang, H.; Wang, L.; Kotov, N. A. *Journal of the American Chemical Society* **2012**, 134, (36), 15114-15121.
10. Li, G.; Fei, X.; Liu, H.; Gao, J.; Nie, J.; Wang, Y.; Tian, Z.; He, C.; Wang, J.-L.; Ji, C.; Oron, D.; Yang, G. *ACS Nano* **2020**, 14, (4), 4196-4205.
11. Gong, W.; Chen, Z.; Dong, J.; Liu, Y.; Cui, Y. *Chemical Reviews* **2022**, 122, (9), 9078-9144.
12. Liang, J.; Yang, B.; Deng, J. *Chemical Engineering Journal* **2018**, 344, 262-269.
13. Döring, A.; Ushakova, E.; Rogach, A. L. *Light: Science & Applications* **2022**, 11, (1), 75.
14. He, S.; Jiang, Z.; Dou, X.; Gao, L.; Feng, C. *ChemPlusChem* **2023**, 88, (7), e202300226.
15. Wu, C.; Arju, N.; Kelp, G.; Fan, J. A.; Dominguez, J.; Gonzales, E.; Tutuc, E.; Brener, I.; Shvets, G. *Nature Communications* **2014**, 5, (1), 3892.
16. Zhao, S.; Zhu, H.; Lu, J.; Li, M.; Zhao, L.; Zhou, L.; Gao, L. *Advanced Functional Materials* **2022**, 32, (44), 2201927.
17. Dzwolak, W. *Chirality* **2014**, 26, (9), 580-587.
18. Karst, J.; Cho, N. H.; Kim, H.; Lee, H.-E.; Nam, K. T.; Giessen, H.; Hentschel, M. *ACS Nano* **2019**, 13, (8), 8659-8668.
19. Tohgha, U.; Deol, K. K.; Porter, A. G.; Bartko, S. G.; Choi, J. K.; Leonard, B. M.; Varga, K.; Kubelka, J.; Muller, G.; Balaz, M. *ACS Nano* **2013**, 7, (12), 11094-11102.

20. Deng, H.-H.; Shi, X.-Q.; Wang, F.-F.; Peng, H.-P.; Liu, A.-L.; Xia, X.-H.; Chen, W. *Chemistry of Materials* **2017**, 29, (3), 1362-1369.
21. Cheng, G.; Xu, D.; Lu, Z.; Liu, K. *ACS Nano* **2019**, 13, (2), 1479-1489.
22. Yeom, J.; Yeom, B.; Chan, H.; Smith, K. W.; Dominguez-Medina, S.; Bahng, Joong H.; Zhao, G.; Chang, W.-S.; Chang, S.-J.; Chuvilin, A.; Melnikau, D.; Rogach, A. L.; Zhang, P.; Link, S.; Král, P.; Kotov, N. A. *Nature Materials* **2015**, 14, (1), 66-72.
23. Wang, Z.-Y.; Zhang, N.-N.; Li, J.-C.; Lu, J.; Zhao, L.; Fang, X.-D.; Liu, K. *Soft Matter* **2021**, 17, (26), 6298-6304.
24. Dong, J.; Zhou, Y.; Pan, J.; Zhou, C.; Wang, Q. *Chemical Communications* **2021**, 57, (50), 6201-6204.
25. Grzelak, D.; Tupikowska, M.; Vila-Liarte, D.; Beutel, D.; Bagiński, M.; Parzyszek, S.; Góra, M.; Rockstuhl, C.; Liz-Marzán, L. M.; Lewandowski, W. *Advanced Functional Materials* **2022**, 32, (16), 2111280.
26. Vila-Liarte, D.; Kotov, N. A.; Liz-Marzán, L. M. *Chemical Science* **2022**, 13, (3), 595-610.
27. Li, Y.; Zhang, J.; Chen, Q.; Xia, X.; Chen, M. *Advanced Materials* **2021**, 33, (27), 2100855.
28. Wu, F.; Xia, S.; Wei, J.; Gao, W.; Li, F.; Niu, W. *ChemPhysChem* **2023**, 24, (15), e202200881.
29. Shanks, D. N.; MahdikhanySarvejahany, F.; Muccianti, C.; Alfrey, A.; Koehler, M. R.; Mandrus, D. G.; Taniguchi, T.; Watanabe, K.; Yu, H.; LeRoy, B. J.; Schaibley, J. R. *Nano Letters* **2021**, 21, (13), 5641-5647.
30. Lv, Y.; Duan, S.; Wang, R. *Progress in Natural Science: Materials International* **2020**, 30, (1), 1-12.
31. Liu, J.; Peng, Q. *Acta Biomaterialia* **2017**, 55, 13-27.
32. Li, Q.; Barrett, D. G.; Messersmith, P. B.; Holten-Andersen, N. *ACS Nano* **2016**, 10, (1), 1317-1324.
33. Cha, C.; Shin, S. R.; Gao, X.; Annabi, N.; Dokmeci, M. R.; Tang, X.; Khademhosseini, A. *Small* **2014**, 10, (3), 514-523.
34. Park, W.; Park, S.-j.; Na, K. *Biomaterials* **2011**, 32, (32), 8261-8270.
35. Bagiński, M.; Tupikowska, M.; González-Rubio, G.; Wójcik, M.; Lewandowski, W. *Advanced Materials* **2020**, 32, (1), 1904581.
36. Park, W.; Shin, H.; Choi, B.; Rhim, W.-K.; Na, K.; Keun Han, D. *Progress in Materials Science* **2020**, 114, 100686.
37. Thacker, V. V.; Herrmann, L. O.; Sigle, D. O.; Zhang, T.; Liedl, T.; Baumberg, J. J.; Keyser, U. F. *Nature Communications* **2014**, 5, (1), 3448.
38. Majoinen, J.; Hassinen, J.; Haataja, J. S.; Rekolä, H. T.; Kontturi, E.; Kostianen, M. A.; Ras, R. H. A.; Törmä, P.; Ikkala, O. *Advanced Materials* **2016**, 28, (26), 5262-5267.

39. Urban, M. J.; Shen, C.; Kong, X.-T.; Zhu, C.; Govorov, A. O.; Wang, Q.; Hentschel, M.; Liu, N. *Annual Review of Physical Chemistry* **2019**, 70, (1), 275-299.
40. Lan, X.; Wang, Q. *Advanced Materials* **2016**, 28, (47), 10499-10507.
41. Wang, C.; Tang, C.; Wang, Y.; Shen, Y.; Qi, W.; Zhang, T.; Su, R.; He, Z. *Current Opinion in Solid State and Materials Science* **2022**, 26, (5), 101017.
42. Helgert, C.; Pshenay-Severin, E.; Falkner, M.; Menzel, C.; Rockstuhl, C.; Kley, E.-B.; Tünnermann, A.; Lederer, F.; Pertsch, T. *Nano Letters* **2011**, 11, (10), 4400-4404.
43. Wu, W.; Battie, Y.; Lemaire, V.; Decher, G.; Pauly, M. *Nano Letters* **2021**, 21, (19), 8298-8303.
44. Gao, J.; Wu, W.; Lemaire, V.; Carvalho, A.; Nlate, S.; Buffeteau, T.; Oda, R.; Battie, Y.; Pauly, M.; Pouget, E. *ACS Nano* **2020**, 14, (4), 4111-4121.
45. Kuzyk, A.; Schreiber, R.; Fan, Z.; Pardatscher, G.; Roller, E.-M.; Högele, A.; Simmel, F. C.; Govorov, A. O.; Liedl, T. *Nature* **2012**, 483, (7389), 311-314.
46. Kumar, J.; Eraña, H.; López-Martínez, E.; Claes, N.; Martín, V. F.; Solís, D. M.; Bals, S.; Cortajarena, A. L.; Castilla, J.; Liz-Marzán, L. M. *Proc. Natl. Acad. Sci. U.S.A* **2018**, 115, (13), 3225.
47. Tamoto, R.; Lecomte, S.; Si, S.; Moldovan, S.; Ersen, O.; Delville, M.-H.; Oda, R. *The Journal of Physical Chemistry C* **2012**, 116, (43), 23143-23152.
48. Winogradoff, D.; Li, P.-Y.; Joshi, H.; Quednau, L.; Maffeo, C.; Aksimentiev, A. *Advanced Science* **2021**, 8, (5), 2003113.
49. Liu, H.; Shen, X.; Wang, Z.-G.; Kuzyk, A.; Ding, B. *Nanoscale* **2014**, 6, (16), 9331-9338.
50. Ceconello, A.; Besteiro, L. V.; Govorov, A. O.; Willner, I. *Nature Reviews Materials* **2017**, 2, (9), 17039.
51. Molotsky, T.; Tamarin, T.; Moshe, A. B.; Markovich, G.; Kotlyar, A. B. *The Journal of Physical Chemistry C* **2010**, 114, (38), 15951-15954.
52. Zhang, Q.; Hernandez, T.; Smith Kyle, W.; Hosseini Jebeli Seyyed, A.; Dai Alan, X.; Warning, L.; Baiyasi, R.; McCarthy Lauren, A.; Guo, H.; Chen, D.-H.; Dionne Jennifer, A.; Landes Christy, F.; Link, S. *Science* **2019**, 365, (6460), 1475-1478.
53. Naito, M.; Iwahori, K.; Miura, A.; Yamane, M.; Yamashita, I. *Angewandte Chemie International Edition* **2010**, 49, (39), 7006-7009.
54. Govorov, A. O.; Fan, Z. *ChemPhysChem* **2012**, 13, (10), 2551-2560.
55. Govorov, A. O. *J. Phys. Chem. C* **2011**, 115, (16), 7914-7923.
56. Chibber, S.; Ahmad, I. *Biochemistry and Biophysics Reports* **2016**, 6, 63-67.
57. Ke, P. C.; Zhou, R.; Serpell, L. C.; Riek, R.; Knowles, T. P. J.; Lashuel, H. A.; Gazit, E.; Hamley, I. W.; Davis, T. P.; Fändrich, M.; Otzen, D. E.; Chapman, M. R.;

- Dobson, C. M.; Eisenberg, D. S.; Mezzenga, R. *Chem Soc Rev* **2020**, 49, (15), 5473-5509.
58. Wang, L.; Urbas, A. M.; Li, Q. *Advanced Materials* **2020**, 32, (41), 1801335.
59. Duan, C.; Cheng, Z.; Wang, B.; Zeng, J.; Xu, J.; Li, J.; Gao, W.; Chen, K. *Small* **2021**, 17, (30), 2007306.
60. Querejeta-Fernández, A.; Kopera, B.; Prado, K. S.; Klinkova, A.; Methot, M.; Chauve, G.; Bouchard, J.; Helmy, A. S.; Kumacheva, E. *ACS Nano* **2015**, 9, (10), 10377-10385.
61. Liu, P.; Battie, Y.; Decossas, M.; Tan, S.; Pouget, E.; Okazaki, Y.; Sagawa, T.; Oda, R. *ACS Nano* **2021**, 15, (10), 16411-16421.
62. Liu, P.; Chen, W.; Okazaki, Y.; Battie, Y.; Brocard, L.; Decossas, M.; Pouget, E.; Müller-Buschbaum, P.; Kauffmann, B.; Pathan, S.; Sagawa, T.; Oda, R. *Nano Letters* **2020**, 20, (12), 8453-8460.
63. Cheng, J.; Le Saux, G.; Gao, J.; Buffeteau, T.; Battie, Y.; Barois, P.; Ponsinet, V.; Delville, M.-H.; Ersen, O.; Pouget, E.; Oda, R. *ACS Nano* **2017**, 11, (4), 3806-3818.
64. Thomas, A. R.; Swetha, K.; C. K, A.; Ashraf, R.; Kumar, J.; Kumar, S.; Mandal, S. S. *Journal of Materials Chemistry B* **2022**, 10, (33), 6360-6371.
65. Sang, Y.; Han, J.; Zhao, T.; Duan, P.; Liu, M. *Advanced Materials* **2020**, 32, (41), 1900110.
66. Parzyszek, S.; Tessarolo, J.; Pedraza-Tardajos, A.; Ortuño, A. M.; Bagiński, M.; Bals, S.; Clever, G. H.; Lewandowski, W. *ACS Nano* **2022**, 16, (11), 18472-18482.
67. Zhang, T.; Tang, C.; Wang, Y.; Wang, C.; Zhang, Y.; Qi, W.; Su, R.; He, Z. *Langmuir* **2022**, 38, (13), 4147-4155.
68. Mancinelli, M.; Bencivenni, G.; Pecorari, D.; Mazzanti, A. *European Journal of Organic Chemistry* **2020**, 2020, (27), 4070-4086.
69. Shinmori, H.; Mochizuki, C. *Chem Commun (Camb)* **2017**, 53, (49), 6569-6572.
70. Yan, J.; Feng, W.; Kim, J.-Y.; Lu, J.; Kumar, P.; Mu, Z.; Wu, X.; Mao, X.; Kotov, N. A. *Chemistry of Materials* **2020**, 32, (1), 476-488.
71. Lu, J.; Xue, Y.; Bernardino, K.; Zhang, N.-N.; Gomes Weverson, R.; Ramesar Naomi, S.; Liu, S.; Hu, Z.; Sun, T.; de Moura Andre, F.; Kotov Nicholas, A.; Liu, K. *Science* **2021**, 371, (6536), 1368-1374.
72. Zhao, L.; Zhou, Y.; Niu, G.; Gao, F.; Sun, Z.; Li, H.; Jiang, Y. *Particle & Particle Systems Characterization* **2022**, 39, (4), 2100231.
73. Hou, K.; Zhao, J.; Wang, H.; Li, B.; Li, K.; Shi, X.; Wan, K.; Ai, J.; Lv, J.; Wang, D.; Huang, Q.; Wang, H.; Cao, Q.; Liu, S.; Tang, Z. *Nature Communications* **2020**, 11, (1), 4790.

74. Sun, M.; Xu, L.; Qu, A.; Zhao, P.; Hao, T.; Ma, W.; Hao, C.; Wen, X.; Colombari, F. M.; de Moura, A. F.; Kotov, N. A.; Xu, C.; Kuang, H. *Nature Chemistry* **2018**, 10, (8), 821-830.
75. Gao, F.; Sun, M.; Ma, W.; Wu, X.; Liu, L.; Kuang, H.; Xu, C. *Advanced Materials* **2017**, 29, (18), 1606864.
76. Ma, W.; Kuang, H.; Xu, L.; Ding, L.; Xu, C.; Wang, L.; Kotov, N. A. *Nature Communications* **2013**, 4, (1), 2689.
77. Xu, L.; Xu, Z.; Ma, W.; Liu, L.; Wang, L.; Kuang, H.; Xu, C. *Journal of Materials Chemistry B* **2013**, 1, (35), 4478-4483.
78. Ngamdee, K.; Ngeontae, W. *Sensors and Actuators B: Chemical* **2018**, 274, 402-411.
79. Li, S.; Xu, L.; Ma, W.; Wu, X.; Sun, M.; Kuang, H.; Wang, L.; Kotov, N. A.; Xu, C. *Journal of the American Chemical Society* **2016**, 138, (1), 306-312.
80. Hao, C.; Xu, L.; Ma, W.; Wu, X.; Wang, L.; Kuang, H.; Xu, C. *Advanced Functional Materials* **2015**, 25, (36), 5816-5822.
81. Hao, C.; Gao, R.; Li, Y.; Xu, L.; Sun, M.; Xu, C.; Kuang, H. *Angewandte Chemie International Edition* **2019**, 58, (22), 7371-7374.
82. Xu, L.; Sun, M.; Cheng, P.; Gao, R.; Wang, H.; Ma, W.; Shi, X.; Xu, C.; Kuang, H. *Advanced Functional Materials* **2018**, 28, (18), 1707237.
83. Alex, S.; Tiwari, A. *J Nanosci Nanotechnol* **2015**, 15, (3), 1869-94.
84. Langille, M. R.; Personick, M. L.; Zhang, J.; Mirkin, C. A. *Journal of the American Chemical Society* **2012**, 134, (35), 14542-14554.
85. Ali, M. R.; Snyder, B.; El-Sayed, M. A. *Langmuir* **2012**, 28, (25), 9807-15.
86. Mayer, K. M.; Hafner, J. H. *Chemical Reviews* **2011**, 111, (6), 3828-3857.
87. Kim, S.; Yoon, S. *Bulletin of the Korean Chemical Society* **2021**, 42, (8), 1058-1065.
88. Amendola, V.; Pilot, R.; Frascioni, M.; Maragò, O. M.; Iatì, M. A. *Journal of Physics: Condensed Matter* **2017**, 29, (20), 203002.
89. Liu, J.; He, H.; Xiao, D.; Yin, S.; Ji, W.; Jiang, S.; Luo, D.; Wang, B.; Liu, Y., Recent Advances of Plasmonic Nanoparticles and their Applications. In *Materials*, 2018; Vol. 11.
90. Hutter, E.; Fendler, J. H. *Advanced Materials* **2004**, 16, (19), 1685-1706.
91. Chen, G.; Wang, Y.; Tan, L. H.; Yang, M.; Tan, L. S.; Chen, Y.; Chen, H. *Journal of the American Chemical Society* **2009**, 131, (12), 4218-4219.
92. Slaughter, L. S.; Wu, Y.; Willingham, B. A.; Nordlander, P.; Link, S. *ACS Nano* **2010**, 4, (8), 4657-4666.
93. Sharifi, M.; Attar, F.; Saboury, A. A.; Akhtari, K.; Hooshmand, N.; Hasan, A.; El-Sayed, M. A.; Falahati, M. *Journal of Controlled Release* **2019**, 311-312, 170-189.

94. Hentschel, M.; Schäferling, M.; Duan, X.; Giessen, H.; Liu, N. *Science Advances* **2017**, 3, (5), e1602735.
95. Lee, H.-E.; Ahn, H.-Y.; Mun, J.; Lee, Y. Y.; Kim, M.; Cho, N. H.; Chang, K.; Kim, W. S.; Rho, J.; Nam, K. T. *Nature* **2018**, 556, (7701), 360-365.
96. Zheng, G.; Bao, Z.; Pérez-Juste, J.; Du, R.; Liu, W.; Dai, J.; Zhang, W.; Lee, L. Y. S.; Wong, K.-Y. *Angewandte Chemie International Edition* **2018**, 57, (50), 16452-16457.
97. González-Rubio, G.; Mosquera, J.; Kumar, V.; Pedraza-Tardajos, A.; Llombart, P.; Solís, D. M.; Lobato, I.; Noya, E. G.; Guerrero-Martínez, A.; Taboada, J. M.; Obelleiro, F.; MacDowell, L. G.; Bals, S.; Liz-Marzán, L. M. *Science* **2020**, 368, (6498), 1472-1477.
98. Golze, S. D.; Porcu, S.; Zhu, C.; Sutter, E.; Ricci, P. C.; Kinzel, E. C.; Hughes, R. A.; Neretina, S. *Nano Letters* **2021**, 21, (7), 2919-2925.
99. Zhang, N.-N.; Sun, H.-R.; Liu, S.; Xing, Y.-C.; Lu, J.; Peng, F.; Han, C.-L.; Wei, Z.; Sun, T.; Yang, B.; Liu, K. *CCS Chemistry* **2021**, 4, (2), 660-670.
100. Fan, Z.; Govorov, A. O. *Nano Letters* **2012**, 12, (6), 3283-3289.
101. Govorov, A. O.; Fan, Z.; Hernandez, P.; Slocik, J. M.; Naik, R. R. *Nano Letters* **2010**, 10, (4), 1374-1382.
102. Slocik, J. M.; Govorov, A. O.; Naik, R. R. *Nano Letters* **2011**, 11, (2), 701-705.
103. Nesterov, M. L.; Yin, X.; Schäferling, M.; Giessen, H.; Weiss, T. *ACS Photonics* **2016**, 3, (4), 578-583.
104. Wang, R.-Y.; Wang, P.; Liu, Y.; Zhao, W.; Zhai, D.; Hong, X.; Ji, Y.; Wu, X.; Wang, F.; Zhang, D.; Zhang, W.; Liu, R.; Zhang, X. *The Journal of Physical Chemistry C* **2014**, 118, (18), 9690-9695.
105. Severoni, E.; Maniappan, S.; Liz-Marzán, L. M.; Kumar, J.; García de Abajo, F. J.; Galantini, L. *ACS Nano* **2020**, 14, (12), 16712-16722.
106. Hou, S.; Wen, T.; Zhang, H.; Liu, W.; Hu, X.; Wang, R.; Hu, Z.; Wu, X. *Nano Research* **2014**, 7, (11), 1699-1705.
107. Naka, K.; Itoh, H.; Chujo, Y. *Langmuir* **2003**, 19, (13), 5496-5501.
108. Ni, W.; Mosquera, R. A.; Pérez-Juste, J.; Liz-Marzán, L. M. *The Journal of Physical Chemistry Letters* **2010**, 1, (8), 1181-1185.
109. Chen, C.-L.; Rosi, N. L. *Journal of the American Chemical Society* **2010**, 132, (20), 6902-6903.
110. El-Sayed, I. H.; Huang, X.; El-Sayed, M. A. *Nano Letters* **2005**, 5, (5), 829-834.
111. Singh, S. K.; Mazumder, S.; Vincy, A.; Hiremath, N.; Kumar, R.; Banerjee, I.; Vankayala, R. *ACS Applied Nano Materials* **2023**, 6, (3), 1508-1521.
112. Vankayala, R.; Huang, Y.-K.; Kalluru, P.; Chiang, C.-S.; Hwang, K. C. *Small* **2014**, 10, (8), 1612-1622.

113. Erdem, Ö.; Saylan, Y.; Cihangir, N.; Denizli, A. *Biosensors and Bioelectronics* **2019**, 126, 608-614.
114. Kim, W.; Lee, S. H.; Ahn, Y. J.; Lee, S. H.; Ryu, J.; Choi, S. K.; Choi, S. *Biosensors and Bioelectronics* **2018**, 111, 59-65.
115. Campu, A.; Lerouge, F.; Maniu, D.; Magyari, K.; Focsan, M. *J Mol Struct* **2021**, 1246, 131160.
116. Mukherjee, S.; Libisch, F.; Large, N.; Neumann, O.; Brown, L. V.; Cheng, J.; Lassiter, J. B.; Carter, E. A.; Nordlander, P.; Halas, N. J. *Nano Letters* **2013**, 13, (1), 240-247.
117. Chen, X.-J.; Cabello, G.; Wu, D.-Y.; Tian, Z.-Q. *Journal of Photochemistry and Photobiology C: Photochemistry Reviews* **2014**, 21, 54-80.
118. Wu, K.; Chen, J.; McBride, J. R.; Lian, T. *Science* **2015**, 349, (6248), 632-635.
119. Mupparapu, R.; Cunha, J.; Tantussi, F.; Jacassi, A.; Summerer, L.; Patrini, M.; Giugni, A.; Maserati, L.; Alabastri, A.; Garoli, D.; Proietti Zaccaria, R. *Advanced Energy Materials* **2022**, 12, (15), 2103785.
120. Zhou, N.; Yang, Y.; Guo, X.; Gong, J.; Shi, Z.; Yang, Z.; Wu, H.; Gao, Y.; Yao, N.; Fang, W.; Wang, P.; Tong, L. *Science Advances* 8, (27), eabn2026.
121. Jin, R. *Nanoscale* **2010**, 2, (3), 343-362.
122. Zhu, M.; Aikens, C. M.; Hollander, F. J.; Schatz, G. C.; Jin, R. *Journal of the American Chemical Society* **2008**, 130, (18), 5883-5885.
123. Yang, Y.; Han, A.; Li, R.; Fang, G.; Liu, J.; Wang, S. *Analyst* **2017**, 142, (23), 4486-4493.
124. Shang, L.; Dong, S.; Nienhaus, G. U. *Nano Today* **2011**, 6, (4), 401-418.
125. Zhu, S.; Wang, X.; Cong, Y.; Li, L. *ACS Omega* **2020**, 5, (36), 22702-22707.
126. Jin, R.; Zeng, C.; Zhou, M.; Chen, Y. *Chemical Reviews* **2016**, 116, (18), 10346-10413.
127. Nasaruddin, R. R.; Chen, T.; Yan, N.; Xie, J. *Coordination Chemistry Reviews* **2018**, 368, 60-79.
128. Jin, R.; Qian, H.; Wu, Z.; Zhu, Y.; Zhu, M.; Mohanty, A.; Garg, N. *The Journal of Physical Chemistry Letters* **2010**, 1, (19), 2903-2910.
129. Zeng, C.; Chen, Y.; Das, A.; Jin, R. *The Journal of Physical Chemistry Letters* **2015**, 6, (15), 2976-2986.
130. Jadzinsky, P. D.; Calero, G.; Ackerson, C. J.; Bushnell, D. A.; Kornberg, R. D. *Science* **2007**, 318, (5849), 430-433.
131. Heaven, M. W.; Dass, A.; White, P. S.; Holt, K. M.; Murray, R. W. *Journal of the American Chemical Society* **2008**, 130, (12), 3754-3755.
132. Jin, R. *Nanoscale* **2015**, 7, (5), 1549-1565.
133. Yuan, X.; Goswami, N.; Chen, W.; Yao, Q.; Xie, J. *Chemical Communications* **2016**, 52, (30), 5234-5237.

134. Zhou, M.; Higaki, T.; Li, Y.; Zeng, C.; Li, Q.; Sfeir, M. Y.; Jin, R. *Journal of the American Chemical Society* **2019**, 141, (50), 19754-19764.
135. Kang, X.; Zhu, M. *Chemical Society Reviews* **2019**, 48, (8), 2422-2457.
136. Wang, G.; Huang, T.; Murray, R. W.; Menard, L.; Nuzzo, R. G. *Journal of the American Chemical Society* **2005**, 127, (3), 812-813.
137. Song, X.-R.; Goswami, N.; Yang, H.-H.; Xie, J. *Analyst* **2016**, 141, (11), 3126-3140.
138. Goswami, N.; Zheng, K.; Xie, J. *Nanoscale* **2014**, 6, (22), 13328-13347.
139. Wu, Z.; Jin, R. *Nano Letters* **2010**, 10, (7), 2568-2573.
140. Mathew, A.; Varghese, E.; Choudhury, S.; Pal, S. K.; Pradeep, T. *Nanoscale* **2015**, 7, (34), 14305-14315.
141. Goswami, N.; Yao, Q.; Luo, Z.; Li, J.; Chen, T.; Xie, J. *The Journal of Physical Chemistry Letters* **2016**, 7, (6), 962-975.
142. Luo, Z.; Yuan, X.; Yu, Y.; Zhang, Q.; Leong, D. T.; Lee, J. Y.; Xie, J. *Journal of the American Chemical Society* **2012**, 134, (40), 16662-16670.
143. Wu, Z.; Du, Y.; Liu, J.; Yao, Q.; Chen, T.; Cao, Y.; Zhang, H.; Xie, J. *Angewandte Chemie International Edition* **2019**, 58, (24), 8139-8144.
144. Huang, H.-Y.; Ca, K.-B.; Io, C.-C.; Chen, P.-W.; Soebroto, R. J.; Shen, J.-L.; Yeh, J.-M.; Yuan, C.-T. *The Journal of Physical Chemistry Letters* **2020**, 11, (21), 9344-9350.
145. Olesiak-Banska, J.; Waszkielewicz, M.; Obstarczyk, P.; Samoc, M. *Chem Soc Rev* **2019**, 48, (15), 4087-4117.
146. Knoppe, S.; Vanbel, M.; van Cleuvenbergen, S.; Vanpraet, L.; Bürgi, T.; Verbiest, T. *The Journal of Physical Chemistry C* **2015**, 119, (11), 6221-6226.
147. Ramakrishna, G.; Varnavski, O.; Kim, J.; Lee, D.; Goodson, T. *Journal of the American Chemical Society* **2008**, 130, (15), 5032-5033.
148. Obstarczyk, P.; Osmólska, J.; Swierczewski, M.; Bürgi, T.; Samoc, M.; Olesiak-Bańska, J. *Journal of Materials Chemistry C* **2024**.
149. Oh, E.; Fatemi, F. K.; Currie, M.; Delehanty, J. B.; Pons, T.; Fragola, A.; Lévéque-Fort, S.; Goswami, R.; Susumu, K.; Huston, A. L.; Medintz, I. L. *Particle & Particle Systems Characterization* **2013**, 30, (5), 453-466.
150. Zeng, C.; Liu, C.; Chen, Y.; Rosi, N. L.; Jin, R. *Journal of the American Chemical Society* **2014**, 136, (34), 11922-11925.
151. Yan, N.; Xia, N.; Liao, L.; Zhu, M.; Jin, F.; Jin, R.; Wu, Z. *Science Advances* **2018**, 4, (10), eaat7259.
152. Zeng, C.; Chen, Y.; Kirschbaum, K.; Lambright, K. J.; Jin, R. *Science* **2016**, 354, (6319), 1580-1584.
153. Ma, Y.; Fu, H.; Zhang, C.; Cheng, S.; Gao, J.; Wang, Z.; Jin, W.; Conde, J.; Cui, D. *Scientific Reports* **2016**, 6, (1), 33436.
154. Kumar, S.; Jin, R. *Nanoscale* **2012**, 4, (14), 4222-4227.

155. Takano, S.; Tsukuda, T. *The Journal of Physical Chemistry Letters* **2016**, *7*, (22), 4509-4513.
156. Si, W.-D.; Sheng, K.; Zhang, C.; Wang, Z.; Zhang, S.-S.; Dou, J.-M.; Feng, L.; Gao, Z.-Y.; Tung, C.-H.; Sun, D. *Chemical Science* **2022**, *13*, (35), 10523-10531.
157. Qu, D.; Zhang, J.; Chu, G.; Jiang, H.; Wu, C.; Xu, Y. *Journal of Materials Chemistry C* **2016**, *4*, (9), 1764-1768.
158. Grzelczak, M.; Vermant, J.; Furst, E. M.; Liz-Marzán, L. M. *ACS Nano* **2010**, *4*, (7), 3591-3605.
159. Truttmann, V.; Loxha, A.; Banu, R.; Pittenauer, E.; Malola, S.; Matus, M. F.; Wang, Y.; Ploetz, E. A.; Rupprechter, G.; Bürgi, T.; Häkkinen, H.; Aikens, C.; Barrabés, N. *ACS Nano* **2023**, *17*, (20), 20376-20386.
160. Zeng, C.; Jin, R. *Chemistry – An Asian Journal* **2017**, *12*, (15), 1839-1850.
161. Yao, H. *Progress in Natural Science: Materials International* **2016**, *26*, (5), 428-439.
162. Jia, T.-T.; Li, B.-J.; Yang, G.; Hua, Y.; Liu, J.-Q.; Ma, W.; Zang, S.-Q.; Chen, X.; Zhao, X. *Nano Today* **2021**, *39*, 101222.
163. Shi, L.; Zhu, L.; Guo, J.; Zhang, L.; Shi, Y.; Zhang, Y.; Hou, K.; Zheng, Y.; Zhu, Y.; Lv, J.; Liu, S.; Tang, Z. *Angewandte Chemie International Edition* **2017**, *56*, (48), 15397-15401.
164. Olesiak-Banska, J.; Waszkielewicz, M.; Samoc, M. *Physical Chemistry Chemical Physics* **2018**, *20*, (38), 24523-24526.
165. Pniakowska, A.; Samoc, M.; Olesiak-Banska, J. *Nanoscale* **2023**, *15*, (19), 8597-8602.
166. Obstarczyk, P.; Kazan, R.; Bürgi, T.; Samoć, M.; Olesiak-Bańska, J. *Journal of the American Chemical Society* **2024**, *146*, (51), 35011-35015.
167. Casteleiro, B.; Da Cruz-Boisson, F.; Alcouffe, P.; Pinto, S. N.; Gaspar Martinho, J. M.; Charreyre, M.-T.; Farinha, J. P. S.; Favier, A. *ACS Applied Nano Materials* **2023**, *6*, (13), 11689-11698.
168. Jiang, X.; Wang, X.; Yao, C.; Zhu, S.; Liu, L.; Liu, R.; Li, L. *The Journal of Physical Chemistry Letters* **2019**, *10*, (17), 5237-5243.
169. Obstarczyk, P.; Pniakowska, A.; Nonappa; Grzelczak, M. P.; Olesiak-Bańska, J. *ACS Omega* **2023**, *8*, (12), 11503-11511.
170. Xia, J.; Wang, X.; Zhu, S.; Liu, L.; Li, L. *ACS applied materials & interfaces* **2019**, *11*, (7), 7369-7378.
171. Zhu, S.; Wang, X.; Li, S.; Liu, L.; Li, L. *ACS applied materials & interfaces* **2020**, *12*, (9), 11063-11071.
172. Zhang, H.; Liu, H.; Tian, Z.; Lu, D.; Yu, Y.; Cestellos-Blanco, S.; Sakimoto, K. K.; Yang, P. *Nature Nanotechnology* **2018**, *13*, (10), 900-905.
173. Liu, Y.; Liu, X.; Yang, S.; Li, F.; Shen, C.; Huang, M.; Li, J.; Nasaruddin, R. R.; Xie, J. *ACS Sustainable Chemistry & Engineering* **2018**, *6*, (11), 15425-15433.

174. Longhena, F.; Boujebene, R.; Brembati, V.; Sandre, M.; Bubacco, L.; Abbate, S.; Longhi, G.; Bellucci, A. *Nanoscale* **2024**, 16, (40), 18882-18898.
175. Goodman, R. P.; Schaap, I. A. T.; Tardin, C. F.; Erben, C. M.; Berry, R. M.; Schmidt, C. F.; Turberfield, A. J. *Science* **2005**, 310, (5754), 1661-1665.
176. Mastroianni, A. J.; Claridge, S. A.; Alivisatos, A. P. *Journal of the American Chemical Society* **2009**, 131, (24), 8455-8459.
177. Tian, Y.; Wang, T.; Liu, W.; Xin, H. L.; Li, H.; Ke, Y.; Shih, W. M.; Gang, O. *Nature Nanotechnology* **2015**, 10, (7), 637-644.
178. Szustakiewicz, P.; Kowalska, N.; Grzelak, D.; Narushima, T.; Góra, M.; Bagiński, M.; Pocięcha, D.; Okamoto, H.; Liz-Marzán, L. M.; Lewandowski, W. *ACS Nano* **2020**, 14, (10), 12918-12928.
179. Guo, Y.; Zhao, X.; Long, T.; Lin, M.; Liu, Z.; Huang, C. *RSC Advances* **2015**, 5, (75), 61449-61454.
180. Hao, F.; Geng, F.; Zhao, X.; Liu, R.; Liu, Q. S.; Zhou, Q.; Jiang, G. *NanoImpact* **2021**, 22, 100321.
181. Brust, M.; Fink, J.; Bethell, D.; Schiffrin, D. J.; Kiely, C. *Journal of the Chemical Society, Chemical Communications* **1995**, (16), 1655-1656.
182. Wu, Z.; Gayathri, C.; Gil, R. R.; Jin, R. *Journal of the American Chemical Society* **2009**, 131, (18), 6535-6542.
183. Monti, M.; Matus, M. F.; Malola, S.; Fortunelli, A.; Aschi, M.; Stener, M.; Häkkinen, H. *ACS Nano* **2023**, 17, (12), 11481-11491.
184. Kluz, M.; Nieznańska, H.; Dec, R.; Dziegielewska, I.; Niżyński, B.; Ścibisz, G.; Puławski, W.; Staszczak, G.; Klein, E.; Smalc-Koziorowska, J.; Dzwolak, W. *PLoS one* **2019**, 14, (6), e0218975.
185. Schaaff, T. G.; Whetten, R. L. *The Journal of Physical Chemistry B* **2000**, 104, (12), 2630-2641.
186. Knoppe, S.; Bürgi, T. *Accounts of Chemical Research* **2014**, 47, (4), 1318-1326.
187. MacKenzie, L. E.; Pålsson, L. O.; Parker, D.; Beeby, A.; Pal, R. *Nat Commun* **2020**, 11, (1), 1676.
188. Sánchez-Carnerero, E. M.; Agarrabeitia, A. R.; Moreno, F.; Maroto, B. L.; Muller, G.; Ortiz, M. J.; de la Moya, S. *Chemistry – A European Journal* **2015**, 21, (39), 13488-13500.
189. Stachelek, P.; MacKenzie, L.; Parker, D.; Pal, R. *Nature Communications* **2022**, 13, (1), 553.
190. Hammer, M.; Schweitzer, D.; Richter, S.; Königsdörffer, E. *Physiological Measurement* **2005**, 26, (4), N9.
191. Arsenovic, P. T.; Mayer, C. R.; Conway, D. E. *Sci Rep* **2017**, 7, (1), 15609.
192. Grelich-Mucha, M.; Lipok, M.; Różycka, M.; Samoć, M.; Olesiak-Bańska, J. *The Journal of Physical Chemistry Letters* **2022**, 13, (21), 4673-4681.

193. Zhong, Y.; Zhang, J.; Li, T.; Xu, W.; Yao, Q.; Lu, M.; Bai, X.; Wu, Z.; Xie, J.; Zhang, Y. *Nature Communications* **2023**, 14, (1), 658.
194. Li, Q.; Zhou, M.; So, W. Y.; Huang, J.; Li, M.; Kauffman, D. R.; Cotlet, M.; Higaki, T.; Peteanu, L. A.; Shao, Z.; Jin, R. *Journal of the American Chemical Society* **2019**, 141, (13), 5314-5325.
195. Liu, Z.; Luo, L.; Jin, R. *Advanced Materials* **2024**, 36, (8), 2309073.
196. Wei, Z.; Pan, Y.; Hou, G.; Ran, X.; Chi, Z.; He, Y.; Kuang, Y.; Wang, X.; Liu, R.; Guo, L. *ACS applied materials & interfaces* **2022**, 14, (2), 2452-2463.
197. Willis, O. G.; Petri, F.; De Rosa, D. F.; Mandoli, A.; Pal, R.; Zinna, F.; Di Bari, L. *Journal of the American Chemical Society* **2023**, 145, (46), 25170-25176.
198. Lee, J.-J.; Kim, B.-C.; Choi, H.-J.; Bae, S.; Araoka, F.; Choi, S.-W. *ACS Nano* **2020**, 14, (5), 5243-5250.
199. Parker, J. F.; Weaver, J. E. F.; McCallum, F.; Fields-Zinna, C. A.; Murray, R. W. *Langmuir* **2010**, 26, (16), 13650-13654.
200. Yang, C.; An, G.; Zhao, X. *Journal of Materials Science: Materials in Electronics* **2013**, 24, (9), 3490-3495.
201. Tofanelli, M. A.; Salorinne, K.; Ni, T. W.; Malola, S.; Newell, B.; Phillips, B.; Häkkinen, H.; Ackerson, C. J. *Chemical Science* **2016**, 7, (3), 1882-1890.
202. Abroshan, H.; Li, G.; Lin, J.; Kim, H. J.; Jin, R. *Journal of Catalysis* **2016**, 337, 72-79.
203. Li, T.; Senesi, A. J.; Lee, B. *Chemical Reviews* **2016**, 116, (18), 11128-11180.
204. Salorinne, K.; Lahtinen, T.; Koivisto, J.; Kalenius, E.; Nissinen, M.; Pettersson, M.; Häkkinen, H. *Analytical Chemistry* **2013**, 85, (7), 3489-3492.
205. Collins, C. B.; Tofanelli, M. A.; Crook, M. F.; Phillips, B. D.; Ackerson, C. J. *RSC Advances* **2017**, 7, (71), 45061-45065.
206. Lewandowski, W.; Fruhnert, M.; Mieczkowski, J.; Rockstuhl, C.; Górecka, E. *Nature Communications* **2015**, 6, (1), 6590.
207. Hough, L. E.; Jung, H. T.; Krüerke, D.; Heberling, M. S.; Nakata, M.; Jones, C. D.; Chen, D.; Link, D. R.; Zasadzinski, J.; Heppke, G.; Rabe, J. P.; Stocker, W.; Körblova, E.; Walba, D. M.; Glaser, M. A.; Clark, N. A. *Science* **2009**, 325, (5939), 456-460.
208. Park, W.; Yoon, D. K. *Crystals* **2020**, 10, (8), 675.
209. Smaisim, G. F.; Mohammed, K. J.; Hadrawi, S. K.; Koteh, H.; Kianfar, E. *BioNanoScience* **2023**, 13, (2), 819-839.
210. Lipok, M.; Obstarczyk, P.; Parzyszek, S.; Wang, Y.; Bagiński, M.; Büergi, T.; Lewandowski, W.; Olesiak-Bañska, J. *Advanced Optical Materials* **2023**, 11, (3), 2201984.
211. Gan, Z.; Lin, Y.; Luo, L.; Han, G.; Liu, W.; Liu, Z.; Yao, C.; Weng, L.; Liao, L.; Chen, J.; Liu, X.; Luo, Y.; Wang, C.; Wei, S.; Wu, Z. *Angewandte Chemie International Edition* **2016**, 55, (38), 11567-11571.

212. Qian, H.; Zhu, M.; Gayathri, C.; Gil, R. R.; Jin, R. *ACS Nano* **2011**, 5, (11), 8935-8942.
213. Valenta, J.; Greben, M.; Pramanik, G.; Kvakova, K.; Cigler, P. *Physical Chemistry Chemical Physics* **2021**, 23, (20), 11954-11960.
214. Derkachova, A.; Kolwas, K.; Demchenko, I. *Plasmonics* **2016**, 11, (3), 941-951.
215. Kumaranchira Ramankutty, K. *Nanoscale* **2024**, 16, (25), 11914-11927.
216. Huang, X.; Neretina, S.; El-Sayed, M. A. *Advanced Materials* **2009**, 21, (48), 4880-4910.
217. Warning, L. A.; Miandashti, A. R.; Misiura, A.; Landes, C. F.; Link, S. *J Phys Chem C* **2022**, 126, (5), 2656-2668.
218. Tullius, R.; Karimullah, A. S.; Rodier, M.; Fitzpatrick, B.; Gadegaard, N.; Barron, L. D.; Rotello, V. M.; Cooke, G.; Lapthorn, A.; Kadodwala, M. *J Am Chem Soc* **2015**, 137, (26), 8380-8383.
219. Lee, S. Y.; Han, Y.; Hong, J. W.; Ha, J. W. *Nanoscale* **2017**, 9, (33), 12060-12067.
220. Rao, W.; Li, Q.; Wang, Y.; Li, T.; Wu, L. *ACS Nano* **2015**, 9, (3), 2783-91.
221. Deska, R.; Obstarczyk, P.; Matczyszyn, K.; Olesiak-Bańska, J. *The Journal of Physical Chemistry Letters* **2021**, 12, (21), 5208-5213.
222. Sánchez-Iglesias, A.; Winckelmans, N.; Altantzis, T.; Bals, S.; Grzelczak, M.; Liz-Marzán, L. M. *J. Am. Chem. Soc.* **2017**, 139, (1), 107-110.
223. Chiti, F.; Dobson, C. M. *Annual Review of Biochemistry* **2017**, 86, (Volume 86, 2017), 27-68.
224. Chiti, F.; Webster, P.; Taddei, N.; Clark, A.; Stefani, M.; Ramponi, G.; Dobson, C. M. *Proceedings of the National Academy of Sciences* **1999**, 96, (7), 3590-3594.
225. Surmacz-Chwedoruk, W.; Babenko, V.; Dec, R.; Szymczak, P.; Dzwolak, W. *Sci Rep* **2016**, 6, (1), 32022.
226. Babenko, V.; Harada, T.; Yagi, H.; Goto, Y.; Kuroda, R.; Dzwolak, W. *Chirality* **2011**, 23, (8), 638-46.
227. Lokszejn, A.; Dzwolak, W. *J Mol Biol* **2008**, 379, (1), 9-16.
228. Kurouski, D.; Dukor, Rina K.; Lu, X.; Nafie, Laurence A.; Lednev, Igor K. *Biophysical Journal* **2012**, 103, (3), 522-531.
229. Muzaffar, M.; Ahmad, A. *PloS one* **2011**, 6, (11), e27906.
230. Ishigaki, M.; Morimoto, K.; Chatani, E.; Ozaki, Y. *Biophys J* **2020**, 118, (12), 2997-3007.
231. Khurana, R.; Coleman, C.; Ionescu-Zanetti, C.; Carter, S. A.; Krishna, V.; Grover, R. K.; Roy, R.; Singh, S. *Journal of structural biology* **2005**, 151, (3), 229-38.
232. Dzwolak, W.; Pecul, M. *FEBS Letters* **2005**, 579, (29), 6601-6603.

233. Kurouski, D.; Lombardi, R. A.; Dukor, R. K.; Lednev, I. K.; Nafie, L. A. *Chemical Communications* **2010**, 46, (38), 7154-7156.
234. Babenko, V.; Surmacz-Chwedoruk, W.; Dzwolak, W. *Langmuir* **2015**, 31, (7), 2180-2186.
235. Rybicka, A.; Longhi, G.; Castiglioni, E.; Abbate, S.; Dzwolak, W.; Babenko, V.; Pecul, M. *ChemPhysChem* **2016**, 17, (18), 2931-2937.
236. Li, R.; Wang, Z.; Gu, X.; Chen, C.; Zhang, Y.; Hu, D. *ACS Omega* **2020**, 5, (10), 4943-4952.
237. Psonka-Antonczyk, K. M.; Duboisset, J.; Stokke, B. T.; Zako, T.; Kobayashi, T.; Maeda, M.; Nyström, S.; Mason, J.; Hammarström, P.; Nilsson, K. P. R.; Lindgren, M., Nanoscopic and Photonic Ultrastructural Characterization of Two Distinct Insulin Amyloid States. In *International Journal of Molecular Sciences*, 2012; Vol. 13, pp 1461-1480.
238. Tseng, K.-H.; Hsieh, C.-L.; Huang, J.-C.; Tien, D.-C. *Journal of Nanomaterials* **2015**, 2015, (1), 612324.
239. Murray, W. A.; Auguié, B.; Barnes, W. L. *J. Phys. Chem. C* **2009**, 113, (13), 5120-5125.
240. Lipok, M.; Obstarczyk, P.; Żak, A.; Olesiak-Bańska, J. *The Journal of Physical Chemistry Letters* **2023**, 14, (49), 11084-11091.
241. Jain, P. K.; Huang, W.; El-Sayed, M. A. *Nano Letters* **2007**, 7, (7), 2080-2088.
242. Warning, L. A.; Miandashti, A. R.; McCarthy, L. A.; Zhang, Q.; Landes, C. F.; Link, S. *ACS Nano* **2021**, 15, (10), 15538-15566.
243. Bouchard, M.; Zurdo, J.; Nettleton, E. J.; Dobson, C. M.; Robinson, C. V. *Protein Sci* **2000**, 9, (10), 1960-7.
244. Kelly, S. M.; Jess, T. J.; Price, N. C. *Biochim Biophys Acta* **2005**, 1751, (2), 119-39.
245. Chattopadhyay, S.; Lipok, M.; Pfaffenberger, Z. J.; Olesiak-Bańska, J.; Biteen, J. S. *The Journal of Physical Chemistry Letters* **2024**, 15, (6), 1618-1622.

Appendix

List of author's papers included in this dissertation:

1. **Lipok, M.**; Obstarczyk, P.; Parzyszek, S.; Wang, Y.; Bagiński, M.; Buerger, T.; Lewandowski, W.; Olesiak-Bañska, J., *Circularly Polarized Luminescence from Atomically Precise Gold Nanoclusters Helically Assembled by Liquid-Crystal Template*, *Advanced Optical Materials*, **2023**, 11, (3), 2201984.
2. **Lipok, M.**; Obstarczyk, P.; Żak, A.; Olesiak-Bañska, J., *Single Gold Nanobipyramids Sensing the Chirality of Amyloids*. *The Journal of Physical Chemistry Letters* **2023**, 14, (49), 11084-11091.
3. Chattopadhyay, S.; **Lipok, M.**; Pfaffenberger, Z. J.; Olesiak-Bañska, J.; Biteen, J. S., *Single-Particle Photoluminescence Measures a Heterogeneous Distribution of Differential Circular Absorbance of Gold Nanoparticle Aggregates near Constricted Thioflavin T Molecules*. *The Journal of Physical Chemistry Letters*, **2024**, 15, (6), 1618-1622.

List of author's papers not included in this dissertation:

1. Obstarczyk, P.; **Lipok, M.**; Grelich-Mucha, M.; Samoć, M.; Olesiak-Bañska, J., *Two-Photon Excited Polarization-Dependent Autofluorescence of Amyloids as a Label-Free Method of Fibril Organization Imaging*. *The Journal of Physical Chemistry Letters* 2021, 12 (5), 1432-1437.
2. Obstarczyk, P.; **Lipok, M.**; Żak, A.; Cwynar, P.; Olesiak-Bañska, J., *Amyloid fibrils in superstructures – local ordering revealed by polarization analysis of two-photon excited autofluorescence*. *Biomaterials Science* 2022, 10 (6), 1554-1561.
3. **M. Lipok**, P. Obstarczyk, J. Olesiak-Bañska, *Polarization-Sensitive Two-Photon Microscopy for a Label-Free Amyloid Structural Characterization*. *J. Vis. Exp.* (199), e65670 (2023)
4. M. Grelich-Mucha, **M. Lipok**, M. Różycka, M. Samoć, J. Olesiak-Bañska, *One- and Two-Photon Excited Autofluorescence of Lysozyme Amyloids*, *J. Phys. Chem. Lett.* 13, 4673–4681 (2022)